UNIVERSITY OF SÃO PAULO
OCEANOGRAPHIC INSTITUTE

JULIA MARTINS DE ARAUJO

On the South Equatorial Undercurrent Origin and Variability in the Western Tropical Atlantic

São Paulo - SP

2022

JULIA MARTINS DE ARAUJO

On the South Equatorial Undercurrent Origin and Variability in the Western Tropical Atlantic

Dissertation presented to Oceanographic Institute (IO) from the University of São Paulo (USP), as part of the requirements to hold the Master of Science degree.

Field of Study: Physical Oceanography.

Advisor: Prof. Dr. Ilson C. A. da Silveira

São Paulo - SP

2022

ARAUJO, Julia. **On the South Equatorial Undercurrent origin and variability in the tropical Atlantic**. Dissertation (Master) presented to Oceanographic Institute from the University of São Paulo as part of the requirements to hold the Master of Science degree, Oceanography Program, Physical Oceanography field of study.

Approved on the ___ / ___ / _____ .

Original version

Prof. Dr. Ilson C. A. da Silveira University of São Paulo (Advisor)	Concept
Professor Institution	Concept
Professor Institution	Concept

São Paulo - SP
2022

Acknowledgements

First of all, I would like to dedicate this work to the person I found along this journey and became one of the most important of my life, my fiance. Pedro made the pandemic a lot easier and funnier even though there were days when nothing made sense. He stood by my side at every single moment of this process and supported me as my best friend and true love. I am also very thankful for my two little cutties, my cat Magê and my dog Malu, for having this amazing power of making me realise I had this small family I could call "my little home".

I would like to thank my family for believing and supporting me throughout this adventure. My mother Clarissa, my father Moacyr and my brother Pedro were always making sure I was strong and capable of completing this challenge and also pushing me to do my best at everything. They are my rock.

Ilson, or better saying "tio Ilson", was the person that made all of this possible. As one of the scientists I most admire in my life, he was able to always make me laugh and carried this journey with his amazing energy. Finally, I also really appreciate the support of everyone at our lab team and I thank for the countless lessons I've learned with this wonderful and outstanding group at the Laboratório de Dinâmica Oceânica (LaDO).

This study was partially funded by the Conselho Nacional de Desenvolvimento Científico e Tecnológico - Brasil (CNPq), through a MSc. scholarship.

"Feliz de quem entende que é preciso mudar muito pra ser sempre o mesmo."

Dom Hélder Câmara

Contents

List of figures

List of tables

List of abbreviations and acronyms

AMEDA	Angular Momentum Eddy Detection and tracking Algorithm
AMOC	Atlantic Meridional Overturning Circulation
ABRACOS	Acoustics along the Brazilian Coast
CASCADE	Chaîne Automatisée de Suivi des Courantomètres Acoustiques Doppler Embarqués
CMEMS	Copernicus Marine Environment Monitoring System
CODAS	Common Ocean Data Access System
CTD	Conductivity Temperature Depth
CTW	Coastal Trapped Wave
EAW	Eastern Atlantic Waters
EBSA	Ecologically or Biologically Significant Marine Areas
EUC	Equatorial Undercurrent
LNAM	Local Normalized Angular Momentum
LOW	Local Okubo-Weiss
MJO	Madden-Julian oscillation
MPA	Marine Protected Area
NAW	North Atlantic Waters
NBC	North Brazil Current
NBUC	North Brazil Undercurrent
NBUCc	North Brazil Undercurrent counterflow
NEC	North Equatorial Current
NECC	North Equatorial Countercurrent
OMZ	Oxygen Minimum Zone
OW	Okubo-Weiss
PIRATA	Prediction and Research Moored Array in the Tropical Atlantic

REVIZEE	*Avaliação do Potencial Sustentável de Recursos Vivos na Zona Econômica Exclusiva* (Sustainable Potential Assessment of the Living Resources at the Exclusive Economic Zone)
SAW	South Atlantic Waters
SEANOE	SEA scieNtific Open data Edition
SEC	South Equatorial Current
cSEC	central branch of the South Equatorial Current
eSEC	equatorial branch of the South Equatorial Current
nSEC	northern branch of the South Equatorial Current
sSEC	southern branch of the South Equatorial Current
SECC	South Equatorial Countercurrent
SEUC	South Equatorial Undercurrent
SSH	Sea surface height
SST	Sea surface temperature
TIW	Tropical Instability Wave
UNESCO	United Nations Educational, Scientific and Cultural Organization
VMADCP	Vessel Mounted Acoustic Doppler Current Profiler
WOA	World Ocean Atlas
WOD	World Ocean Database

Abstract

The South Equatorial Undercurrent (SEUC) is the northermost equatorial countercurrent of the South Atlantic Ocean. Having been described in the late 1970's, this jet has been depicted as lower tropical pycnocline-subpycnoclinic current that flows eastward crossing the Atlantic Ocean in the 3.5°S-5.5°S latitudinal band. Its origin site is nearby the western boundary, but how this jet is formed and organizes itself is theme that has not been settled in the scientific community so far. Some authors credit the SEUC genesis due to the feeding by the western boundary current system. Others consider that the SEUC is formed by interior sources, such as the equatorial branch of the South Equatorial Current (eSEC) as it approaches the Brazilian continental margin. Finally, there are others who compromise both approaches mentioning that the SEUC genesis is seasonally-dependent and its sources may vary along the year. However, most of this studies used one-two cruise synoptic observations and/or limited float data. This present work aims to reexamine this topic by obtaining a higher resolution, quantitative picture of the SEUC origin site employing hydrographic and current profiler data from 25 surveys in the area. It complements the observational information by exploring the 1993-2018 assimilative GLORYS12V1 global reanalysis. The analysis and interpretation of 13 selected cruises that best captured the SEUC suggested - through the construction vertical section and stream function maps - that the North Brazil Undercurrent (NBUC) is the main source of water volume to the SEUC. The SEUC orgin seems to be closely related to a southernmost of the multiple retroflections of the NBUC-North Brazil Current (NBC) system. However, unlike all others, the retroflection lobe is cyclonic, and not anticyclonic. In addition, the sometimes called NBUC counterflow (or NBUCc for short) is in fact and overshoot of the so-called primary crest of the retroflection structure, and very likely the SEUC begining. The site location of the NBUC retroflection is that of the shelf projection of the Cape Calcanhar (5.5°S), where the Brazilian margin veers drastically from a meridional orientation to virtually 45° westward of the north direction. In addition to the veloctiy mapping, a regional water mass analysis was carried out to reveal that lower salinity, high dissolved oxygen content, and therefore compatible with the SACW flowing in the NBUC, dominates the SEUC near its origin location. The uneven distribution of the 13 analyzed cruises led us to rule out the possiblity of seasonaly alternating sources of SEUC feeding. The NBUC source is markly relevant throughout the year. The use of the numerical GLORYS12V1 outputs allowed for three complementing and relevant results, after a detailed quantitative assessment of the model skills in the study area. The first result was to compute a 25-year climatology of the SEUC birth site, calculate the volume transport balance and show that the NBUC feeding cannot be discarded as the most important source for the SEUC formation. A second relevant finding is that the the use of AMEDA eddy-detecting algorithm allowed to separate three large bands rich in vortical activity. The northeast band (2.5°S-4.5°S,35°W-28°W) is dominated by anticyclones; the southeast band (4.5°S-6.5°S,35°W-28°W) is dominated by cyclones and the western boundary

(0°-3.5°S,39°W-35°W) band is also dominanted by cyclones. The first two zonal bands are separated by a slimmer region were both polarities are found. All this is indicative of the presence of a wave pattern characteristic of separating jets from a retroflection structure. Moreover, the inspection of countless model snapshots revealed that these waves are unstable - probably baroclinic Tropical Instability Waves- already reported for the region and related somehow withthe SEUC dynamics. The third and, perhaps the most intriguing, of the three results of the numerical output analysis is that the NBUC retroflection itself is unstable, and sheds about 7 intrapycnoclinic cyclones per year. These rings keep flowing northwestward bordering the NBC and probably reach the equator.

Keywords: Western boundary currents; South Equatorial Undercurrent; Current retroflection; Eddy shedding.

Resumo

A Subcorrente Sul Equatorial (SEUC) é a contracorrente equatorial situada mais ao norte no Oceano Atlântico Sul. Tendo sido descrita no final dos anos 1970, esse jato oceânico tem sido retratado na literatura como uma corrente de picnoclina tropical inferior e subpicnoclina, que flui para leste cruzando o Atlântico Tropical entre 3.5°S-5.5°S. Seus sítio de origem ocorre nas proximidades do contorno oeste, mas como o jato é formado e se organiza para cruzar o Atlântico ainda é tema de controvérsia na comunidade científica. Alguns autores creditam a gênese da SEUC ao suprimento de volume pelo sistema de correntes de contorno oeste. Outros autores consideram que a SEUC é alimentada por fontes interiores, tal qual um giro anticiclônico do ramo equatorial da Corrente Sul Equatorial (eSEC) à medida que esse se projeta sobre a margem continental Brasileira. Outros autores ainda tentam concatenar as duas hipóteses especulando que a gênese da SEUC apresenta variação sazonal e que há alternância nos contribuidores de sua formação. Entretanto, a revisão dos trabalhos pretéritos revela que a maioria dos estudos conduzidos na região da SEC se valeram de 1-2 cruzeiros sinóticos apenas. Outros, utilizaram-se de dados de flutuadores restritos a uma determinada faixa de profundidade. Há ainda os estudos mais antigos que se utilizaram de cálculo geostrófico tradicional, apesar das limitações da aplicação deste método numa região quase-equatorial. O presente trabalho se dispõe a reexaminar esse tema através da obtenção de um figura quantitativa, de alta resolução espacial sobre a origem e formação da SEUC através do emprego de perfilagens de hidrografia e velocidade de 25 cruzeiros quase-sinóticos disponíveis na área. Este trabalho complementará as informações obtidas pelas observações explorando a reanálise assimilativa global GLORY12V1. A análise e interpretação de 13 (dos 25) cruzeiros selecionados que melhor capturaram a SEUC sugeriram - através da construção de mapas horizontais de função de corrente e seções verticais de velocidade - que a Subcorrente Norte do Brasil (NBUC) é a mais importante contribuidora à formação da SEUC em termos de volume de água. A origem da SEUC parece estar proximamente relacionada à mais austral das múltiplas retroflexões do sistema NBUC-Corrente Norte do Brasil (NBC). Entretanto, ressaltamos que ao contrário das demais, o lobo de retroflexão é ciclônico, e não anticiclônico. Adicionalmente, o que é algumas vezes chamado na literatura de contrafluxo da NBUC (ou NBUCc) se trata provavelmente da crista primária da retroflexão adjacente ao lobo ciclônico primário e, portanto, demarca provavelmente o início da SEUC. A localização do sítio de formação da retroflexão da NBUC é aquele nas circunvizinhanças da projeção na margem continental do Cabo do Calcanhar (5°S), onde a margem Brasileira guina de uma orientação praticamente meridional para uma inclinada 45° à esquerda do norte verdadeiro. Em adição aos mapas de velocidade, conduzimos uma análise de massas de água regional, que revelou que águas de relativamente baixa salinidade e altas concentrações de oxigênio dissolvidos, que são compatíveis com águas oriundas da NBUC, dominam as características da SEUC próximo a seu sítio de formação. A distribuição desigual,

mas cobrindo todas as estações do ano, também revelam que não há variação sazonal de contribuidores de formação da SEUC. A NBUC é a principal formadora ao longo de todo o ano. O uso das saídas numéricas da climatologia GLORYS12V1 permitiram-nos três resultados finais conclusivos ao presente tema. O primeiro resultado foi o cálculo de uma climatologia de 25 anos sobre o sítio de origem da SEUC, com a qual calculamos o balanço do transporte de volume e mostramos que a contribuição da NBUC não pode sob nenhuma hipótese ser descartada também via este outro cálculo. O segundo resultado, obtido através da aplicação do algoritmo AMEDA de detecção dos vórtices, permitiram a identificação de três bandas onde a formação, ocorrência e ou propagação de vórtices é intensa. A banda nordeste (2.5°S-4.5°S,35°W-28°W) é dominada por anticiclones; a banda sudeste (4.5°S-6.5°S,35°W-28°W) é dominada por ciclones; e a banda do contorno oeste (0°-3.5°S,39°W-35°W) também é dominada por ciclones. As primeiras duas bandas são separadas por uma delgada região onde vórtices de ambas polaridades são encontrados. Essas estruturas são indicativas da presença de um padrão característico de jatos em separação de estrutura de retroflexão. Acrescentamos a isso, a inspeção de inúmeros campos instantâneos do modelo que revelam se tratam de ondas instáveis - que provavelmente estão associadas a ondas de instabilidade tropical - já reportadas para esse região de estudo, e que estão relacionadas com a dinâmica da NBUC. O terceiro achado, e provavelmente o mais intrigante, é que a retroflexão da NBUC propriamente dita também é instável e emite cerca de sete ciclones intrapicnoclínicos por ano. Esses anéis vorticais, após a emissão, continuam a se propagar para noroeste, ao longo da borda externa da NBC, e provavelmente atingem o equador.

Palavras chave: Correntes de contorno oeste; Subcorrente Sul Equatorial; Retroflexão da corrente; Emissão de vórtice.

1

INTRODUCTION

1.1 The Western Boundary Current System

The mean circulation in the tropical Atlantic presents the South Equatorial Current (SEC) crossing the ocean basin and flowing westward. The SEC is identified in three main branches: the northern branch (nSEC) around 2°N, limited southward by the South Equatorial Undercurrent (SEUC); the central branch (cSEC) around 5°S, bound northward by the SEUC and southward by the South Equatorial Countercurrent (SECC); and the southern branch (sSEC), a multi-banded jet reaching the Brazilian coast between 11°S and 30°S (PETERSON; STRAMMA, 1991; SILVA et al., 2009; LUKO et al., 2021). The western boundary current system of the tropical Atlantic has its origin from the sSEC, which correspond to the northern portion of the South Atlantic Subtropical Gyre and exhibit multi-level bifurcations (STRAMMA, 1991; RODRIGUES; ROTHSTEIN; WIMBUSH, 2007). At the surface level, the Brazil Current (BC) is formed from the sSEC bifurcation around 14°S and the North Brazil Undercurrent (NBUC) is generated from the sSEC bifurcation at the picnoclinic level (100 - 500m) around 20°S, receiving water volumes flowing northward from the 18°S, 14°S and 11°S sSEC bands and also from the surface sSEC bifurcation around 14°S (STRAMMA; ENGLAND, 1999; BOEBEL et al., 1999; LUKO et al., 2021). According to Rodrigues, Rothstein e Wimbush (2007), the sSEC bifurcation reveals a seasonal spatial variability as a result of the Intertropical Convergence Zone (ITCZ) migration, influencing the western boundary current transports. Thus, as the sSEC bifurcation is located at a more southern position, the northward NBUC transport increases and the southward BC transport decreases; in contrast, when the sSEC bifurcation is north of its mean position, the NBUC transport decreases and the BC transport increases. Figure 1 shows the schematic circulation of the main surface and subsurface currents at the western South and tropical Atlantic, illustrating the components described hereafter.

The NBUC is a permanent western boundary current flowing northward along the Brazilian northeast coast. Since the region presents a southwestward Ekman drift, the current has a subsurface core at approximately 200m depth, reaching depths of 1100m (SILVEIRA; MIRANDA; BROWN, 1994; STRAMMA; FISCHER; REPPIN, 1995; SCHOTT; FISCHER;

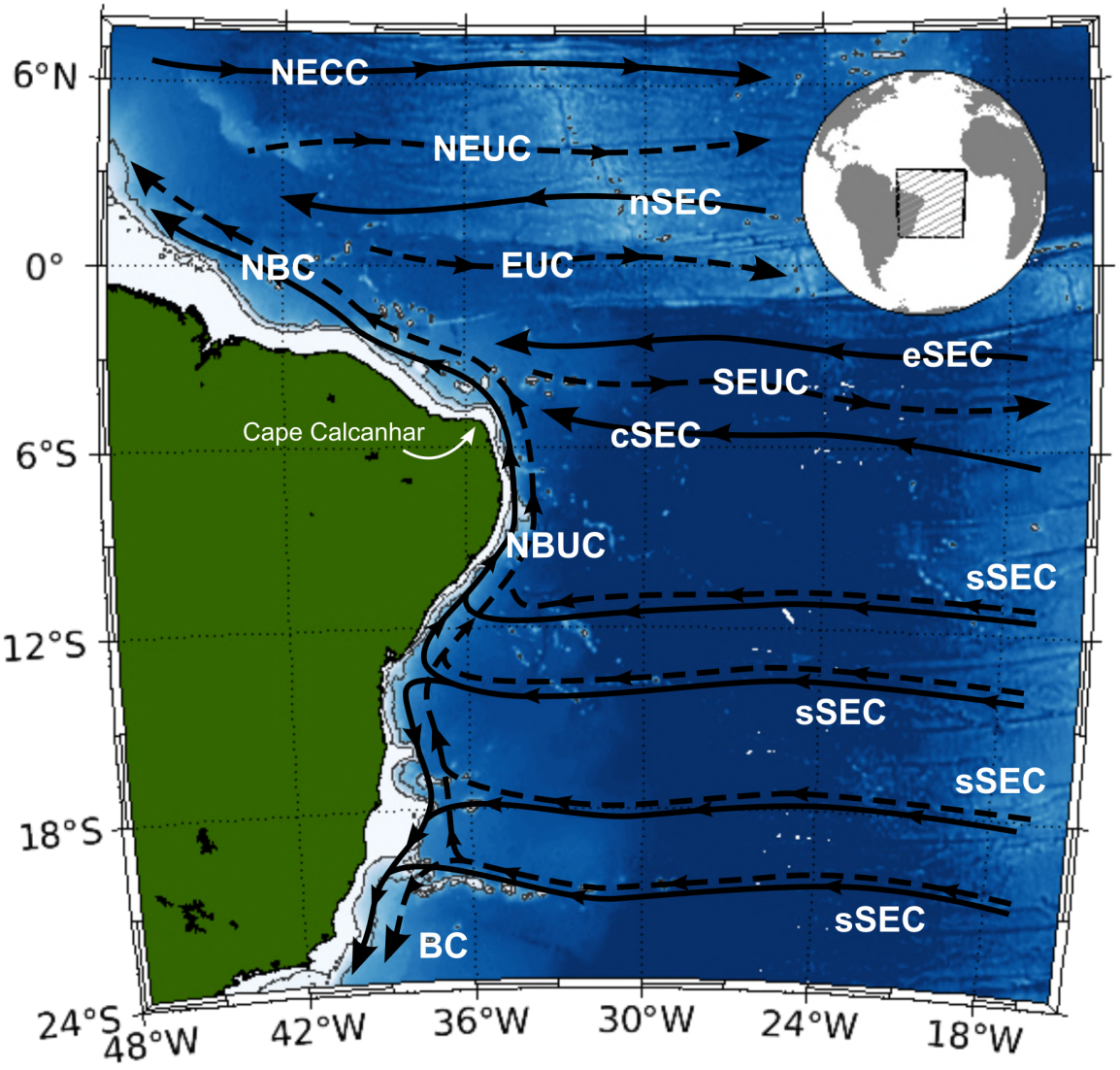

Figure 1 – Schematic map of the upper tropical Atlantic circulation. Surface currents are represented in solid black lines, and subsurface currents are in dashed black lines. Isobaths of 100m and 2000m are highlighted in gray lines. *SEC, South Equatorial Current; sSEC, southern branch of the SEC; cSEC, central branch of the SEC; eSEC, equatorial branch of the SEC; nSEC, northern branch of the SEC; BC, Brazil Current; NBUC, North Brazil Undercurrent; NBC, North Brazil Current; SEUC, South Equatorial Undercurrent; EUC, Equatorial Undercurrent; NEUC, North Equatorial Undercurrent; NECC, North Equatorial Countercurrent.*

STRAMMA, 1998). Long-term mooring observations at 11°S indicate transport values ranging seasonally from 10 Sv to 45 Sv. These measurements also show the NBUC mean transport of 1.6 Sv between the surface and the 24.5 kg m^{-3} isopycnal, it is 12.9 Sv from the 24.5-26.7 kg m^{-3} isopycnals layer and is 10.9 Sv from the 26.7 kg m^{-3} down to the 32.15 kg m^{-3} isopycnal (SCHOTT et al., 2002; HUMMELS et al., 2015). At 5°S, NBUC mean transport obtained from underway ADCP data showed no siginificant differences from the values found at 11°S, and seasonal variability with maximum in July and minimum in October-November (SCHOTT et al., 2002; VELEDA et al., 2011). Some authors, such as Silveira, Miranda e Brown (1994),

Stramma, Fischer e Reppin (1995), Silva et al. (2009), have also shown the presence of a southward flow off the Brazilian northeast margin at the eastern side of the NBUC between 5.5°W and 10°W. Although the source is still unclear, these authors consider the possibility of the counterflow being originated from the deep cSEC southward deflection before reaching the coast, or from the NBUC recirculation, or even that the NBUC counterflow is fed by the SEUC which might turn to the south. North of 5°S, close to the Cape Calcanhar, the NBUC turns northwestward and the cSEC approaches the Brazilian coast from the east to contribute to the western boundary circulation.

The cSEC is a broad westward equatorial current reaching the Brazilian northeast coast at approximately 4-5°S with transport of 29 Sv and velocities of 0.34 $\pm$ 0.05 m s^{-1} around 30°W (SILVEIRA; MIRANDA; BROWN, 1994; LUMPKIN; GARZOLI, 2005). Some authors consider the cSEC as two different branches of the SEC, accounting the equatorial branch of the SEC (eSEC) as a distinct band between the SEUC and the Equatorial Undercurrent (EUC) around 2-3°S (SCHOTT; FISCHER; STRAMMA, 1998; STRAMMA; ENGLAND, 1999). Near the Brazilian coast, the cSEC superposes the NBUC with a transport of 10.0 Sv at 35°W, becoming the surface-intensified western boundary current known as North Brazil Current (NBC) (SCHOTT; FISCHER; STRAMMA, 1998; GOES; SILVEIRA; WAINER, 2005).

North of the Cape Calcanhar, and where the Brazilian continental margin shifts orientation, the NBUC-NBC system vertical structure - also fed by the cSEC and eSEC - is presented as a jet with two main cores: the initial NBC at the surface and the NBUC signal in subpycnoclinic level, both fed by the additional contributions of the SEC's branches. The combined transport of the cSEC, eSEC and NBUC to form the NBC at 35°W, as calculated by Schott et al. (2003), is of 39.2 Sv flowing northwestward south of 2°S, from surface down to 1200m depth. Further north, after slightly separating from the coast and reattaching around 39°W (KRELLING et al., 2020), the current system continues following the continental margin and becomes a more intensified current at the surface, which marks the transition from the NBUC to the NBC. *In situ* measurements obtained by Goes, Silveira e Wainer (2005), indicated that the transport of the NBUC-NBC system at 41°W reaches 16.2 Sv at the surface layer ($\sigma_\theta <$ 24.5 kg m^{-3}) and 17.6 Sv at the subsurface level (24.5 kg $m^{-3} < \sigma_\theta <$ 26.8 kg m^{-3}). Further downstream, the current presents different retroflections along its path feeding eastward zonal equatorial currents. At 44°W, the seasonal cycle is marked by a maximum transport in June-August and a minimum in December-February from the surface to 300m depth (JOHNS et al., 1998; BOURLES; GOURIOU; CHUCHLA, 1999).

The NBUC-NBC system is responsible for the interhemispheric transport of warm waters from the South Atlantic to the North Atlantic as part of the upper-limb of the Atlantic Meridional Overturning Circulation (AMOC), with a northward net heat transport of 0.74 $\pm$ 0.36 10^{15} W (STRAMMA, 1991; LUMPKIN; SPEER, 2007; RUHS et al., 2015). Moreover, the system is a key element as part of the southern hemisphere subtropical cell and also

as the western component of the wind-driven equatorial gyre (MAYER; WEISBERG, 1993; SNOWDEN; MOLINARI, 2003). We will come back to that point latter.

1.2 The NBUC-NBC Retroflections

The NBUC-NBC system presents various retroflections, which feed some of the equatorial zonal currents, as the western boundary system flows equatorward along the Brazilian coast (Figure 2). From north to south, the NECC, the North Equatorial Undercurrent (NEUC) and the EUC receive waters from the NBC at different times, latitudes and depths (SCHOTT; FISCHER; STRAMMA, 1998; BOURLES; GOURIOU; CHUCHLA, 1999). At the surface layer (surface to $\sigma_\theta = 24.5$ kg m^{-3}, $\approx$ 0-100 m), the NBC retroflects between 6-8°N to feed the NECC, with a marked seasonal cycle. Strong eastward flow is present from June to January, with a maximum velocity in August. Weaker NECC transports are verified from February to May (JOHNS et al., 1998; SILVEIRA; BROWN; FLIERL, 2000). During the period of NBC-NECC

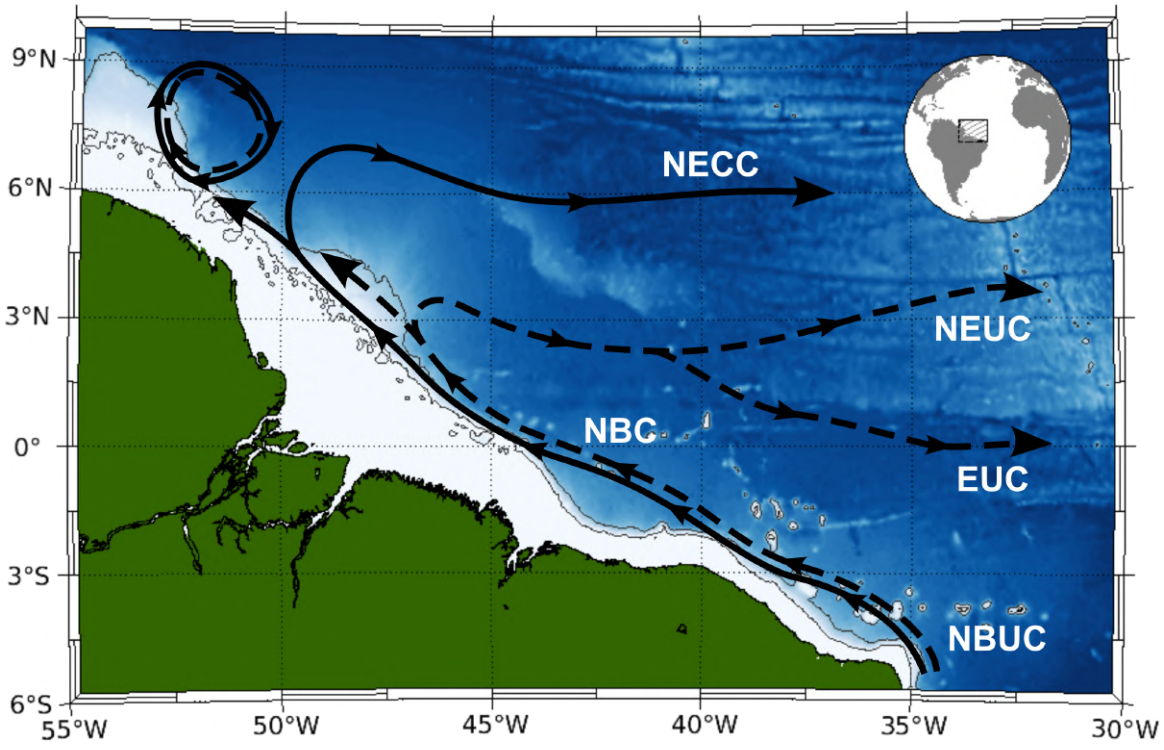

Figure 2 – Schematic map of the NBUC-NBC system retroflections along the Brazilian continental margin. Surface currents are represented in continuous black lines and subsurface currents are in dashed black lines. Isobaths of 100m and 2000m are highlighted in gray lines. *NBUC, North Brazil Undercurrent; NBC, North Brazil Current; EUC, Equatorial Undercurrent; NEUC, North Equatorial Undercurrent; NECC, North Equatorial Countercurrent.*

connection, anticyclonic, and even cyclonic eddies, of approximately 450 km in diameter and 1000m thick pinch off from the retroflection flowing northwestward along the South America

coast (RICHARDSON et al., 1994; FRATANTONI; RICHARDSON, 2006; SILVEIRA; BROWN; FLIERL, 2000; WILSON; JOHNS; GARZOLI, 2002).

At the thermocline layer (σ_θ = 24.5-26.8 kg m^{-3}, $\approx$ 100-300m), the NBC separates from the coast and retroflects around 4°N to feed the EUC-NEUC system, which is a single-core eastward current west of 44°W and becomes two distinct currents (NEUC and EUC) east of 41°W (JOHNS et al., 1998; GOES; SILVEIRA; WAINER, 2005). According to Goes et al. (2013), the NEUC presents a maximum velocity of approximately 0.30 m s^{-1} in June-July and a core position between 4-6°N around 23°W. Supplied mostly by the southern hemisphere, the EUC also at 23°W presents a seasonal cycle of minimum transport in March, when the core is in its shallowest position, and of maximum transport in September, when its core is in its deepest position (BRANDT et al., 2014).

All the above mentioned equatorial zonal currents (NECC, NEUC and EUC), which are fed by the NBC at different latitudes and depths, entrain waters with southern hemisphere characteristics. However, there is a northern hemisphere waters contribution from the westward North Equatorial Current (NEC) flow at the northern portion recirculating to these equatorial zonal currents as well (JOHNS et al., 1998; GOES; SILVEIRA; WAINER, 2005). Recirculations and waters exchanges between the equatorial currents, such as between the nSEC and the EUC, have also been observed by other authors (e.g. Bourles, Gouriou e Chuchla (1999)).

1.3 Intraseasonal Variability and Mesoscale Activity

The intraseasonal variability in the upper-ocean plays an important role in vertical fluxes of heat and salt, also affecting the oxygen, nutrient and plankton distributions. The generation of these oscillations may be related to several dynamical processes, such as local or remote wind-forcing, resonance due to coastline geometry, and mean flow instalibilities. Furthermore, if fluctuations are close to the coast, Earth's rotation, density stratification, topography and the presence of the coastline may also influence the intraseasonal variations (ALLEN, 1980; SCHUCKMANN, 2006). The mean flow instabilities are associated with barotropic, due to lateral shear of the currents, and baroclinic instabilities, which is related to the vertical shear of the currents. Large amplitudes signals are observed in the current field at the equatorial Atlantic Ocean in the 10-80-day band, with peaks at 10-40day and 40-60day periods. These features might be realted to wind-driven equatorial waves or tropical instability waves (TIW) (DUEING et al., 1975; HAN et al., 2008). According to Schott et al. (2005), two-month fluctuations were also observed 50 km off-shore in the NBUC domain at the northeast Brazilian coast around 11°S.

The Madden-Julian oscillation (MJO) is an intraseasonal variability mode of 30-50-days period in the tropical troposphere associated with the upper-ocean fluctuations in the tropical

Atlantic ocean between 10°S and 10°N (FOLTZ; MCPHADEN, 2004; SCHUCKMANN, 2006). The wind-driven equatorial waves, consequence of the MJO, are observed as Kelvin waves propagating eastward with aproximatelly 2.35 m s^{-1} speed, 10-40-day and strong 40-60-day variability, mainly forced by zonal winds and also dominant along the equator and east of 10°W (KATZ, 1987; HAN et al., 2008). According to Bunge, Provost e Kartavtseff (2007), Han et al. (2008), Yanai waves were also wind-driven waves observed and numerically analyzed at the tropical Atlantic region with 10-40-day period and forced by meridional winds. These waves always propagate group (energy) from the western boundary toward the ocean interior (JOCHUM; MALANOTTE-RIZZOLI; BUSALACCHI, 2004).

The TIWs are observed in the tropical Atlantic as near-surface Rossby waves with typical periods 10-40 days and wavelengths from 600 to 2600 km propagating with westward phase speed of 0.2-0.5 m s^{-1} between 5°S and 5°N (DUEING et al., 1975; SCHUCKMANN, 2006; DECCO et al., 2018). These waves are generated by mean flow instabilities within the equatorial zonal current system of alternating eastward and westward flows (PHILANDER, 1976). Three different locations at the tropical Atlantic are highlighted by Schuckmann, Brandt e Eden (2008) as sources of energy for the TIWs: (i) 4-5°N band, which receives contribution of the barotropic instability from the nSEC-NECC horizontal shear, and the baroclinic instability from the nSEC vertical shear; (ii) along the equator, which is related to barotropic instability from the nSEC-EUC horizontal shear (JOCHUM; MALANOTTE-RIZZOLI; BUSALACCHI, 2004); and (iii) 4-5°S band, where only the baroclinic instability from the cSEC vertical shear accounts for energy production. The waves as intensified in the upper 100 m of the ocean with energy propagation down to 600m depth (SCHUCKMANN; BRANDT; EDEN, 2008). The waves present a strong seasonality, more intense in May or June to September, in association with the intensification of the trade winds in boreal spring when equatorial zonal currents accelerate (WEISBERG; WEINGARTNER, 1988; FOLTZ; MCPHADEN, 2004). Although present throughout the entire year with low variance, the TIWs show peak on $\approx$ 360 days and on $\approx$ 180 days of annual and semiannual variability respectively (DECCO et al., 2018). Regularly present south of the equator, subsurface TIWs were also observed at the tropical Atlantic ocean, characterized as a distinc feature from TIWs at surface and possibilitating an enhanced vertical mixing by multi-layer shear according to a study conduced by Specht, Jungclaus e Bader (2021). The authors evidenced subsurface TIWs generated through barotropic and baroclinic energy conversions between 0°-4°S.

The coastal trapped waves (CTW) are intraseasonal fluctuations which propagate along the continental slope with the coast to the right on the northern hemisphere and the coast to the left on the southern hemisphere. At the northeast Brazilian margin, CTWs were observed by Veleda et al. (2012) as Kelvin waves of 14-30-days period in 100m depth at 11°S, with equatorward propagating speed of 285 $\pm$ 63 km day^{-1} (3.30 $\pm$ 0.73 m s^{-1}). The author suggest that the CTWs are generated at 22-36°S (or at the "Southeast Brazil Bight") by a combination of wind stress variability and abrupt change in coastline direction.

Mesoscale eddies can trap and transport waters within the eddy core as they advect, being responsables for a global eddy-induced zonal transport of 30-40Sv comparable with the global wind-driven and thermohaline-driven circulations (FLIERL, 1981; ZHANG; WANG; QIU, 2014). According to Zhang, Wang e Qiu (2014), these features can also impact the transports on the western boundary currents and, since they influence the global mass and heat transport, the mesoscale eddies contribute to regional and basin-scale climate variability. Besides mass and heat transport, dissolved carbon, oxygen and nutrients are also carried within the eddy core. Recently, Dossa (2021) used satellites altimetry data from 1993 to 2018 to analyze eddy characteristics, polarity, spatial and temporal distribution, trajectories off Northeast Brazil (37-25°W; 13-1°S). Based on sea surface height (SSH) maps, the authors identified approximately 1950 mesoscale eddy crossed the region, including 76% formed in the region, with amplitudes and radii ranging between 1 and 2 cm and 25 and 205 km, respectively.

Most of previous works in literature at the western tropical Atlantic region focuses on surface eddies, and a limited number of studies have addressed subsurface mesoscale activity in the western tropical Atlantic boundary (SILVEIRA; BROWN; FLIERL, 2000; WILSON; JOHNS; GARZOLI, 2002; KRELLING et al., 2020). North of the Cape Calcanhar ($\approx$ 5°S), where the Brazilian northeast coast changes its orientation, two bights are present along the coast: the Potiguar Bight, centered at 4°S, and the Barreirinhas Bight centered at 1.75°S. Two coastally-trapped eddies are formed associated with these topographic features. As described by Krelling et al. (2020), the Potiguar Eddy is a quasi-stationary subsurface anticyclone related to the NBUC reattachment process off the continental margin with a intraseasonal variability of 20-30-days period in May-June and of 30-days period in September. The authors hypothesize that these oscillations might be linked with the CTWs observed by Veleda et al. (2012). The Barreirinhas Eddies are submesoscale westward-propagating anticyclonic eddies at near-surface level and in pycnoclinic level, occuring mainly from March to August. They are reported to be 1-week-long recurrent events, and are related to the NBC interaction with the continental margin topography (SIMOES-SOUZA et al., 2021). Another study addressing below-surface vortical features in the western boundary tropical Atlantic is associated to the low-frequency presence of anticyclonic southward migrating eddies formed after the interaction between the Deep Western Boundary Current (DWBC) and the topography (Pernambuco Plateau) at 8°S (DENGLER et al., 2004; SCHOTT et al., 2005). As we will present later, the current work investigates subsurface mesoscale activity associated to the NBUC-SEUC-NBC system.

1.4 The South Equatorial Undercurrent

In the Pacific, the Atlantic SEUC counterpart was firstly described by Tsuchyia (1975) and it is called the Southern Subsurface Countercurrent (SSCC) or the Tsuchyia Jet. In the Pacific, more observations are available, and also more numerical and theoretical studies have

been developed than in the Atlantic. Many of these theoretical studies attempted to elucidate the mechanisms behind the SSCC formation, which can be also transported to the SEUC. Some energy sources have been proposed to explain, at least in part, the current dynamics: (i) the equatorward shoaling of the thermocline, as meridional ageostrophic and diapycnal cells form to conserve angular momentum (MARIN; HUA; WACONGNE, 2000; HUA; MARIN; SCHOPP, 2003); (ii) the large-scale zonal slope of the thermocline, as the eastward shoaling of the thermocline is compensated by the poleward migration of the current (JOHNSON; MOORE, 1997); (iii) the EUC, as a result of the balance between the poleward diffusion of relative vorticity associated with the EUC and the poleward advection of planetary vorticity (MCPHADEN, 1984); (iv) the upwelling along the eastern boundary, as Rossby waves carrying the density structure from the upwelling regions converge or intersect creating arrested fronts (MCCREARY; LU; YU, 2002); and (v) the tropical instability waves, as drivers of the current (JOCHUM; MALANOTTE-RIZZOLI, 2004). Such large-scale and regional forcing can be complementary, and processes involving different energy sources are probably associated to the SEUC formation (MENESGUEN et al., 2019). Despite the efforts, we still lack of comprehensive understanding of the currents existence in both Pacific and Atlantic oceans.

The SEUC is a zonal equatorial current observed at subpycnoclinic level, and flowing eastward south of the EUC, at about 4°S. The current shifts poleward from its west-east orientation, also presenting a core rise across the isopycnals as it crosses the Atlantic basin. Further west, at 35°W, the SEUC core is found deeper than 200-300 m depth, and migrates northward to approximately 3°S. The current reaches core depths less than 100 m depth and latitudes of 5.5°S at 10°W, and there is an apparent cessation of the SEUC near 5°W (SILVEIRA; MIRANDA; BROWN, 1994; MARIN; HUA; WACONGNE, 2000; BOURLES et al., 2002). In Table 1, we compilate transport values from measurements reported in previous works at the western Atlantic boundary. These transports were calculated at different longitudes, density/depth ranges and months of the year. Note that Fischer et al. (2008) ensembled the sections obtained with the observations from other studies, e.g. Schott, Fischer e Stramma (1998), and recalculated the transports for the density range of 24.5 - 27.1 kg m^{-3}. As the SEUC flows eastward from around 35°W, it becomes stronger and wider as it reaches 28°W, and gets weaker further east. At its westernmost portion, the subsurface zonal flow presents a wake-like pattern (FISCHER et al., 2008).

Study	**Longitude**	σ_θ **(kg m^{-3}) or Depth**	**Month**	**Transport**
Fischer et al. (2008)	26°W	24.5 - 26.9	Mar	11.2 Sv
Molinari (1982)	26°W	100 m - 700 m	Jul	20.0 Sv
Molinari (1982)	27.5°W	100 m - 700 m	Feb	10.7 Sv
Molinari (1982)	27.5°W	100 m - 700 m	Mar	7.4 Sv
Fischer et al. (2008)	28°W	24.5 - 27.1	Jan	9.5 Sv
Fischer et al. (2008)	28°W	24.5 - 27.1	May	9.9 Sv
Fischer et al. (2008)	28°W	24.5 - 27.1	May	10.3 Sv
Fischer et al. (2008)	28°W	24.5 - 27.1	Aug	11.2 Sv
Cochrane, Kelly e Olling (1979)	30°W	100 m - 700 m	Mar	20.1 Sv
Bourles, Gouriou e Chuchla (1999)	30°W	24.5 - 26.75	Mar	3.0 Sv
Fischer et al. (2008)	31°W	24.5 - 27.1	Jun	5.4 Sv
Schott, Fischer e Stramma (1998)	31°W	24.5 - 1000 m	Nov	3.5 Sv
Cochrane, Kelly e Olling (1979)	33°W	100 m - 700 m	Mar	15.9 Sv
Silva et al. (2021)	33.5°W	100 m - 400 m	Sep	5.6 Sv
Silva et al. (2021)	33.5°W	100 m - 400 m	Apr	3.8 Sv
Silveira, Miranda e Brown (1994)	34°W	100 m - 800 m	May	15.4 Sv
Silveira, Miranda e Brown (1994)	34.5°W	10 0 m - 800 m	May	12.7 Sv
Goes, Silveira e Wainer (2005)	35°W	24.5 - 27.0	Feb	4.6 Sv
Fischer et al. (2008)	35°W	24.5 - 27.1	Apr	8.7 Sv
Fischer et al. (2008)	35°W	24.5 - 27.1	Apr	8.9 Sv
Bourles, Gouriou e Chuchla (1999)	35°W	24.5 - 26.75	Apr	2.2 Sv
Fischer et al. (2008)	35°W	24.5 - 27.1	May	3.7 Sv
Fischer et al. (2008)	35°W	24.5 - 26.9	Jun	2.9 Sv
Fischer et al. (2008)	35°W	24.5 - 27.1	Jun	4.0 Sv
Fischer et al. (2008)	35°W	24.5 - 27.1	Jul	4.3 Sv
Bourles, Gouriou e Chuchla (1999)	35°W	26.5 - 26.75	Sep	7.1 Sv
Fischer et al. (2008)	35°W	24.5 - 27.1	Oct	6.1 Sv
Fischer et al. (2008)	35°W	24.5 - 27.1	Nov	3.7 Sv
Fischer et al. (2008)	35°W	24.5 - 27.1	Dec	4.6 Sv

Table 1 – The South Equatorial Undercurrent (SEUC) calculated transport in different longitudes, months, and isopycnal and/or depth ranges from several studies in the literature.

The area of the SEUC origin at the western tropical Atlantic boundary is a very complex region, with different circulation components, topographic interactions and dynamic forcings acting simutaneaously. Besides, the lack of observations at this specific area makes it even

more complex. Despite the efforts to explain the origin of the SEUC waters at the western boundary region, it remains a debatable topic among the scientific community. It is commonly established the feeding of the SEUC from recirculations at its northward and southward portions, as the deeper parts of the eSEC and the cSEC, respectively. At the westernmost region, some studies indicate no connection between the NBUC-NBC system, only contributions from the eSEC (SCHOTT; FISCHER; STRAMMA, 1998; BRANDT et al., 2006; HUTTL-KABUS; BONING, 2008). First identified by Cochrane, Kelly e Olling (1979), other authors have indicates the likely existence of a NBUC retroflection to feed the SEUC Silveira, Miranda e Brown (1994). Other studies found relatively high-oxygen concentrations, characteristic from the South Atlantic waters, embedded in the SEUC oxygen-poor waters, which pointed to the NBUC-SEUC connection (MOLINARI, 1982; ARHAN et al., 1998; GOES; SILVEIRA; WAINER, 2005). According to Silva et al. (2021), the connection occurs seasonally, only during spring. However, a small observational coverage was used in the latter work to infer the seasonallity of the NBUC-SEUC connection. On the other hand, other efforts, such as Bourles, Gouriou e Chuchla (1999) and Jochum e Malanotte-Rizzoli (2004), even suggest the EUC might also feed the SEUC at its western portion. The Figure 3 illustrates a schematic map of the circulation at the SEUC origin region, with the possibilities of connections between the components, as suggested in previous works already mentioned above.

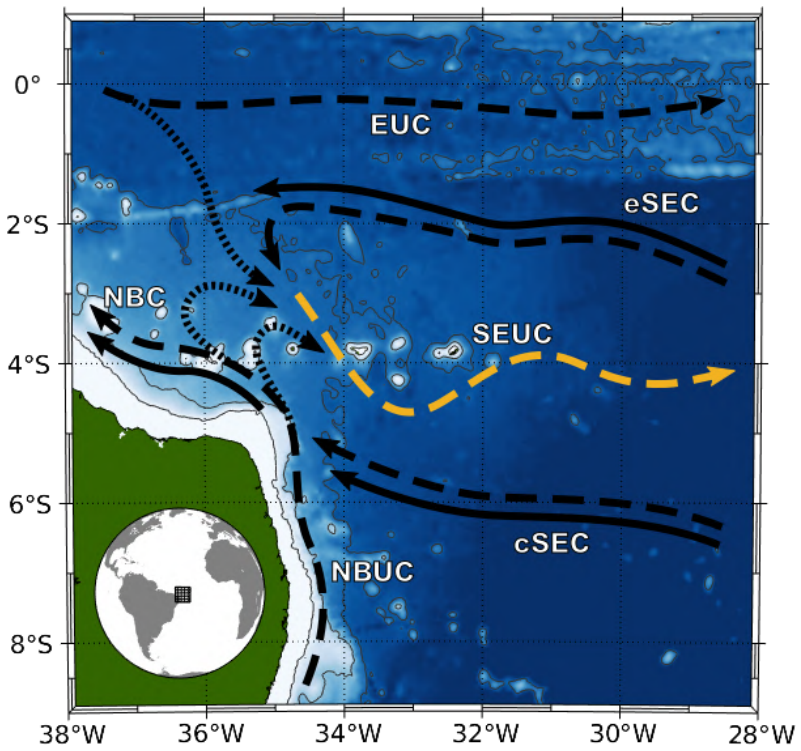

Figure 3 – Schematic circulation map at the SEUC origin region and possible connections (dotted lines) between the SEUC and other components. Continuous lines represent surface currents and dashed lines indicate subsurface currents or part of currents.

1.5 Motivation and Ecological Relevance

The region off the Brazilian northeast coast presents important geomorphological features: the Northern Brazilian Chain, between 1-4°S and 37-39°W; and the Fernando de Noronha Chain, between 3-5°S and 32-38°W (Figure 4). The diversity of these features, such as guyots, seamounts and islands, offers a large amount of solid substrate under the reach of solar radiation and, in a tropical oligotrophic environment, the geological formations are considered oases for marine life, providing shelter for high biodiversity (SCHMIDT; SCHMINCKE, 2000; SAMADI et al., 2006). Moreover, the interaction between the geomorphological features' topography and the ocean circulation induces dynamical processes responsable for the enrichment of nutrients necessary for the local productivity (TRAVASSOS et al., 1999; MCGILLICUDDY, 2015).

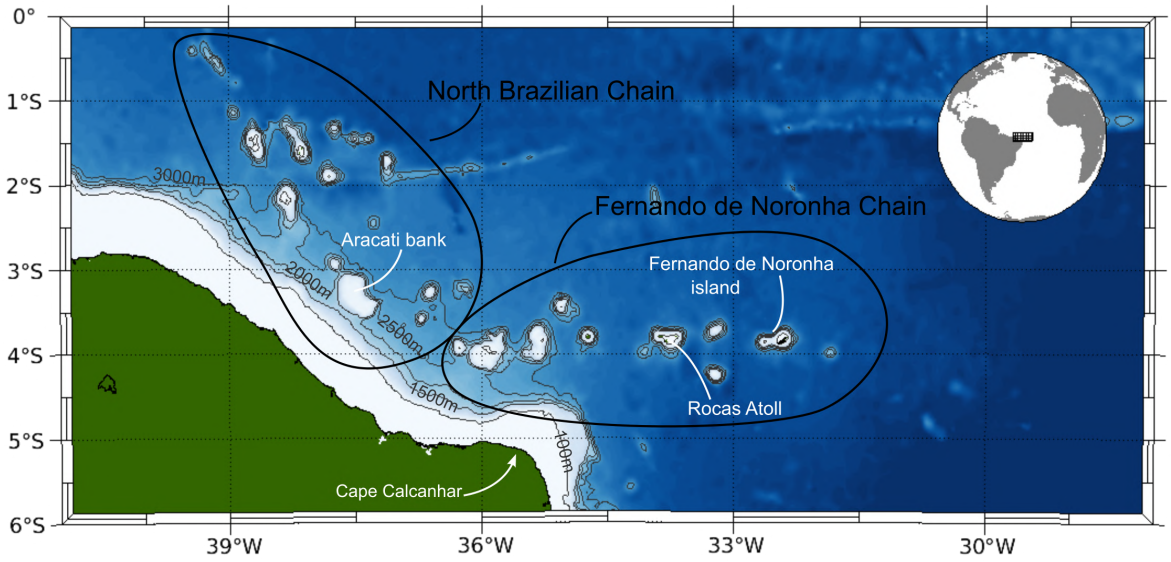

Figure 4 – The main topographic features at the study region: the North Brazilian Chain and the Fernando de Noronha Chain, the Fernando de Noronha island, the Rocas Atoll and the Aracati bank.

Accordingly, the Northern Brazilian Chain and the Fernando de Noronha Chain were identified as a Marine World Heritage by the United Nations Educational, Scientific and Cultural Organization (UNESCO) in 2001 and as one of the Ecologically or Biologically Significant Marine Areas (EBSA) in 2012 (COP11, UN, 2012; SCBD, 2014; UNESCO, 2018). Recent observations analyzed by Silva et al. (2021) and numerical modeling results (CMEMS, 2018) indicate the action of the SEUC on these highly biodiverse-value ecosystems. The advance in the knowledge of the current dynamics off the Northeast Brazilian continental margin, and more specifically the SEUC variability, provides important contributions to the identification and quantification of the biogeochemical components and marine life distribution in the region.

The mesoscale activity also plays an important role in the ecosystem balance. When

generated adjacent to the continental margin, the mesoscale features trap coastal waters and transport them to the oligotrophic ocean interior. From the biogeochemical perspective, they are also relevant as physical processes capable of generating nutrient fluxes upward to the surface, contributing to 20-50% of the world primary production (FAKOWSKI et al., 1991; MCGILLICUDDY, 2015). This assoaciated increase in biological productivity yields favorable habitats from high to low trophic levels (GODO et al., 2012; SANCHEZ-VELASCO et al., 2013). Besides the higher primary production, these eddy environments are also associated with abundance, growth and settlement of fish larvae, fish migration and with juvenile fish recruitments (LUO et al., 2015; SHULZITSKI et al., 2016). Therefore, contributions to the understanding of the mesoscale fields at the western boundary currents and the tropical Atlantic circulation possibilitate the growth in knowledge on climate and ecosystem dynamics and variabilities.

Advances in improving the understanding of the large and mesoscale scale circulation enable the construction of offshore structures and equipments for oil and gas exploration, accident prevention and mitigation of the economic activity consequences. Moreover, it allows a better elaboration of contigency plans of environmental disasters, such as oil and gas accidents. In August 2019, over 7000 tonnes of oil (petroleum) were removed from beaches caused by an oil spill of unclear source spread over the more than 860 localities, hitting over 40 Marine Protected Areas (MPA) and causing severe socioeconomic impacts (ARAUJO; RAMALHO; MELO, 2020; GONCALVES et al., 2020; LADLE et al., 2020). In October 2021, the National Agency of Petroleum, Natural Gas and Biofuels (ANP) offered five blocks at an auction for oil and gas exploitation just south of the Fernando de Noronha Chain between 4°S and 5°S, evidencig the need for an accurate comprehension on the current dynamics of the region (MAIDA et al., 2021).

The investigation of the subsurface circulation nearby highly biodiverse sites and productive coastal areas in the tropical Atlantic is important for other reasons rather than providing an environmentally controlled oi and gas exploration. The intermediate layers of the ocean present minima of oxygen when compared with upper-layers and deep levels, consequence of the balance between ventilation, circulation and biogeochemical forcing. In the eastern tropical Atlantic, an oxygen minimum zone (OMZ) is found at the 100-700m depth with decreasing trends, which affects important biogeochemical cycles and impacts the function of marine ecosystems (KEELING; ARNE; GRUBER, 2010; BRANDT et al., 2010). According to Brandt et al. (2010), Brandt et al. (2015), the advection of oxygen is one of the possible sources for the OMZ and eastward current bands be generally associated with oxygen-rich waters. This advection results from transport of these high-oxygen waters from the western boundary towards the depleted eastern tropical Atlantic region. It represents a ventilation pathway for the OMZ. In fact, Duteil et al. (2014) points out that the SEUC strength might be a critical factor to the oxygen trends in the upwelling system off the African coast. Therefore, a better comprehension of the western boundary circulation and also the SEUC origin could

contribute to the understanding of the possible sources/sinks of oxygen for the tropical Atlantic OMZ in a global warming scenario.

Another important motivation to conduct studies in subpcynoclinc current dynamics concerns the so-called "AMOC puzzle". The AMOC, illustrated in Figure 5, is responsible for the mass and heat interhemispheric transport and sequestration of carbon dioxide. This circulation influences the sea surface temperature (SST), precipitation and sea level pattern at regional and global scales (SHMITZ; MCCARTNEY, 1993; LORBACHER et al., 2010; FERRARI; FERREIRA, 2011; PEREZ et al., 2013). In the subtropical Atlantic, the fluctuations in the AMOC have been suggested to impact Atlantic SST, with further impacts on weather and climate (DUCHEZ et al., 2016). The subtropical gyres of the North and South Atlantic have become warmer and more saline (DURACK; WIJFFELS, 2010; LUMPKIN; GARZOLI, 2011). These studies showed that the water transport from the Indian Ocean to the South Atlantic through the Agulhas leakage has been increasing in recent years. According to Hummels et al. (2015), the observed changes in the upper layer of salinity and oxygen in the western tropical Atlantic boundary for the last decade are consistent with the increase in the Agulhas leakage. However, recent studies based on long-term measurements at 26°N and climate model simulations affirm that the Atlantic Meridional Overturning Circulation is slowing down and losing its stability (RAHMSTORF et al., 2015; SROKOSZ; BRYDEN, 2017; LIU et al., 2017). Furthermore, the IPCC's Report (AR6) released recently (August 2021), stated that it is very likely the AMOC will decline throughout the 21st century (IPCC, 2021). Those findings suggest that the AMOC decline is not just a fluctuation or a linear response to increasing temperatures, but it is related to the approaching of a critical threshold beyond which the circulation system could collapse in the future. It is somehow intriguing once incompatible to the observed increasing of the Agulhas leakage. One explanation comes to the possibility of a long-term intensification of the connections between tropical western boundary circulation (NBUC-NBC system) and eastward zonal flows via NBC-NBUC retroflections, which diverts part of the northward meridional AMOC flow to feed NECC, NEUC-EUC, and SEUC (Figures 2 and 3). In fact, Brandt et al. (2017) showed from mooring observations that the EUC strengthened by more than 20% from 2008 to 2018. According to these authors, the EUC intensification is found to be mainly forced by trade wind changes in the western tropical North Atlantic. All those findings reinforce the

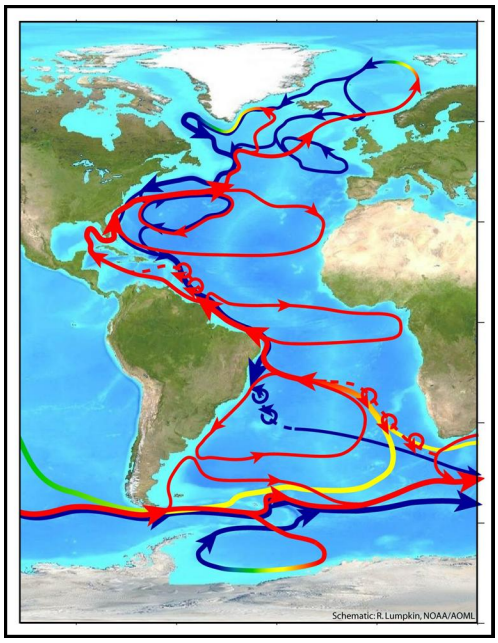

Figure 5 – The Atlantic Meridional Overturning Circulation (AMOC). Source: Rick Lumpkin (NOAA/AOML).

need to investigate the origin and variability of the still much less studied SEUC.

1.6 Scientific Hypotheses

Despite all the efforts to better understand the tropical Atlantic circulation, and more specifically the complex western boundary current system, some scientific questions remain open. The SEUC is relatively well characterized at its eastern portion redwe need references here. However, little is known in terms of its characterization and time variability at its origin site in the western portion of the tropical Atlantic. In particular, the possible NBUC-NBC system retroflection to feed the eastward SEUC remains doubtful and is it is still subject to debate and disagreement in the scientific community. In other words, if the NBUC-NBC-SEUC connection exists, the space and time variability of the process is still unknown. Also, it is known that most of retroflecting currents are unstable redreferences here too, and present rich mesoscale associated. The retroflection to feed the SEUC and its variability has been neither confirmed nor yet adressed in a quantitave manner.

Therefore, the main hypothesis that guides this study is:

The SEUC is connected with the NBUC-NBC system year-round through an unstable NBUC subpycnoclinic retroflection, which feeds the meandering, eastward-flowing SEUC.

Two supplementary hypotheses, regarding the NBUC-SEUC-NBC connection, are also tested. They are:

- The variability of the NBUC-NBC system retroflection feeding the SEUC is driven by the changes in the NBUC intensity, which is linked with the latitudinal variation of the sSEC bifurcation;
- The meandering SEUC flow is surrounded by intense mesoscale activity with cyclonic (anticyclonic) band south (north) of the current of eddies flowing westward.

1.7 Objectives

Considering the scientific questions raised in the previous section, the present study aims to investigate the connection between the NBUC-NBC system and the SEUC. Therefore, in order to achieve that, the specific objectives are:

- To describe the western portion of the SEUC from synoptic observations;

- To investigate the NBUC-SEUC connection through a regional water mass analysis, stream function mapping, and transport calculation;
- To analyze the time variability of the NBUC retroflection using reanalysis results;
- To examine and to characterize the mesoscale SEUC eddies and their (north)westward propagation along the NBC using outputs from global ocean reanalysis.

In order to present the test of the formulated hypotheses and the fulfillment of the objectives of the present work, the document is organized as follows: Chapter 2 describes the Data and Methods used in this effort; Chapter 3 focus on an observational characterization, searching for evidences about the NBUC-SEUC connection and mesoscale activity along the SEUC flow; Chapter 4 is dedicated to explore the results obtained from numerical global model reanalysis for the study region, which allows to reach broader continuous spatial and time scales. In this latter section, after validating the reanalysis, we seek to understand the mass transport balance in the region and the mesoscale processes associated to the SEUC eddies. Finally, Chapter 5 summarizes the main findings, concludes, and points out perspectives for future investigations.

2

DATA AND METHODS

2.1 Observational Dataset

As far as we know, observational efforts in the western tropical Atlantic have been not fully explored in examining the NBUC-SEUC-NBC connection. The present work uses different datasets as an attempt to capture distinct physical scnearios and processes within the region the aformentioned connection occurs. These sets of observations enable us to survey the SEUC western portion at different times and locations. The overall gsthered dataset consists of several hydrographic and current (quasi)-synoptic measurements obtained during various national and international cruises made available to us.

We analyze 25 oceanographic campaigns performed in the SEUC formation region, such as: Operação Oceano Nordeste (ONE) I and II; Prediction and Research Moored Array in the Tropical Atlantic (PIRATA) I to XIX (SERVAIN et al., 1998; BOURLES et al., 2019); Acoustics along the Brazilian Coast (ABRACOS) I and II (BERTRAND et al., 2015; BERTRAND et al., 2017); METEOR M130 and M145; and lastly *Avaliação do Potencial Sustentável de Recursos Vivos na Zona Econômica Exclusiva program - Nordeste* (REVIZEE-NE) IV. From the 25 analyzed campaigns, 13 of these cruises (Table 2 and Figure 6) present observation within the necessary horizontal and vertical extension, as well as the needed quality, to capture the circulation dynamic of the NBUC-SEUC-NBC system. The hydrographic data obtained with *Conductivity-Temperature-Depth* (CTD) equipment were preliminary processed with the original SeaBird software common to all cruises' sampling, followed by standard quality-control procedures (<https://repository.oceanbestpractices.org/handle/11329/378>). The current profiling data, which were taken with the Ship-Mounted Acoustic Doppler Current Profiler (SADCP), instrument were processed with the Common Ocean Data Access System (CODAS) package, developed by the University of Hawaii (<https://currents.soest.hawaii.edu/docs/adcp_doc/index.html>). Specifically for the PIRATA cruises, underway current measurements were also processed with CASCADE (*Chaîne Automatisée de Suivi des Courantomètres Acoustiques Doppler Embarqués*) software, developed at the Ifremer Laboratoire de Physique de Océans (KERMABON et al., 2018; ARAUJO et al., 2021).

Cruise	Date	Austral season	Research vessel
REVIZEE NE IV	Oct-Nov 2000	Spring	Antares
PIRATA IV	Apr-May 2001	Fall	Antares
ONE II	Feb-Mar 2002	Summer	Cruzeiro do Sul
PIRATA V	Apr 2002	Fall	Antares
PIRATA VII	Jul-Aug 2004	Winter	Antares
PIRATA XII	Jul-Sep 2010	Winter	Antares
ABRACOS I	Oct 2015	Spring	Antea
PIRATA XVI	Oct-Nov 2015	Spring	Antares
METEOR M130	Sep 2016	Spring	Meteor
ABRACOS II	Apr 2017	Fall	Antea
PIRATA XVII	Oct-Dec 2017	Spring	Vital de Oliveira
METEOR M145	Mar 2018	Summer	Meteor
PIRATA XVIII	Sep-Nov 2018	Spring	Vital de Oliveira

Table 2 – Oceanographic cruises analyzed at the western boundary region.

Another source of observational data was the World Ocean Database (WOD). The WOD is a collection of scientific ocean profile data formatted uniformly, quality controlled, made freely available covering the whole planet (BOYER et al., 2018). Acquired from several types of equipaments including CTD, moored buoys and profiling floats, the database provide information of biotic and abiotic variables, such as temperature, salinity, chlorophyll, dissolved oxygen and dissolven inorganic nutrients. The database latest updated version, the WOD18 contains over 15 million oceanographic casts accounting for more than 3 billion profile measurements, which are distributed in originally observed depths levels and also in interpolated standard depths levels (GARCIA et al., 2018). For the present work, the WOD18 was another source of observational data providing 7825 casts of temperature, salinity and oxygen ocean profile measurements for the regional water mass analysis at the western tropical Atlantic and more specifically in the SEUC formation site. Figure 6 illustrates the complete hidrographic dataset coverage, which is analyzed in the present study, exhibiting the data collected during the cruises cited above as well as CTD casts from WOD18. Table 2 lists the cruises from where SADCP velocity transects were obtained.

The neutral density variable was calculated from temperature and salinity fields obtained from the Multi Observation Global Ocean ARMOR3D product developed and delivered by the Copernicus Marine Environment Monitoring Service (CMEMS). The L4 product is a combination of *in situ* and satellite data from surface to 5500m depth with a weekly frequency

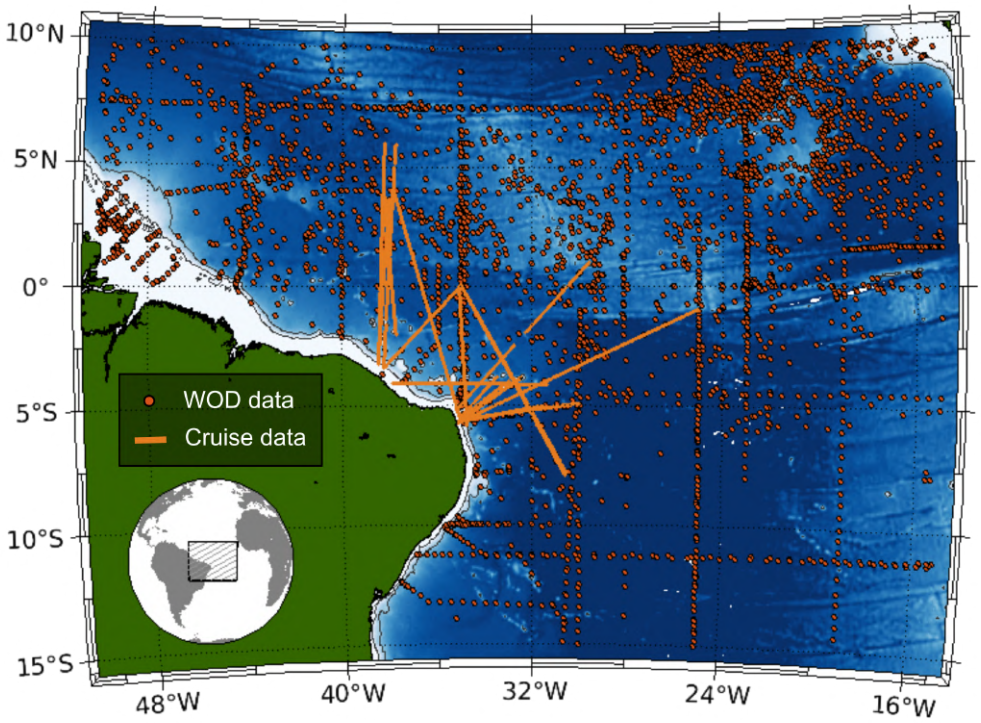

Figure 6 – *In situ* measurements obtained from oceanographic cruises campaigns mentioned in Table 2 and from the World Ocean Database (WOD).

from 1993 to 2019, and spatial resolution of $1/4°$ (Multi Observations Thematic Assembly Center, 2020). The satellite data are vertically determined by multiple linear regression method and covariances from historical observations, and then combined with T/S *in situ* profiles by optimal interpolation method. The ARMOR3D product is fed by different sources of data such as Argo profiling floats, WOA18 climatology, both infrared and microwave radiometers, and a conjoint of *in situ* CTD, XBT and moorings measurements (GREINER et al., 2020).

In situ observations referred above are extremelly valuable since they furnish concrete elements of investigation. However, cruise measurements provide only a synoptic perspective of the study area dynamics, i.e space and time resolution are limited to capture the variability and dynamic of the process. Therefore, the use of a numerical product properly validated was made necessary to allow further examination and broaden the investigation of intraseasonal phenomena, as we will see in the next sections.

2.2 Numerical Product

The Mercator Ocean GLORYS12V1 product is a global ocean eddy-resolving reanalysis provided by Copernicus Marine Environment Monitoring System (CMEMS, <https://marine.copernicus.eu/>) with horizontal spatial resolution of $1/12°$, 50 vertical levels and daily temporal resolution from 1993 to 2019 (Mercator Ocean, 2020). The product ocean component is the

NEMO 3.1 ocean/sea-ice general circulation model developed by Madec e Team (2008), with the ORCA12 global configuration of 50 vertical levels developed by the DRAKKAR consortium (MOLINES et al., 2014). It is forced at the surface by the ECMWF ERA-Interim reanalysis, after some specific corrections. All along the simulation, data assimilation is performed using a reduced-order Kalman filter with a 3D multivariate modal decomposition of the background error, which includes an adaptive-error estimate and a localization algorithm. CMEMS along track altimeter data (Sea Level Anomaly – SLA), satellite SST, and sea ice concentration are assimilated, together with *in situ* temperature and salinity vertical profiles from the CORA database (COriolis dataset for Re-Analysis) (DREVILLON et al., 2021; CABANES et al., 2013). Moreover, a 3D-VAR scheme provides a correction for the slowly-evolving large-scale biases in temperature and salinity. The simulation is initialized using the T/S conditions derived from the EN4.2.0 database (GOOD; MARTIN; RAYNER, 2013).

The GLORYS12V1 product has obviuosly higher space and time resolution than the observational dataset, enabling a more comprehensive investigation on the characterization and evolution of the circulation, and the associated mesoscale activity in the western tropical Atlantic. In order to obtain this more detailed perspective of the processes involving the NBUC-NBC system and the SEUC origin, the numerical results were previouly and properly validated, as presented ahead in this thesis.

2.3 Analytical Techniques

2.3.1 Objective analysis

Traditional optimal interpolation was used to obtain both horizontal maps and vertical sections of the temperature, salinity, density, and velocity fields from the cruise data on regular grids. For the vertical sections, the regular grid presents 5 km of horizontal resolution and 10 m of vertical resolution. We followed Silveira et al. (2004) by employing an anisotropic gaussian correlation function in the interpolation scheme. The correlation pairs from the data were fit to a theoretical form of the correlation function, which expression is given by

$$C(x,z) = (1-\epsilon^2)\, e^{-\left(\frac{x^2}{L_x^2}+\frac{z^2}{L_z^2}\right)}, \tag{2.1}$$

where ϵ^2 is the sample error variance, (L_x, L_z) are the horizontal and vertical correlation lengths. These parameters typically varied from 15-20 km horizontally, and 15-25 m vertically.

For the horizontal maps, the regular grid was chosen to be 0.1° of resolution in both zonal and meridional directions. To minimize interpolation errors in the maps, the interpolated areas were reduced to polygons surrounding the oceanographic cruises' ship routes, and the physical properties were subsequently interpolated using a horizontally isotropic correlation

function as a weight function in the scheme, following Silveira, Brown e Flierl (2000):

$$C(r) = (1 - \epsilon^2)\, e^{-\frac{r^2}{L_x^2}}, \tag{2.2}$$

where $r = \sqrt{x^2 + y^2}$ is the search radius, and L is the isotropic correlation length of 1.5°.

The stream fuction and horizontally nondivergent velocity mapping was carried out in two steps, very similarly to the procedure proposed by Carter e Robinson (1987). The first step, the zonal and the meridional velocities were interpolated to grids using the objective analysis scheme above. As a second step, the poison solver proposed by Li, Chao e McWilliams (2006) was employed to map both the stream function and the velocity potential satisfying the proper boundary conditions at the western boundaries.

2.3.2 Spectral analysis

In order to evaluate the circulation variability in the time scale at the western tropical Atlantic, the currents' transport time series were analyzed using spectral analysis as the Welch's periodogram method was applied. The power spectrum density (PSD) was estimated implementing the following steps for each analyzed time serie:

1. Removal the mean and trend from the time serie;
2. Zero-padding of the time serie;
3. Application of a highpass sixth order Butterworth filter;

- Cut-off frequency of 0.0025 cpd (400-days period);

4. Welch's periodogram method application.

- Kaiser-Bessel window of 2048-day-wide ($\alpha = 2$);
- Overlap of 50% (1024 days).

The 95% confidence bounds were also calculated and included in the spectral analysis, allowing the identification of significant peaks of the PSD. The significant peaks are the ones in which the lower confidence bound is above the upper confidence bound at the vicinities of the peak. The previously mentioned procedures were based on the spectral analysis approaches described by Welch (1967), Emery e Thomson (2014).

2.3.3 Eddy detection and tracking method

For the past 30 years, many methods were developed to detect and track mesoscale and submesoscale structures from altimetric sea surface maps and velocity field. These algorithms were based on: (i) physical characteristics, using threshold values for specified property;

(ii) flow geometry, which considers the shape or curvature of streamlines; and (iii) hybrid parameters, involving both physical and geometrical properties. For physical-characteristics based methods, some authors used relative vorticity values, wavelet analysis of vorticity fields and the Okubo-Weiss parameter (OW) (MCWILLIAMS, 1990; DOGLIOLI et al., 2007). The OW parameter quantifies the relative importance of the rotation with respect to deformation using the horizontal velocity field (OKUBO, 1970; WEISS, 1991). The parameter is calculated with the following equation:

$$OW = \left(\underbrace{\frac{\partial u}{\partial x} - \frac{\partial v}{\partial y}}_{\sigma_n}\right)^2 + \left(\underbrace{\frac{\partial v}{\partial x} + \frac{\partial u}{\partial y}}_{\sigma_s}\right)^2 + \left(\underbrace{\frac{\partial v}{\partial x} - \frac{\partial u}{\partial y}}_{\zeta}\right)^2$$

$$\boxed{OW = \sigma_n^2 + \sigma_s^2 + \zeta^2} \tag{2.3}$$

where σ_n is the shearing deformation rate, σ_s is the straining deformation rate and ζ is the vertical component of the vorticity. Negative OW values are expected inside the vortex, however the use of the parameter may induce false positive eddy detections (CHAIGNEAU; GIZOLME; GRADOS, 2008). The geometrical approach considers the closed or spiral instantaneous streamlines from horizontal velocity or sea level anomaly fields (SADARJOEN; POST, 2000; NENCIOLI et al., 2010). Although the method is indeed more accurate to identify mesoscale structures, it's more computationally expensive. Some authors, for hybrid methods, used OW parameter to identify potential eddy centers and then applied algorithms for closed-streamline detections (VIIKMAE; TORSVIK, 2013; YI et al., 2014). A study conduced by Mkhinini et al. (2014) applied the local normalized angular momentum parameter (LNAM), which accounts for the angular momentum normalized on a local area centered on each grid point. The parameter is equals to $+1$ (-1) for the center of cyclone (anticyclone) eddies and don't depend on the vortex intesity.

For the present work, it was used an hybrid method developed by Le Vu, Stegner e Arsouze (2018), the Angular Momentum Eddy Detection and tracking Algorithm (AMEDA). The AMEDA is a method based on the computation of physical properties, such as LNAM and local Okubo-Weiss (LOW) parameters, which allows the detection of eddy centers despite its intensity. It also takes into consideration the geometrical features of the streamlines, computing closed streamline contours with maximum radial velocity for the eddy boundaries. Beside the eddy detection, the algorithm tracks eddy structures and also identifies merging and splitting events. For the eddy tracking, AMEDA uses the local nearest neighbor (LNN) assingment and it uses the concept of shared streamline contours for the eddy-eddy interactions. The characteristic contour is defined as the closed streamline of maximum mean azimuthal velocity. Some of the variables, among the parameters provided by the algorithm, analyzed in the present study were: (i) the eddy type (anticyclonic, cyclonic); (ii) the mean azimuthal

velocity for the characteristic contour; (iii) the equivalent radius of a circle of same surface as the characteristic contour; (iv) the surface area of the characteristic contour; (v) (v) kinetic energy; (vi) Rossby number; (vii) eddy positions and tracks; (viii) formation points; and (iv) interactions (splitting/merging) points. The AMEDA method was applied on numerical outputs of GLORYS12V1 at the 222m depth, considered the core of the SEUC from the observational characterization here presented. The first baroclinic Rossby radius of deformation used by the algorithm is a 1° x 1° gridded 2D-field built from Chelton et al. (2006).

3

OBSERVATIONAL CHARACTERIZATION

3.1 Western Boundary Circulation

For the development of the present work, efforts were made to identify and to assemble *in situ* measurements with the purpose of characterizing, as much as possible, the South Equatorial Undercurrent (SEUC) and the associated circulation components in space and time using observational data. To better visualize the horizontal distribution of the velocity field at the study region, streamfunction maps were plotted at the γ_n = 26.7 kg m^{-3} isopycnal surface average depth, which corresponds to the core of the SEUC as previously observed by other authors such as Bourles, Gouriou e Chuchla (1999), Goes, Silveira e Wainer (2005) (Figure 7). For practical reasons, the isopycnal units were omitted hereafter when discussing the neutral density. The NBUC flows strong northward along the Brazilian continental margin and transforms into the NBC as the coast changes direction more abruptly at approximately 5°S. After continental margin veering, the NBC flows northwestward with the increment of the cSEC at surface. A subsurface-intensified, anticylonic eddy - the Potiguar Eddy (PE) according to Krelling et al. (2020) - is detectable in the REVIZEE and ONE oceanographic cruises at this latitude, north of Cape Calcanhar.

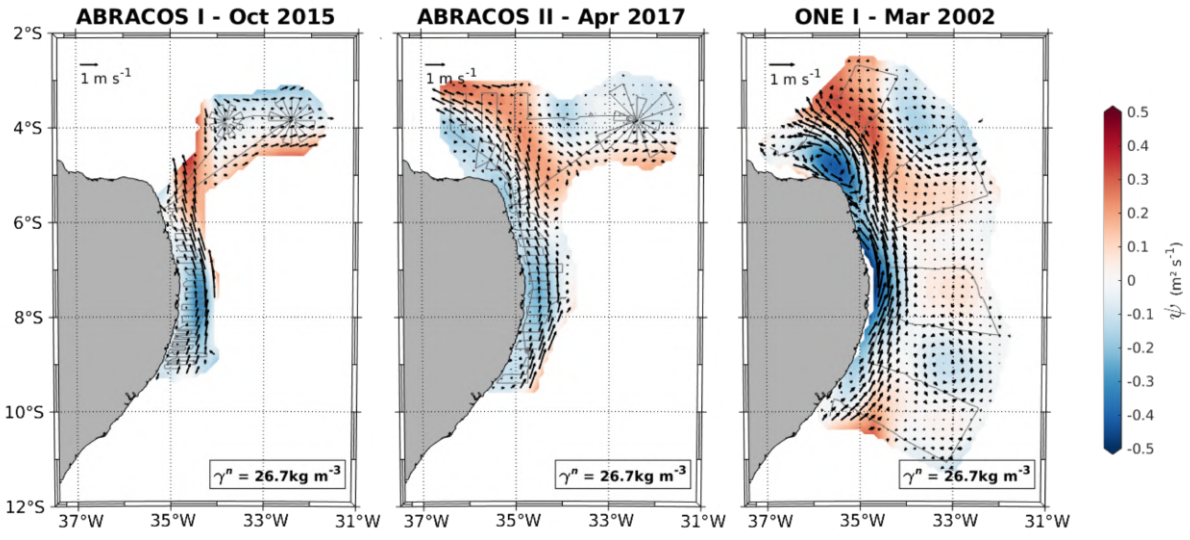

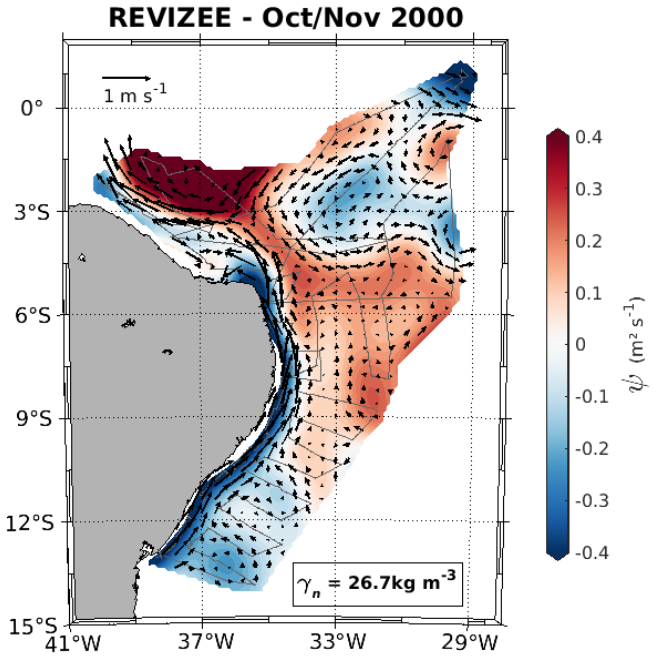

Figure 7 – Maps of velocity (black arrows) and streamfunction (colors) fields at the $\gamma_n = 26.7$ isopycnal surface for the ABRACOS I, ABRACOS II, ONE I, and REVIZEE cruises. The ship trajectory is highlighted in light gray.

Between 3.5°S and 5.5°S the SEUC flows eastward presenting a clear meandering pattern at the longitudinal band of 34.5°W and 29°W for the four cruises presented in Figure 7. The SEUC is fed by a recirculation at the northern portion of the current, as appeared in all analyzed horizontal velocity/streamfunction distributions. Despite the ABRACOS I campaign in October 2015, which is restricted to a more eastward portion of the SEUC compared to the others, there also appears to have a connection between the NBUC and the SEUC west of 34.5°W. The NBUC retroflection is presented in varying latitudes of: (i) 5.5°S for ABRACOS II cruise in April 2017; (ii) 3.5°S for ONE cruise in March 2002; and (iii) 4.5°S for REVIZEE cruise in October/November 2000, although aparently in a more subtly fashion in the scenario depicted in REVIZEE. Silva et al. (2021) using observational SADCP data for two different cruises suggest the existence of a seasonallity of the NBUC-SEUC connection, with no NBUC retroflection during fall. However, the observations here described confirm the presence of the NBUC retroflection during spring and fall seasons. It must also be noticed from the maps in Figure 7 that there are different mesoscale structures at the western boundary tropical Atlantic, characterizing it as an eddy-enriched region. The ONE campaign in March 2002 shows evidences of an anticyclone eddy centered in 9°S, and even more visually pronounced vortical features are depicted at the REVIZEE campaign map, since it covers a larger area. Eddies appear between 5°S and the equator and anticyclones seem to interact with the SEUC at its northern obrder, where the already mentioned recirculations feed the current.

In order to identify and capture the vertical structure of the currents, we selected 20 sections i. e. SADCP transects in the study area from the 13 campaigns listed in Table 2 of distinct periods of the year. The Figures 8 to 13 represent different aspects of the circulation in the western tropical Atlantic with the sections and its respective maps. These

little maps illustrate the horizontal position of the section and the velocities at 220m, depth which corresponds to the main core of the SEUC. In the figures, the neutral density was calculated and interpolated from temperature and salinity of ARMOR3D fields for each section analyzed and the isopycnals of $\gamma_n = 24.5$, $\gamma_n = 26.7$, $\gamma_n = 27.1$ and $\gamma_n = 27.2$ were highlighted. It is cleat that the sections' positions and their inclinations relative to the shelf break orientation varied within the dataset here analyzed. Hence, in order to better visually identify the currents focus of this study, the cross-section velocities were rotated in a way that the NBUC-NBC system have always positive velocities (in red) and the SEUC have negative velocities (in blue).

Figure 8 shows the North Brazil Undercurrent (NBUC) south of 5°S flowing northward extending down to 800m depth along the coast with velocities reaching over 1.0 m s^{-1} at its core, located around 200m depth. At the upper layers between 80m and 200m depth, the NBUC is broader, ranging from the coast to approximately 33.5°W and accounting for about 160km wide. Down 200m depth, the NBUC is narrower with less than 100km wide.

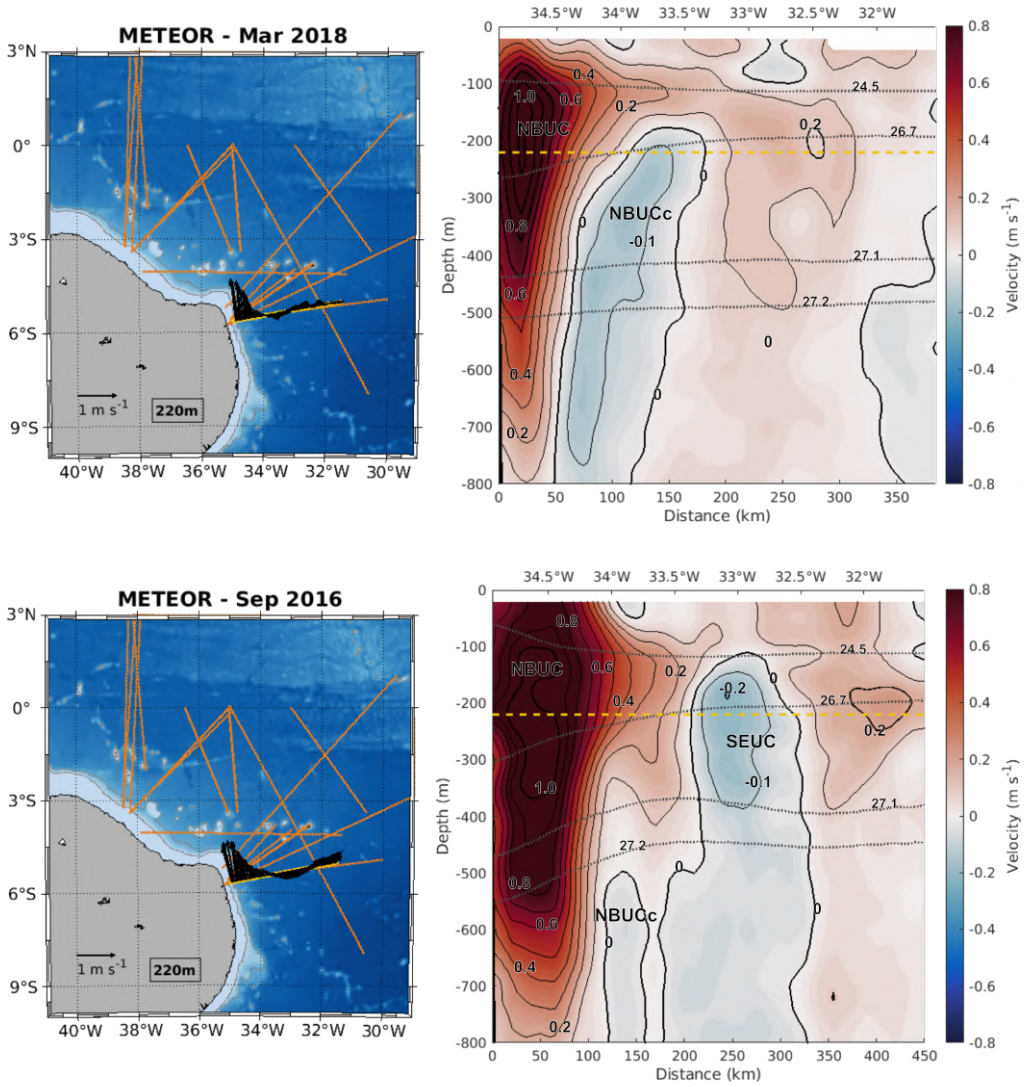

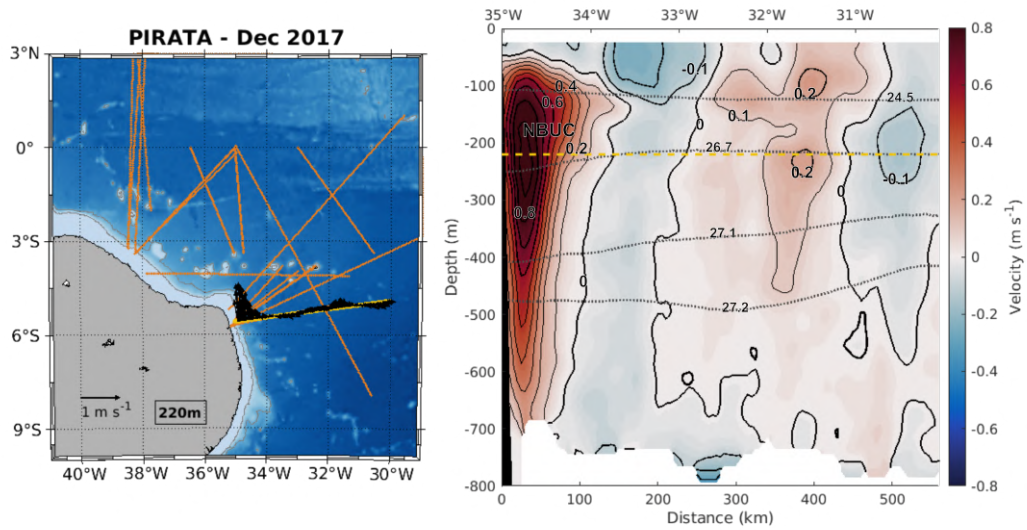

Figure 8 – Cross-section velocities of the METEOR (Mar 2018), METEOR (Sep 2016) and PIRATA (Dec 2017) transects, and their respective maps indicating the section position (yellow line) and velocity (black arrows) at 220m depth. In these sections, gray dashed lines represent isopycnals and yellow dashed lines highlight the 220m depth.

A southward counterflow is present just eastward of the NBUC in Figure 8. The North Brazil Undercurrent counterflow (NBUCc) has also been observed by other authors, such as Silveira, Miranda e Brown (1994), Stramma, Fischer e Reppin (1995), Schott et al. (2002), Silva et al. (2009). As previously mentioned, the NBUCc source remains unclear and might be originated from the deflection of the central and/or equatorial branches of the South Equatorial Current (cSEC/eSEC) at deeper levels, or from the NBUC recirculation, or even fed by part of the SEUC turning southward. At this latitude, the SEUC is not very clearly defined. At the METEOR section in September 2016, it is possible to identify the current with velocities down to 0.2 m s^{-1}, core centered around 220m depth and extending from the $\gamma_n = 24.5$ to the $\gamma_n = 27.2$ isopycnals. All the sections in Figure 8 evidence what seems to be a meandering pattern of an eastward flow which can be verified as alternating patches of positive and negative velocities at the 220m depth east of 33.5°W, corresponding to the SEUC.

Figure 9 also displays sections at 5°S, at which the NBUC flows northward along the coast down to around 650m depth (the lower depth limit of the SADCP measurements). It is wider in subsurface, narrower in deeper levels, and with a maximum velocity of 0.9 m s^{-1} (Figure 9). In the PIRATA section in May 2001, the NBUCc identified as a pronounced southward flow east of the NBUC, with core velocity of 0.3 m s^{-1} at 300m depth. At this same section, the SEUC appears east of 32°W and north of 4.5°S with the core centered around the $\gamma_n = 26.7$ isopycnal. A northwestward flow with the core centered at around the $\gamma_n = 26.7$ isopycnal is observed between the NBUCc and the SEUC in the PIRATA section. This northwestward flow could be related to a deeper part of the cSEC or could even be associated with a subsurface mesoscale feature, since the 4-5°S band has been considered a

source of energy to radiate tropical instability waves (TIW) due the baroclinic instability of the cSEC vertical shear (SCHUCKMANN; BRANDT; EDEN, 2008). For the other sections

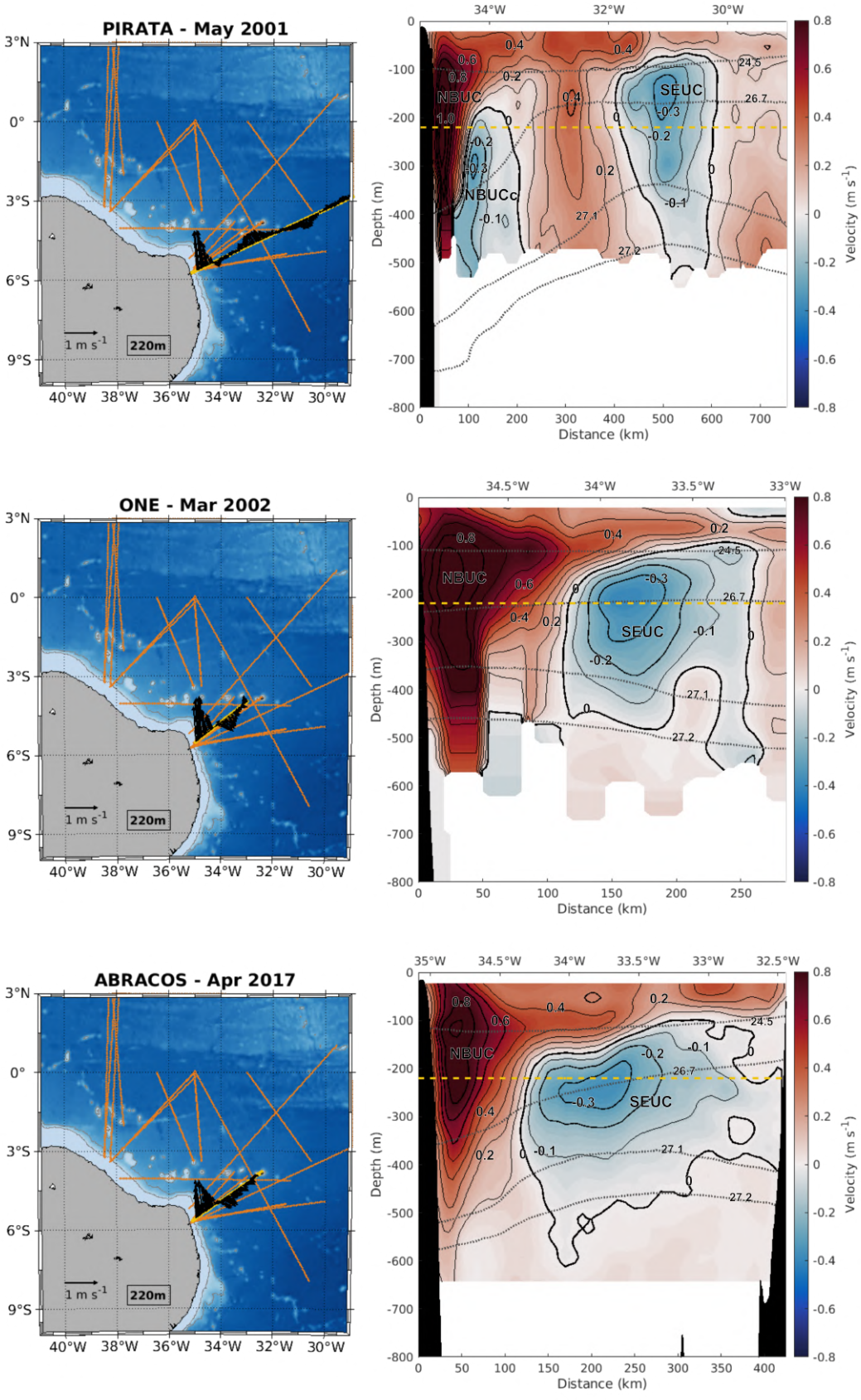

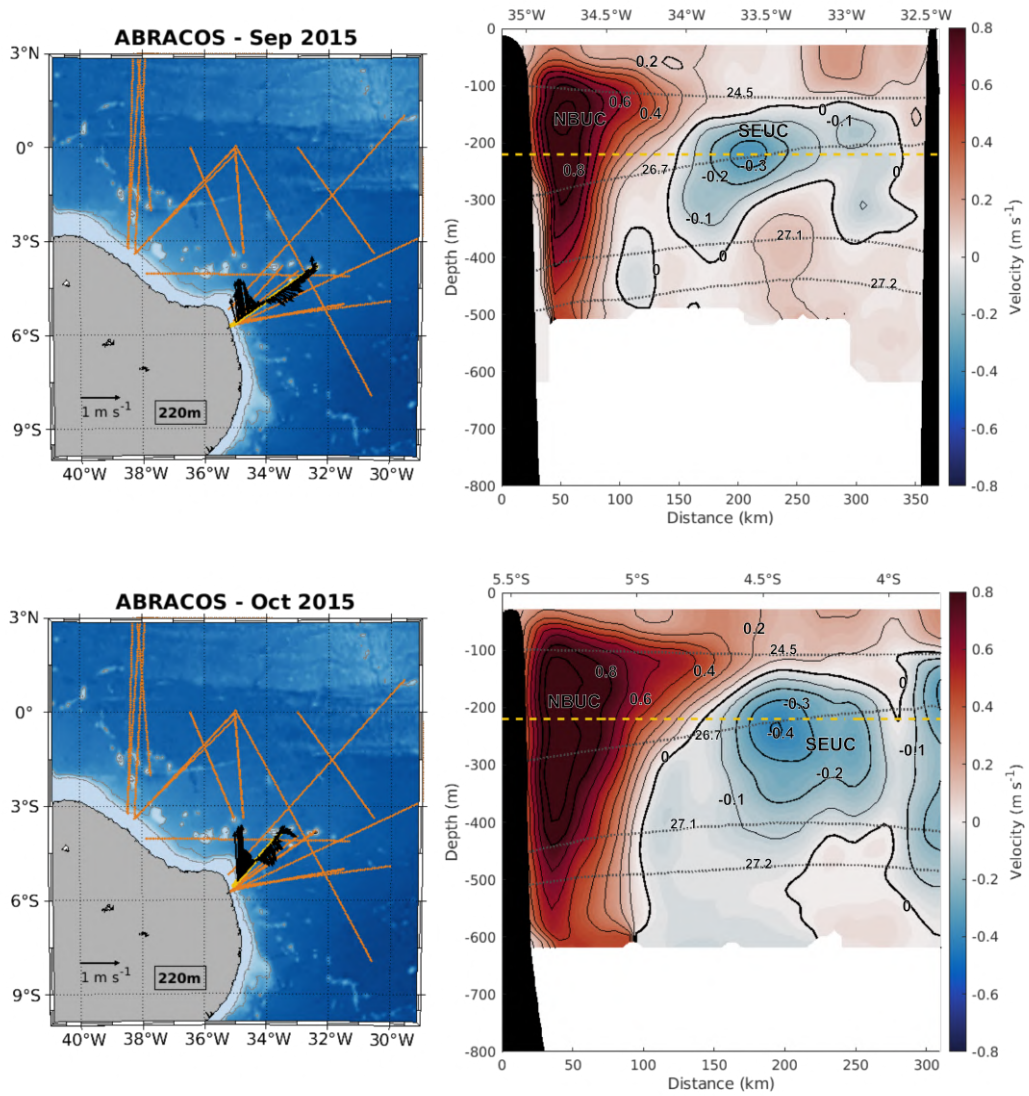

Figure 9 – Cross-section velocities of the PIRATA (May 2001), ONE (Mar 2002), ABRACOS II (Apr 2017), ABRACOS I (Sep 2015) and ABRACOS I (Oct 2015) transects, and their respective maps indicating the section position (yellow line) and velocity (black arrows) at 220m depth. In these sections, gray dashed lines represent isopycnals and yellow dashed lines highlight the 220m depth.

north of 5°S presented in Figure 9, the SEUC appears east of 34.5°W ranging from 100m and approximately 600m depth, mostly comprised between $\gamma_n = 24.5$ and $\gamma_n = 27.2$ isopycnals. At this coordinates, the current core is centered close to 220m depth and to $\gamma_n = 26.7$ isopycnal with southeastward velocities up to 0.4 m s^{-1}.

Figure 10 groups the sections which where off the Brazilian continental margin entirely or partially.. In those, between 32°W and 34°W, the SEUC is observed at 3-5.5°S within the limits of $\gamma_n = 24.5$ and $\gamma_n = 27.2$ with a core at $\gamma_n = 26.7$, which corresponds to the 220m depth. At these coordinates, the current reaches maximum depths of 500 m and velocities up to 0.6 m s^{-1} with eastward and northeastward directions. Specifically in the REVIZEE section (November 2000), the SEUC is captured closer to the Brazilian coast between 35°W

and 32.5°W, presenting southeastward velocities.

Considering the three sections altogether in Figure 10, the SEUC meandering pattern is made evident, as also depicted in Figure 8. For both PIRATA sections, an intense eastward flow is captured north of 2°S and above 230m depth, identified as the Equatorial Undercurrent (EUC), reaching velocities of 0.7 m s^{-1}. In the PIRATA section of August 2010, the strong westward cSEC is visible iat surface, also reaching subsurface levels. In the PIRATA section from November 2017, the cSEC appeared more confined to the surface. Finally, the NBUC-NBC system appears at 4°S and 34-37°W reaching mainly the 450m depth, with a core of 0.4 m s^{-1} in surface and a subsurface core of 0.9 m s^{-1} at 160m depth.

The ensemble of sections presented in Figure 11 shows a perspective of the spatial distribution of the SEUC from the east to the west at Cape Calcanhar. The NBUC-NBC system appears very strong at the REVIZEE section as the current seems to cross the section almost perpendicularly, which is not observed in the PIRATA sections. At the REVIZEE section and also at the PIRATA section in October 2015, the current core is observed around 140m depth, closer to the surface when compared to sections south of 5°S illustrated before. The latter section still presents a small core at 25m, corresponding to the arrival of the westward cSEC at the Brazilian coast. At these coordinates, where the continental margin changes direction more abruptly, the NBUC is transitioning to become the NBC. For the PIRATA section in November 2015, high velocities at 250m depth could be related to the PE formation, as observed at the last section in Figure 10 at this same depth. On the north portion of the sections in Figure 11, the EUC is present at 40-220m depth with core velocities slightly above 0.8 m s^{-1} and centered close to the $\gamma_n = 24.5$ isopycnal. The SEUC appears at 2.5-4.2°S between the $\gamma_n = 24.5$ and the $\gamma_n = 27.2$ isopycnals, reaching velocities of 0.4 m s^{-1} around 34.5°W and 35°W. At the western portion - about 36°W - captured by the PIRATA section in November 2015, a slim core of 0.3 m s^{-1} is observed at 2.3°S, 250m depth, also centered in $\gamma_n = 26.7$. This core might be related to the SEUC formation at 36°W. It is noticeable that the SEUC and the EUC are gradually approximating, as we observe these eastward currents from east to west along the Brazilian coast. In fact, previous authors using current measurements, such as Schott, Fischer e Stramma (1998), Bourles, Gouriou e Chuchla (1999), stated that it was not possible to clearly distinguish the SEUC from the EUC at 35°W.

West of 36°W and north of 3.5°S, the NBC is more clearly defined as a double core current flowing westward following the shelfbreak topography (Figures 12 and 13). The surface core is visible at the upper levels above the 100m depth with core velocities ranging from 0.6 m s^{-1} to 1.2 m s^{-1}. The subsurface core is observed around 180m depth, always restricted between the $\gamma_n = 24.5$ and the $\gamma_n = 26.7$ isopycnals and reaching velocities of 1.2 m s^{-1}.

Although PIRATA section in August 2004 does not capture the full NBC depth range, the other sections show the current confined at the upper 440m of the water column, which is shallower when compared with the NBUC south of 5°S. The EUC presented in Figure 12 is

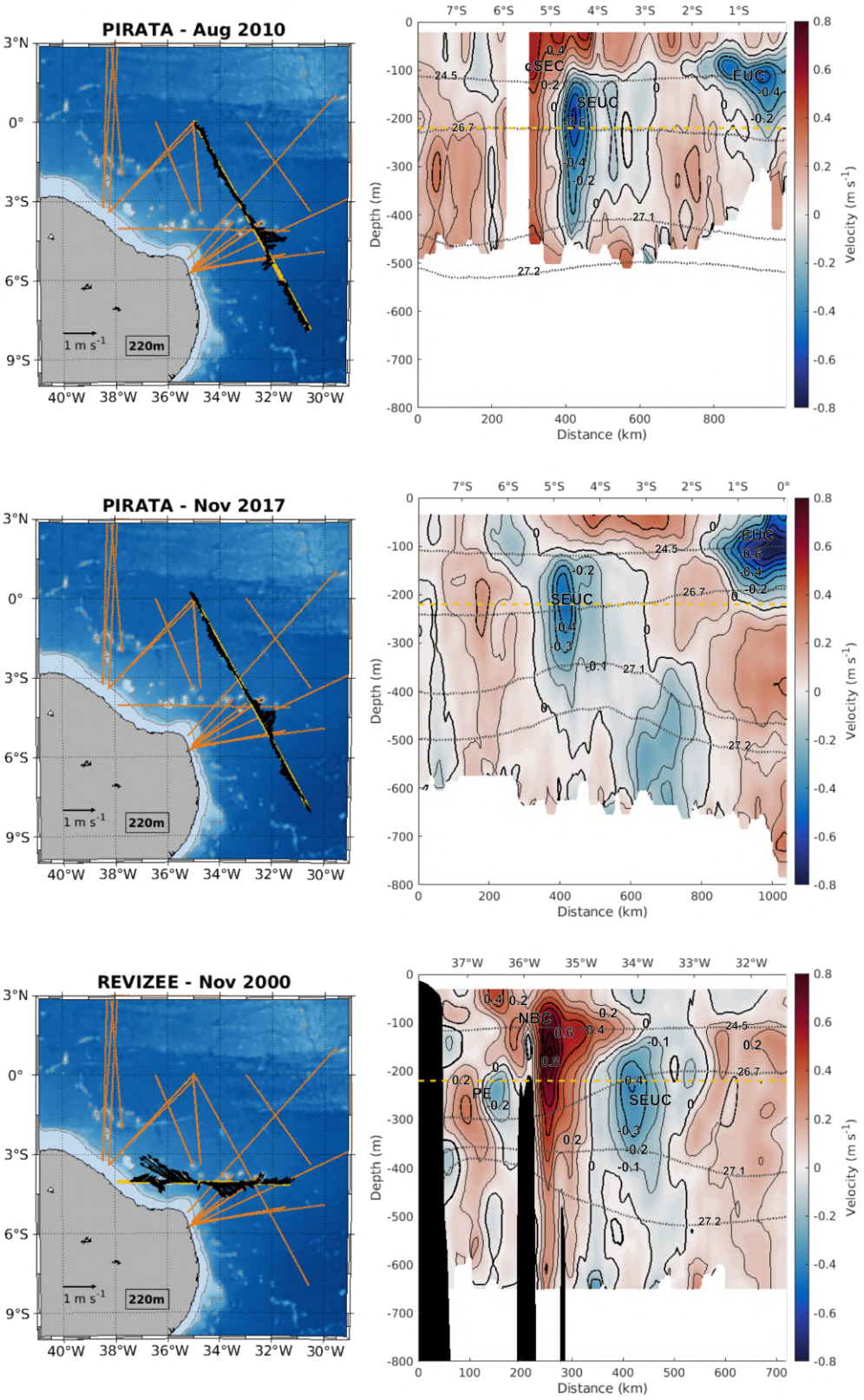

Figure 10 – Cross-section velocities of the PIRATA (Aug 2010), PIRATA (Nov 2017) and REVIZEE (Nov 2000) transects, and their respective maps indicating the section position (yellow line) and velocity (black arrows) at 220m depth. In these sections, gray dashed lines represent isopycnals and yellow dashed lines highlight the 220m depth.

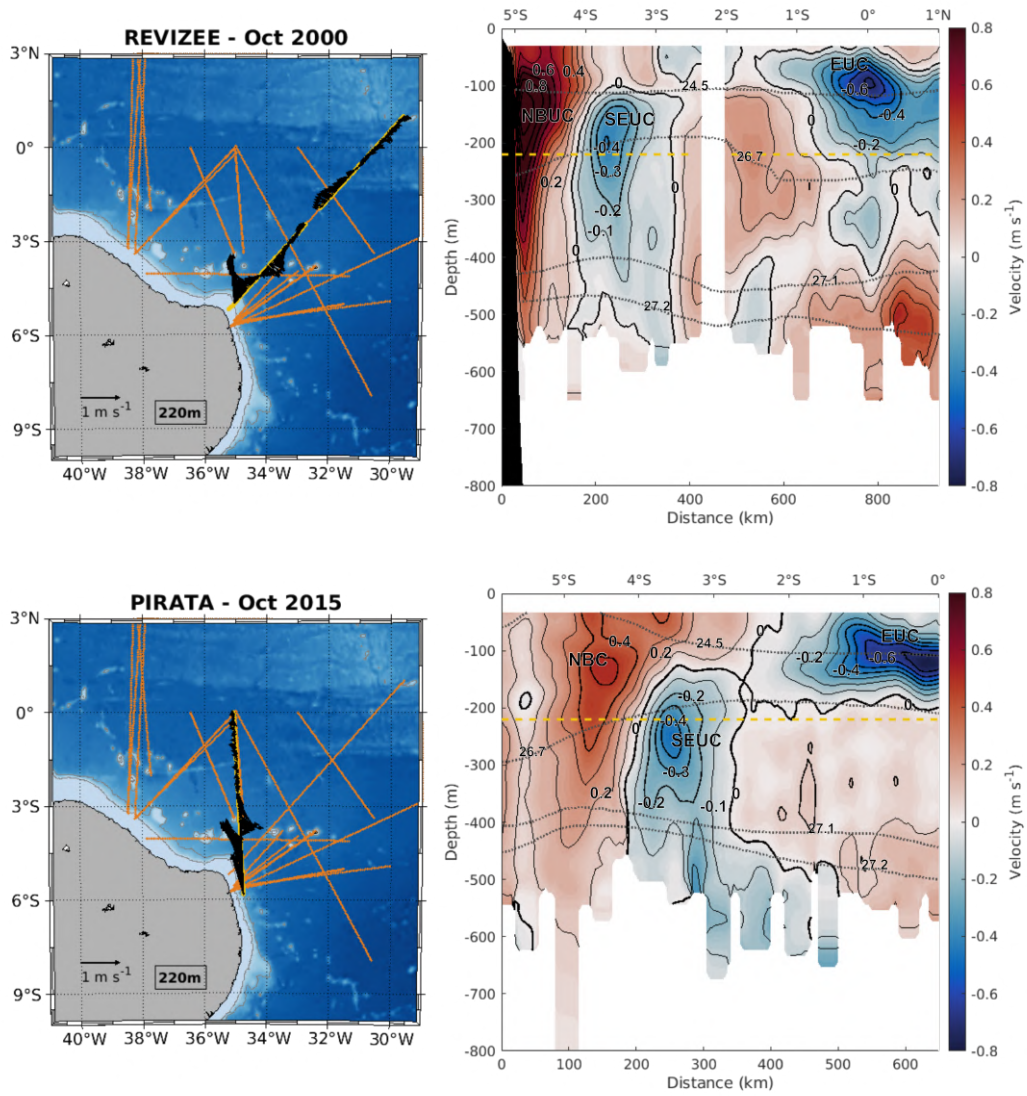

located around 36°W and north of 1.5°S with velocities up to 0.9 m s^{-1} and a core centered at approximately $\gamma_n = 24.5$ isopycnal. At the proximities of the $\gamma_n = 26.7$ isopycnal, around 1.5°S, a core of velocities ranging from 0.1 m s^{-1} to 0.5 m s^{-1} for the illustrated sections seems to be detached from the EUC at deeper levels. The flow at this point has a southeastward direction and could be related to a SEUC signal at 36.8°W. In Figure 13, around 38°W, the EUC still presents strong eastward flow with velocities up to 0.7 m s^{-1}, with the core once again centered around the $\gamma_n = 24.5$ isopycnal, above the 240m depth. At 1.5-2°S, the small core detached from the EUC observed at 36.8°W persists for the 38°W longitude, with velocities of 0.1-0.4 m s^{-1} slightly above the $\gamma_n = 26.7$ isopycnal.

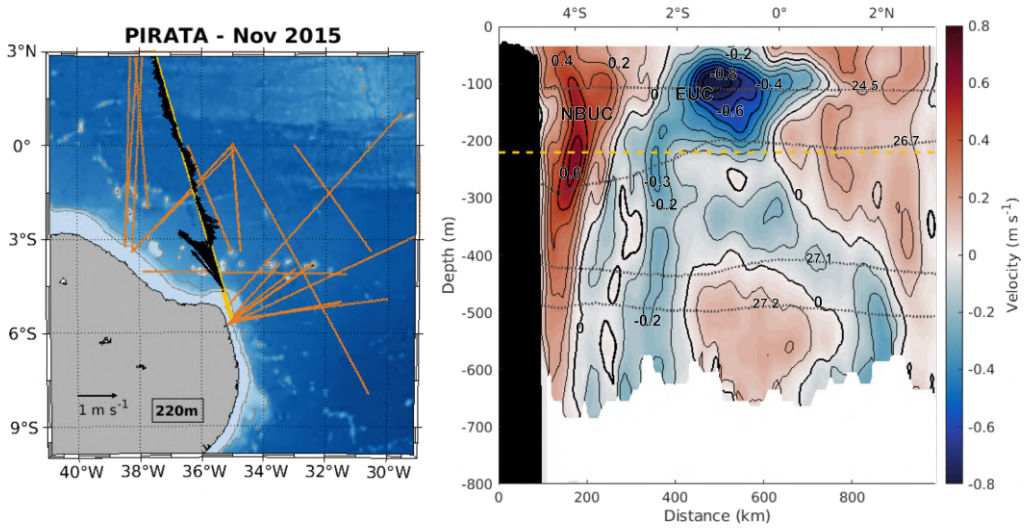

Figure 11 – Cross-section velocities of the REVIZEE (Oct 2000), PIRATA (Oct 2015) and PIRATA (Oct 2015) transects and their respective maps indicating the section position (yellow line) and velocities (black arrows) at 220m depth. In these sections, gray dashed lines represent isopycnals and yellow dashed lines highlight the 220m depth.

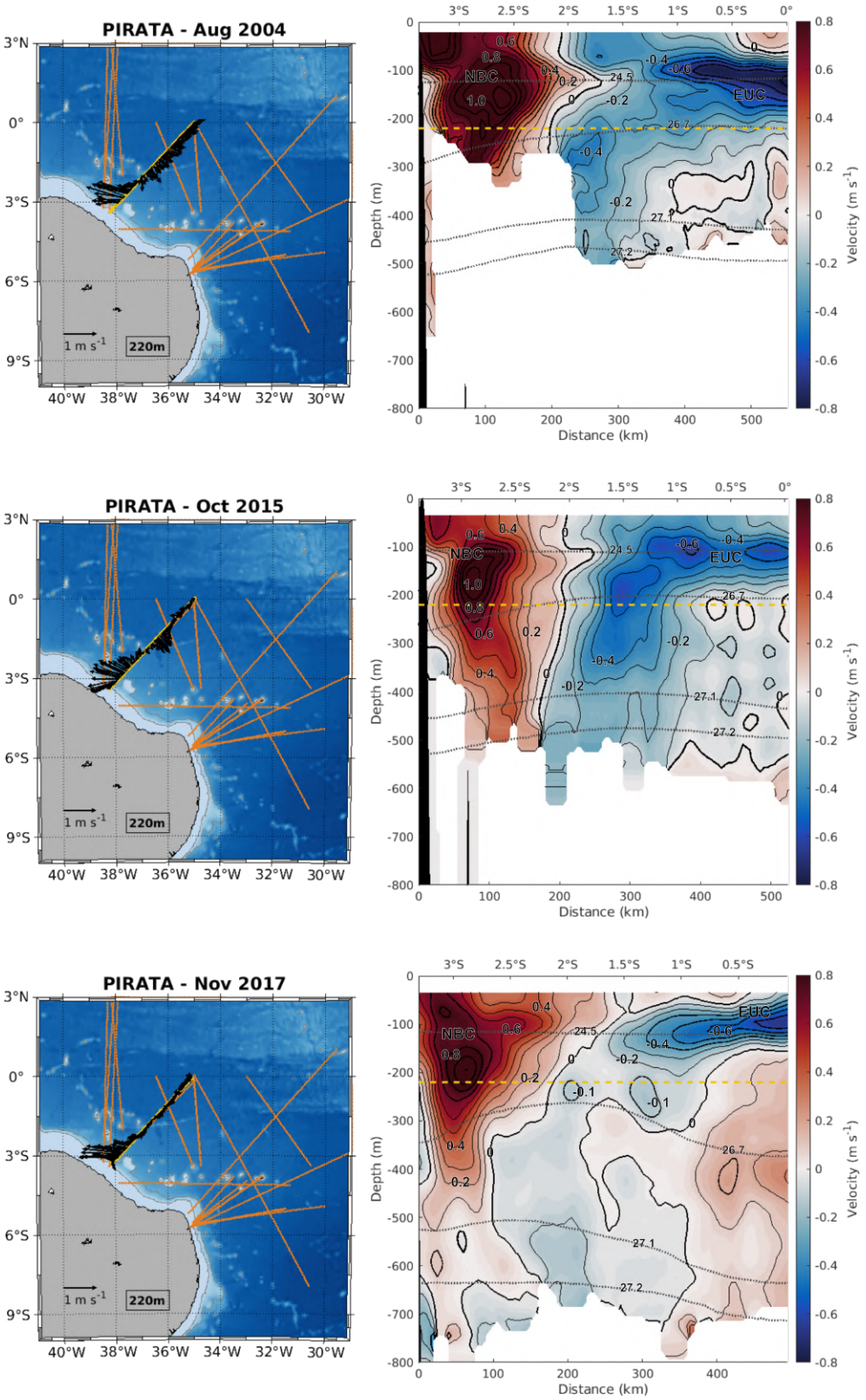

Figure 12 – Cross-section velocity of sections PIRATA (Aug 2004), PIRATA (Oct 2015) and PIRATA (Nov 2017), and its respective maps indicating the section position (yellow line) and velocity (black arrows) at 220m depth. In sections, gray dashed lines represent isopycnals and yellow dashed lines highlight the 220m depth.

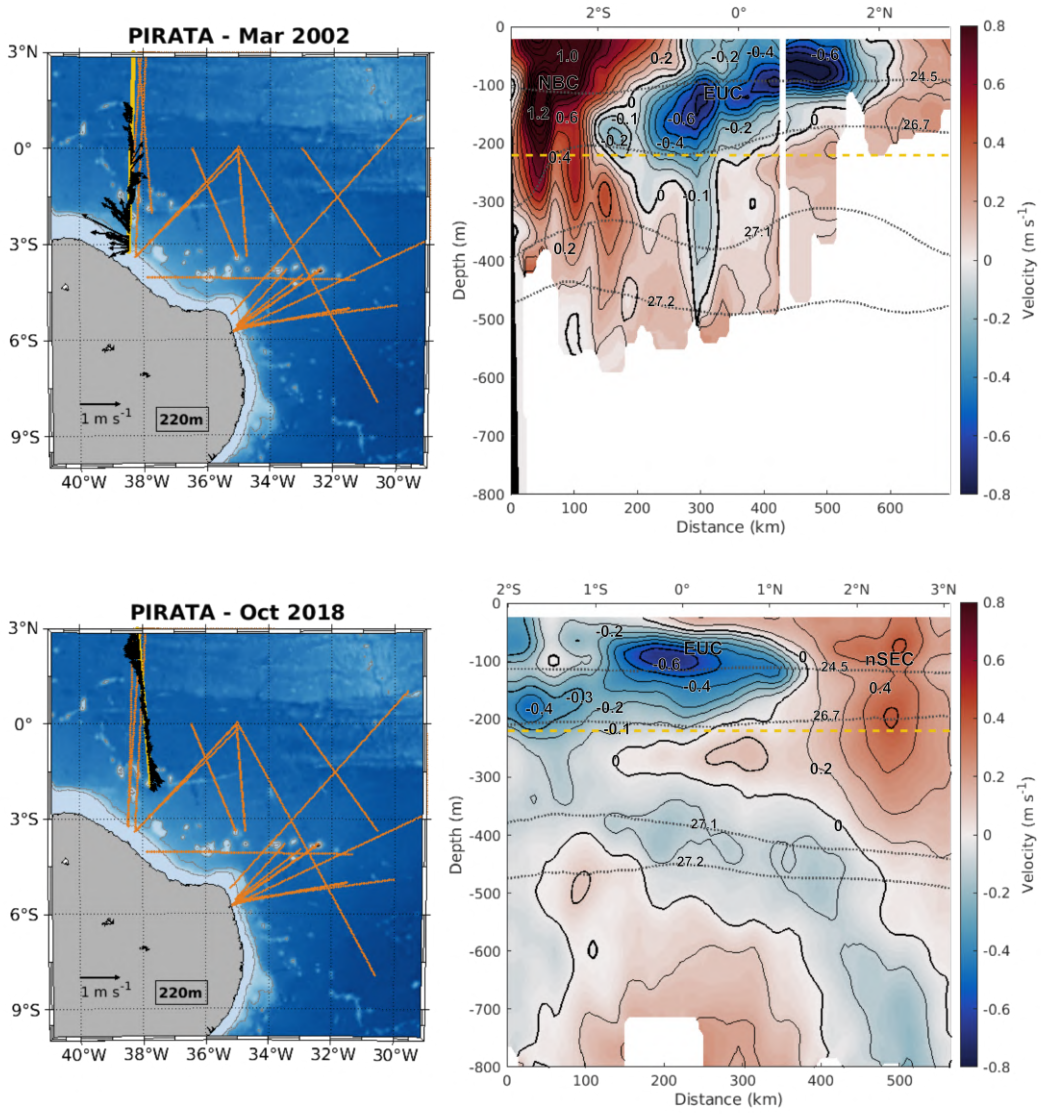
PIRATA - Mar 2002
3°N
0°
3°S
6°S
9°S
40°W 38°W 36°W 34°W 32°W 30°W
1 m s-1
220m
2°S 0° 2°N
NBC
EUC
24.5
26.7
27.1
27.2
Depth (m)
Distance (km)
Velocity (m s-1)
PIRATA - Oct 2018
2°S 1°S 0° 1°N 2°N 3°N
EUC
nSEC
24.5
26.7
27.1
27.2
Depth (m)
Distance (km)
Velocity (m s-1)

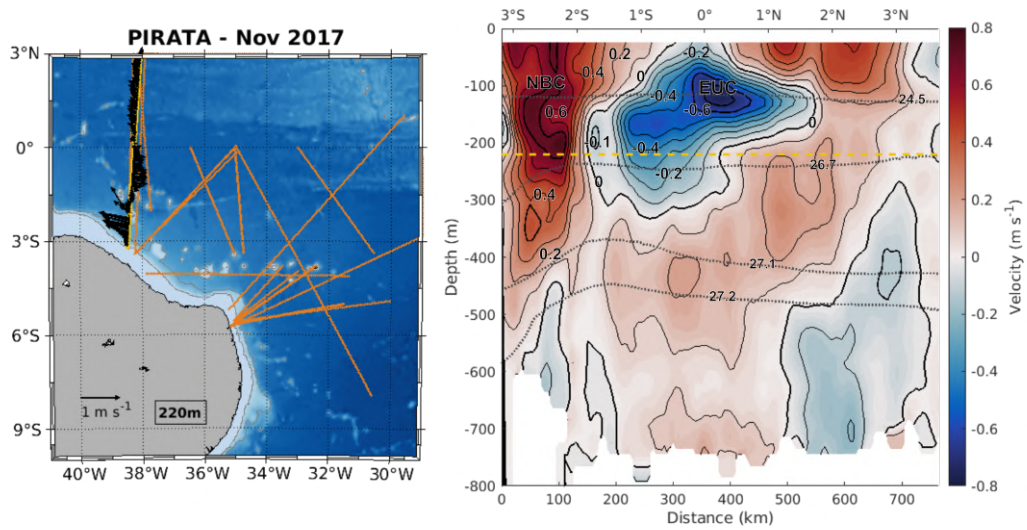

Figure 13 – Cross-section velocity of sections PIRATA (Mar 2002), PIRATA (Oct 2018) and PIRATA (Nov 2017), and its respective maps indicating the section position (yellow line) and velocity (black arrows) at 220m depth. In sections, gray dashed lines represent isopycnals and yellow dashed lines highlight the 220m depth.

According to Cochrane, Kelly e Olling (1979), near 38°W part of the NBC retroflects eastward at subthermocline levels, which suggest that the small core could be related to a NBC retroflection to feed the eastward SEUC, or could even be related to mesoscale structures as anticyclones flowing westward at the region.

The NBUC, NBC and SEUC transports, captured by the sections above adressed, were calculated between the $\gamma_n = 24.5$ and $\gamma_n = 27.2$ isopycnals and are presented in Table 3. The values marked with (a) are the calculated transports for circulation structures associated with the SEUC meandering pattern observed around 5°S, and the values marked with (b) are the structures associated with the SEUC formation, where the small core was recurrently observed between 1.5°S and 2°S slightly above the $\gamma_n = 26.7$ isopycnal. Considering the calculated water volume fluxes observed in the sections, the mean NBUC/NBC system transport is 21.4 Sv, with a standard deviation of 6.7 Sv. For the calculations we did not consider the current transport observed during METEOR cruise in September 2016, once it presented an unusually high value compared to the other sections, probably resulting from an observed NBUC is observed much wider and deeper than whats has been observed at that position. Results indicated the NBUC-NBC system has a mean transport of 19.9 Sv, with a standard deviation of 3.1 Sv. Taking into consideration the SEUC and its associated meandering and formation transports, the mean SEUC transport is 6.4 Sv, with a 3.6 Sv standard deviation. For the westernmost sections (Figures 12 and 13), the SEUC transports show a wide range of values with a minimum of 0.4 Sv and maximum of 12.0 Sv. Thus, discarding the associated transports i.e. meandering and formation transports, the SEUC presents a mean flow of 8.1 Sv and a 2.0 Sv standard deviation. As expected, no clear seasonal signal is evident from cruise measurements, neither

Sections	Transports (10^6 m^3 s^{-1} = 1 Sv)		
	NBUC/NBC	SEUC	
METEOR - Mar 2018	24.3	-	Figure 8
METEOR - Sep 2016	44.8	8.0	
PIRATA - Dec 2017	18.1	*4.4/2.2* [a]	
PIRATA - May 2001	18.2	8.2	Figure 9
ONE - Mar 2002	22.7	6.5	
ABRACOS II - Apr 2017	18.8	9.6	
ABRACOS I - Sep 2015	17.1	3.8	
ABRACOS I - Oct 2015	26.1	8.5	
PIRATA - Aug 2010	-	9.9	Figure 10
PIRATA - Nov 2017	-	11.7	
REVIZEE - Nov 2000	14.1	7.8	
REVIZEE - Oct 2000	20.4	8.7	Figure 11
PIRATA - Oct 2015	18.3	6.8	
PIRATA - Nov 2015	16.6	*7.6* [b]	
PIRATA - Aug 2004	19.4	*6.8* [b]	Figure 12
PIRATA - Oct 2015	23.1	*12.0* [b]	
PIRATA - Nov 2017	19.4	*3.1* [b]	
PIRATA - Mar 2002	22.5	*0.6* [b]	Figure 13
PIRATA - Oct 2018	-	*5.3* [b]	
PIRATA - Nov 2017	19.8	*0.4* [b]	

[a] Transports which might be associated with the SEUC meandering.
[b] Transports which might be associated with the SEUC formation.

Table 3 – NBUC, NBC and SEUC transports captured at the sections in Figures 8-13 limited by the γ_n = 24.5-27.2 isopycnals.

for the SEUC flux nor for the NBUC-NBC system. In addition, it must be considered the fact that the current flows might not be entirely perpendicular to the sections and that the calculated transports listed in Table 3 represent the circulation in different parts of the western tropical Atlantic region. However, the robust observational data acquired with SADCP during various oceanographic cruises provide an insightful perception of the vertical distribution of the horizontal velocities, despite the clear necessity of higher space and time resolution observations for further inferences.

3.2 Regional Analysis of Water Masses

The water mass structure in the upper ocean (from surface to $\approx$ 1300m depth) of the tropical South Atlantic consists of: the Tropical Water (TW), the South Atlantic Central Water (SACW) and the Antarctic Intermediate Water (AAIW). The TW is formed by mixed-layer water presenting the highest values of temperature and salinity. A salinity maximum water is formed from the subduction of salty waters in the limb between subtropical and equatorial gyres overlayed by lower salinity water due to precipitation in the tropical region (REID, 1989; STRAMMA; SCHOTT, 1999). The SACW is located at the pycnoclinic level and presents the largest range of temperature and salinity values. The AAIW is characterized by a salinity minimum and high concentrations of dissolved oxygen. After a compilation of density and depth ranges, Silveira, Napolitano e Farias (2020) provided the water masses interfaces for the Tropical Atlantic shown reproduced here in Table 4.

Water mass	**Potential density range (kg m^{-3})**	**Depth range (m)**
Tropical Water	$<$ 24.50 (σ_0)	0 - 150
South Atlantic Central Water	24.50 (σ_0) - 26.90 (σ_0)	150 - 500
Antarctic Intermediate Water	26.90 (σ_0)- 32.15 (σ_1)	500 - 1000

Table 4 – Ranges of referenced density and depths of each water mass at the western tropical Atlantic upper ocean. Adapted from Silveira, Napolitano e Farias (2020)

The northward flow which results from the pycnoclinic sSEC bifurcation at about 20°S, in addition with the surface component from the sSEC bifurcation at 15°S, leads to the NBUC formation. This current transports 30 Sv of TW, SACW and AAIW equatorward in the upper 1200m with a salinity maximum around 150-200m (SILVEIRA; MIRANDA; BROWN, 1994; SCHOTT et al., 2005; SILVEIRA; NAPOLITANO; FARIAS, 2020). Along the Brazilian continental margin from Cape Calcanhar to low latitudes of the northern hemisphere, the NBUC-NBC system carries these water masses with a northwestward flow marked by different retroflections at the subpycnoclinic, pycnoclinic and surface levels. Considering the horizontal and vertical velocity distributions from observational analysis of the previous section, and the

density and depth ranges presented in Table 4, the SEUC carries SACW and a portion of AAIW, since the current ranges from $\gamma_n = 24.5$ to $\gamma_n = 27.2$, from approximately 90m to 520 m - with the values converted to neutral density.

The water masses in the tropical western boundary circulation of the pycnoclinic/-subpycnoclinic layer (around $\sigma_0 = 24.5$-26.8 kg m^{-3}) can also be identified by its temperature, salinity and oxygen at a certain isopycnal limit. Many studies, such as Wilson, Johns e Molinari (1994), Arhan et al. (1998), Schott, Fischer e Stramma (1998), Bourles et al. (1999), Goes, Silveira e Wainer (2005), have distinguished the water masses for this region in basically three types: (i) the South Atlantic Waters (SAW), rich in oxygen and with relatively low salinity; (ii) the North Atlantic Waters (NAW), with high oxygen and salinity values; and (iii) the Eastern Atlantic Waters (EAW), poor in oxygen and with similar salinity magnitude to the SAW. Schott, Fischer e Stramma (1998) and Bourles et al. (1999) separated the water sources at the tropical Atlantic western boundary region for the $\sigma_0 = 26.7$ kg m^{-3} and the $\sigma_0 = 26.25$ kg m^{-3} isopycnals, respectively, as described in Table 5.

Water masses	Schott, Fischer e Stramma (1998)		Bourles et al. (1999)	
	Salinity	**DO (mL L^{-1})**	**Salinity**	**DO (mL L^{-1})**
Southern waters	< 35.2	> 3.4	35.2 - 36.2	3.8 - 4.5
Northern waters	> 35.3	< 3.3	36.2 - 36.8	3.0 - 4.0
Eastern waters	< 35.3	< 3.3	35.6 - 36.5	2.4 - 3.2

Table 5 – Water sources at the tropical Atlantic western boundary region for the $\sigma_0 = 26.25$ kg m^{-3} and the $\sigma_0 = 26.7$ kg m^{-3} isopycnals from Schott, Fischer e Stramma (1998) and Bourles et al. (1999), respectively.

In the present work, it is used oxygen-salinity (O_2–S) diagrams to distinguish the water masses of different circulation components, and to identify their origin in respect to SAW and EAW (Figure 14). The inferences on the water sources (EAW and SAW) are defined based on areas analyzed in previously mentioned studies. The EAW area was fixed between 2°-3°S and 22.5°-23.5°W, using as reference the findings of Fischer et al. (2008) for a mean section at 23°W, with the SEUC flowing south of 3°S and an westward flow at picnoclinic and subpicnoclinic levels. Luko et al. (2021) showed that the sSEC reaches the Brazilian coast with bands in 14°S and 18°S to feed the NBUC at pycnoclinic and subpycnoclinic levels. Thus, the SAW area is defined between 14°-16°S and 35°-39°W. The O_2–S diagrams were generated to evidence the regional water masses origin of four areas and respective circulation components: (i) the SEUC area; (ii) the NBUC area; the NBC area; and (iv) the subpycnoclinic portion of the eSEC area. These four areas are defined following the observational results exposed in the sections and maps presented in Figures 7–8- cvh the SEUC latitudinal extent ranging from 3°S to 5°S, and the eSEC limited between 1.75-2.5°S.

In our analysis, the observational oxygen and salinity values were extracted from WOD18 and from cruises' hydrographic measurements, for two neutral isopycnal ranges: (i) $\gamma_n = 26.69$ and $\gamma_n = 26.71$ isopycnals, which comprises the SEUC core; (ii) $\gamma_n = 26.99$ and $\gamma_n = 27.01$ isopycnals, at the subpycnoclinic level, inside the SEUC isopycnal limits of $\gamma_n = 24.5$-27.2. In addition, percentiles are calculated to better quantify and understand the oxygen and salinity content distributions represented in the standard O_2–S diagram. It is used to better capture the level of an unequally distributed dataset, as percentiles are not strongly influenced by extreme values i.e. "outliers"as much as other mean-based metrics. In this work, it is established the 5th, 50th (median) and the 95th percentiles as representatives for the dissolved oxygen observations.

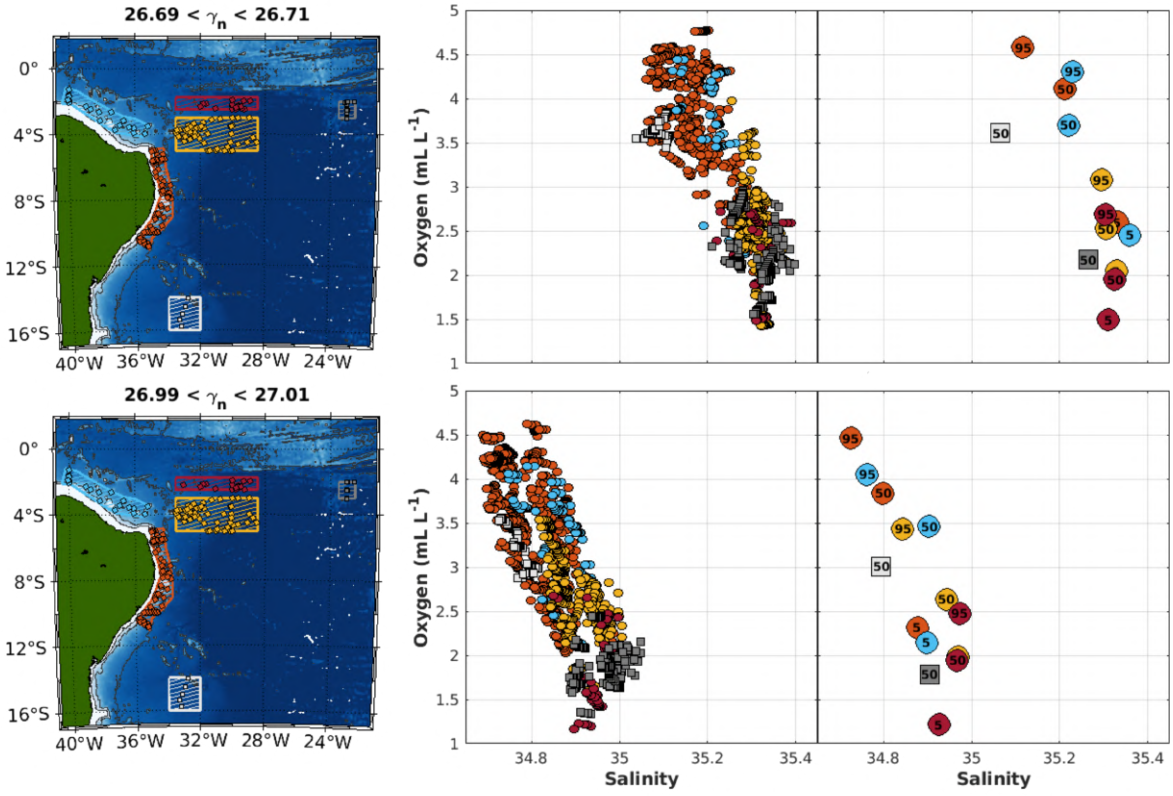

Figure 14 – Oxygen-salinity (O_2–S) diagrams for the pycnoclinic and SEUC core level ($\gamma_n \approx 26.7$) and for the subpycnoclinic level ($\gamma_n \approx 27$), from WOD18 and from the hydrographic cruise data. The EAW reference (eastern portion of the SEUC) is represented as gray squares, the SAW reference (sSEC) is as white squares, the NBUC as orange circles, the NBc as light blue circles, the eSEC as purple circles and the SEUC is illustrated as yellow circles.

In Figure 14, the SAW reference water mass (white squares) has higher dissolved oxygen content and lower salinity values both isopycnal levels, when compared to the EAW reference water mass (gray squares), which present lower oxygen concentration and higher salinity. At the SEUC core and pycnoclinic level of $\gamma_n \approx 26.7$, the SAW median dissolved oxygen is 3.6 mL L^{-1} and salinity is 35.08, and the EAW median presents values of 2.2 mL L^{-1} and 35.28, respectively. In subpycnoclinic level $\gamma_n \approx 27.0$ level, the SAW median dissolved oxygen is

3.0 mL L^{-1} and salinity is 34.79. The EAW median presents values of 1.8 mL L^{-1} and 34.91, respectively.

In general, at pycnoclinic level, the water masses from: (i) the NBUC-NBC system (orange and light blue dots) presents higher dissolved oxygen and lower salinity ($\uparrow O_2 \downarrow S$), similar to SAW values; (ii) the eSEC (purple dots) and also the SEUC itself (yellow dots) have lower oxygen concentrations and higher salinities ($\downarrow O_2 \uparrow S$), resembling the EAW. It is important to notice that the eSEC shows lower dissolved oxygen values than the SEUC water masses at this level. The 50th and 95th percentiles for the NBUC-NBC system are even higher in oxygen concentrations than the SAW reference. However, the 5th percentiles for both currents have similar characteristics to the 95th eSEC percentile and the SEUC median. In fact, the SEUC 95th percentile shows even higher oxygen concentration than the NBUC-NBC system 5th percentiles. Such results lead us to believe that the source of higher oxygen concentrations in the SEUC are carried from the NBUC to the SEUC.

The same general characteristics observed in the pycnocline are also found at subpycnoclinic level: (i) the NBUC-NBC system has $\uparrow O_2 \downarrow S$, similar to the SAW; and (ii) the eSEC and SEUC show $\downarrow O_2 \uparrow S$, resembling the EAW in a lesser extent than at the picnoclinic level. Once again, the NBUC-NBC system median and 95th percentile demonstrate higher dissolved oxygen values than the SAW reference, even comparable to concentrations observed at picnoclinic level. The system 5th percentiles are very similar to EAW showing quite low oxygen concentrations at this level. The eSEC 5th, 50th and 95th percentiles appear relatively close to the EAW characteristics, as already expected. However, the SEUC percentiles cover a wider range in terms of oxygen concentrations. The 5th percentile is indeed similar to EAW characteristics, although the 50th percentile (median) falls in between SAW and EAW references, suggesting a mixture between these water masses. The 95th percentile presents a high value for dissolved oxygen, even greater than the SAW reference and comparable to NBUC-NBC system oxygen concentrations. Again, these results point that the feeding of the SEUC by the NBUC is still more evident at the subpycnoclinic level. Bourles, Gouriou e Chuchla (1999) suggest a connection between the EUC and the SEUC, and Jochum e Malanotte-Rizzoli (2004) even consider this connection being at higher isopycnal levels. Another source for the high oxygen concentrations at subpycnoclinic level could be a deeper portion of the EUC, originated further north from oxygen-rich waters recirculating to the NBC retroflection.

4

ANALYSIS OF NUMERICAL MODELING OUPUTS

4.1 Model Validation

The observational results brought important and elucidating information to the SEUC origin and formation process. However, to better investigate its spatial and time variability, the use of numerical modeling outputs is made necessary. Before proceeding to the analysis with the GLORYS12V1 outputs, the model must be properly validated for the region. With that in mind, Figure 15 shows streamfunction and velocity field snapshots constructed with the product outputs. The numerical outputs are compared to the oceanographic cruises analyzed in the previous chapter: ABRACOS I, ABRACOS II, ONE and REVIZEE (Figure 7). The numerical velocity fields were interpolated as the observational maps, using objective analysis technique with the same influence radii and cutoff values as the data. Therefore, the GLORYS12V1 streamfunction and nondivergent velocities are subject to the same smoothing as the observations. The selected depth of 222m was chosen as representative of the SEUC core average depth, observed in the cruises' data, minimizing possible errors related to vertical interpolations.

Some differences between the *in situ* measurements and the numerical product results of the streamfunction and velocity fields could be related to the fact that the observations are quasi-synoptic, whereas the simulations are synoptic. Besides, the interpolation method could also be a source of divergences at the polygon edges of the observational maps. Despite small dissimilarities, the horizontal streamfunction and velocity distributions in the model results are in good agreement with the *in situ* measurements.The retroflection pattern, the extended retroflection lobe, the Potiguar Eddy, and other features on the cruise-model individual comparisons are alike. However, quantitative arguments are necessary to validate the GLORYS12V1 outputs, as described next.

To examine the model performance in reproducing the vertical structure of the current systems, we compare GLORYS12V1 outputs and observations to selected set of sections obtained from oceanographic cruises (Figures 9-11) where SEUC was clearly registered by

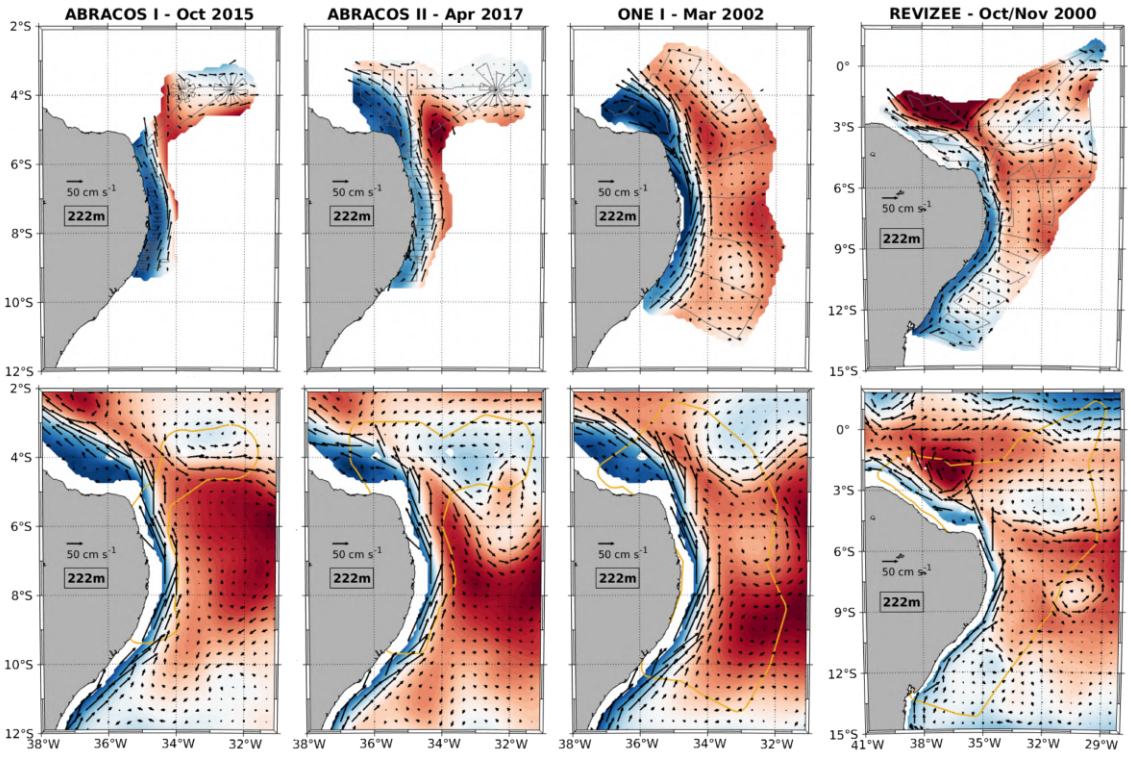

Figure 15 – Horizontal velocity and streamfunctionn distributions for the ABRACOS I, ABRACOS II, ONE and REVIZEE oceanographic campaigns (upper panels), and the respective maps for the GLORYS12V1 model outputs (lower panels). The yellow polygon represents the region of interpolation used in the observational maps.

means of radar charts. The considered core information to form the radar plots included: (i) latitude of ocurrence of the feature; (ii) longitude; (iii) depth; (iv) neutral density (γ_n); (v) along-section velocity component; (vi) cross-section velocity component; and (vii) maximum total velocity or velocity magnitude. Figure 16 shows the cross-section velocity component obtained from *in situ* mesurements and from the model results. The associated radar charts, also known as spiderweb charts, in Figure 16 compare observed and numerical characteristics of the SEUC core, allowing a visualization of the similarities between them. The proximity between the modeled and observational values at the radar vertices indicate the quality of numerical output in reproducing the data.

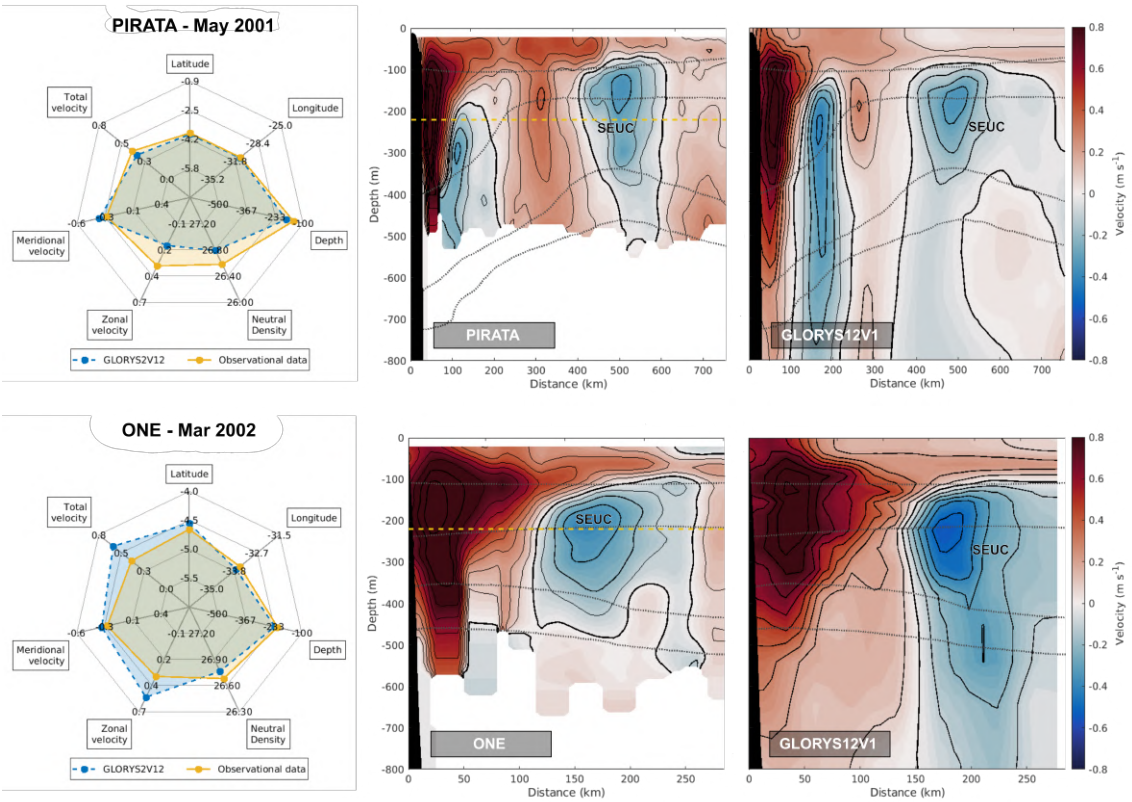
PIRATA - May 2001
Latitude
Longitude
Depth
Neutral Density
Zonal velocity
Meridional velocity
Total velocity
GLORYS2V12
Observational data
SEUC
PIRATA
GLORYS12V1
Depth (m)
Distance (km)
Velocity (m s-1)
ONE - Mar 2002
ONE

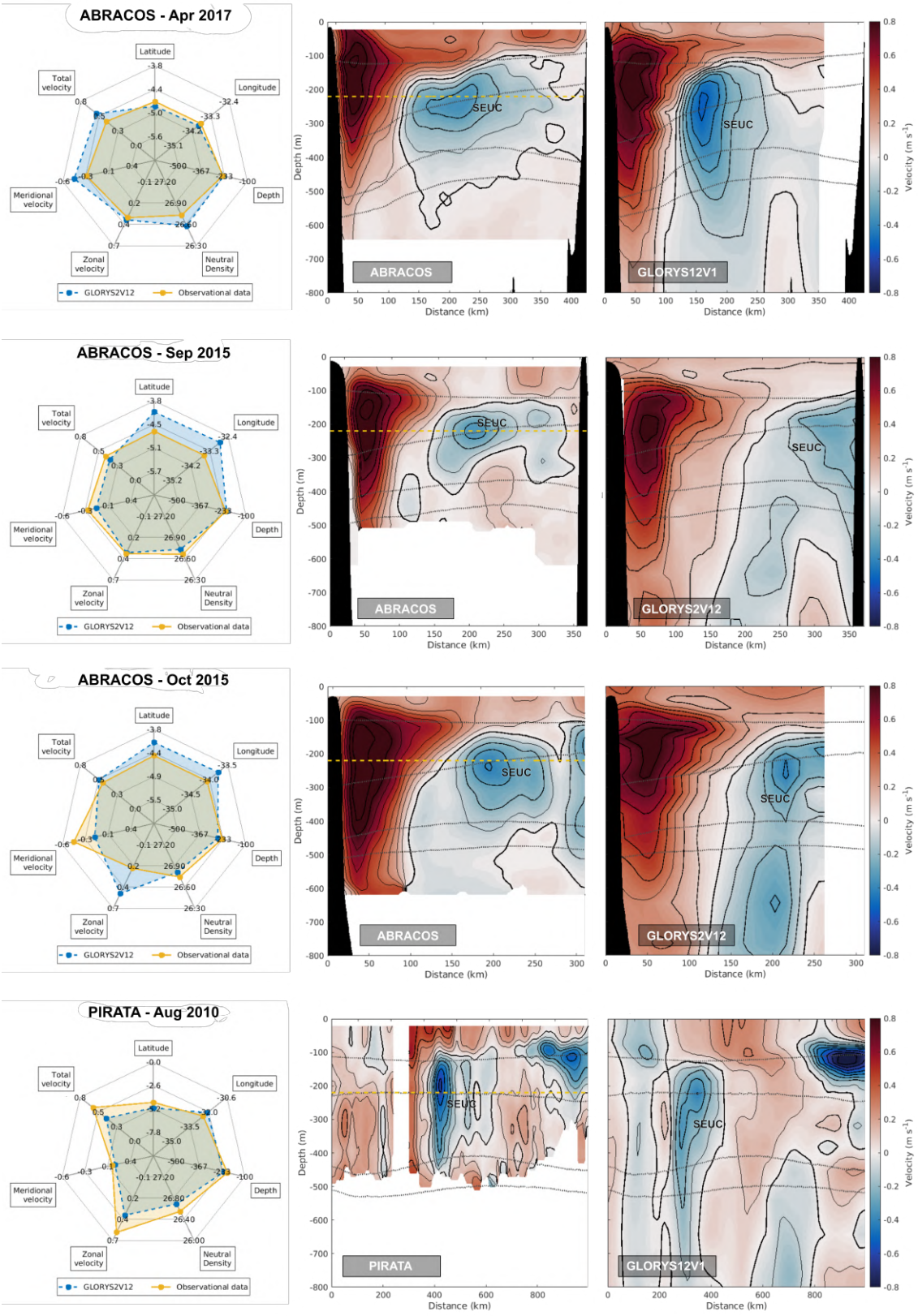
ABRACOS - Apr 2017
Latitude
Longitude
Depth
Neutral Density
Zonal velocity
Meridional velocity
Total velocity
GLORYS2V12
Observational data
SEUC
ABRACOS
GLORYS12V1
Depth (m)
Distance (km)
Velocity (m s-1)
ABRACOS - Sep 2015
GLORYS2V12
ABRACOS - Oct 2015
PIRATA - Aug 2010
PIRATA

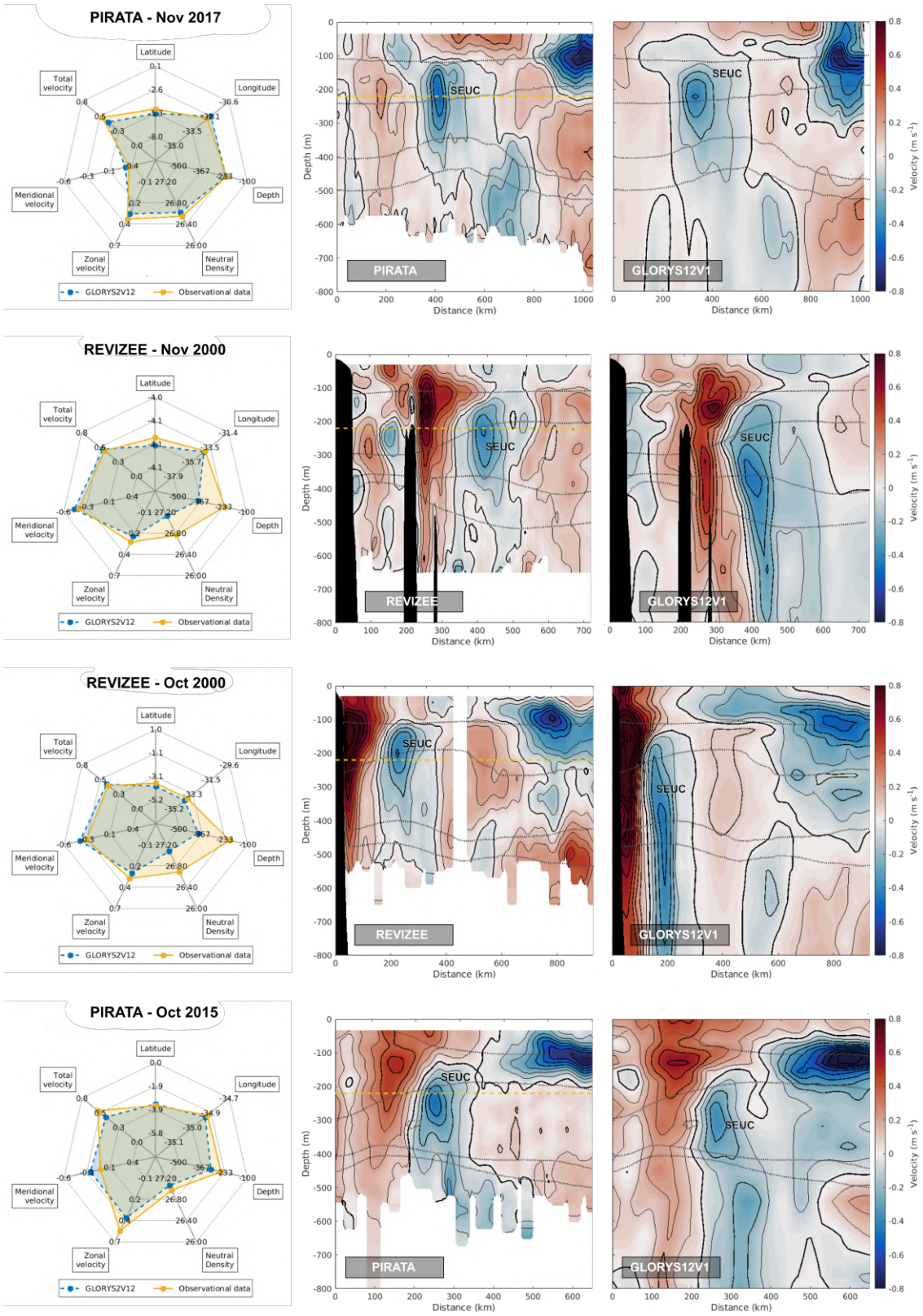

Figure 16 – Radar chart with SEUC core informations (latitude, longitude, depth, neutral density, along-section velocity component, cross-section velocity component, and total velocity or velocity intensity), and comparison between cross-section velocity distributions obtained from *in situ* measurements and from modelling results (GLORYS12V1).

In general, the results are strongly correlated. Visually, the cross-section velocity fields for both observational and modeled sets are very consistent, and the SEUC core variables show again a high resemblance between measurements and numerical outputs. The main differences occur in: (i) the ABRACOS September 2015 section in terms of horizontal core position, with a still small difference of 0.7° in longitude; (ii) both REVIZEE sections relative to the depth position and density layer, as the SEUC core is in deeper and more dense layers, reaching 183m and $\gamma_n = 0.39$ differences, respectively. Despite the ABRACOS I October 2015 section indication of 0.3 m s^{-1} differences in zonal and meridional velocities, in terms of total velocity, variations did not exceed 0.2 m s^{-1}. These subtle differences could be related to variations in the meandering and mesoscale activity between model and measurements. In fact, Figure 16 evidence that there's a high compatibility between observational data and GLORYS12V1 results with a very good circulation agreement not only in horizontal perspective but once again in the vertical direction.

We also employed an even more rigorous statistical way to compare model and data: the use of the Taylor diagram, as seen in Figure 17. The Taylor diagram is a concisely statistical form of evaluating the correspondence between simulated and observed fields through their correlation, their root-mean-square (RMS) difference, and the ratio of their variances (TAYLOR, 2001). In this figure, we synthetize the results of the same sections showed in the radar charts (Figures 9-11). We just recall the reader that these are the sections revealing a SEUC clearly distinguishable. In the Taylor diagram, the correlation values between the series are disposed

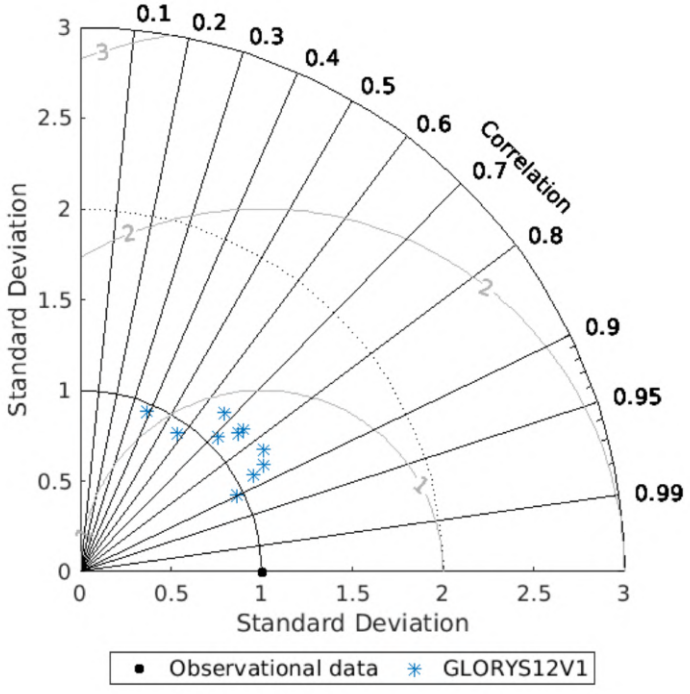

Figure 17 – Taylor diagram of cross-section velocity sections from observational data and model results (GLORYS12V1).

over the circumference, the root-mean-square differences are represented in light gray lines and the variances ratios are illustrated radially regarding the circumference. Basically, the ideal outcome would be model results (asterisk points in Figure 17), as close as possible to the

observations (black point in same the Figure), which means the model has a high correlation, a similar standard deviation with the *in situ* data, and a low RMS value.

The Taylor diagram confirms the overall good performance of the GLORYS12V1 product concerning SEUC analyzed sections. The model shows no low correlation values and the points with moderate correlations - between 0.3 and 0.7 - represent the PIRATA August 2010, the PIRATA November 2017 and the REVIZEE November 2000 sections. The PIRATA sections have lower correlations of 0.39 and 0.58 respectively, which are probably due to dissimilarities at the southern portion of the SEUC and the currents' intensities. The REVIZEE section has a correlation value of 0.67, which might be consequence of differences in the SEUC core depth and the deeper layers at the eastern part of the section. Despite these moderate correlations, the radar charts and section comparisons in Figure 16 show very good resemblance between simulated and measured fields. The seven other sections analyzed show still higher correlations, with points up to 0.9, also present similar standard deviations and low RMS values. The synthesis provided by the Taylor diagram allows us to expand our investigation about SEUC dynamics in the study region by means of continuous time series of a three-dimensional fields of velocity and mass (density).

4.2 Volume Transport Balance and Time Variability

The results of the regional water mass analysis using WOD18 and the cruise measurements provided very good insights about the SEUC origin. The presence of high oxygen concentrations in the SEUC region, which is characteristic of the South Atlantic Waters (SAW), evidenced the current connection with the NBUC. Another important remark is the trace of higher dissolved oxygen concentrations in subpycnoclinic levels, indicating strong NBUC-SEUC connection also in deeper levels.

Although observations are very important for ocean scientific development, numerical modeling enables a more comprehensive analysis in time and space. Thus, with the GLORYS12V1 model properly validated, it is possible to analyze the volume transport balance and space-time currents variabilities at the Tropical Atlantic western boundary.

4.2.1 Climatological seasonal current patterns

The first step taken by us is to build a climatology using the whole time series of the GLORYS12V1 run aiming to build a mean scenario as well as characterize seasonal variations ans patterns. In order to evaluate the transport balance in the study region, and the contributions from different circulation components to the region of the SEUC origin, four sections are defined forming a rectangular area (Figures 18a-21). The sections are delimited as follows:

(i) southernmost section at 30-35.2°W, 6°S (orange, Figure 18a); (ii) westernmost section at 38.5°W, 1°-3.2°S (blue, Figure 19); (iii) northernmost section at 30-38.5°W, 1°S (green, Figure 20); and (iv) easternmost section at 30°W, 1-6°S (yellow and purple, Figure 21). For each of these sections, climatological hovmöller diagrams are constructed using velocity vectors at the same SEUC core level (222 m depth). These climatological hovmöller plots of the current velocities enable us the visualization and demarcation of the main circulation components of each section, respectively: (i) the NBUC; (ii) the NBC; (iii) the EUC; and (iv) the deeper eSEC portion and the SEUC.

The southernmost section at 30-35.2°W, 6°S (orange, Figure 18a) encompasses the NBUC confined to the Brazilian continental margin west of 33.2°W (G-H slice in Figure 18a). The climatologic current is observed narrower in March-April and wider in June-July. According to Silveira, Miranda e Brown (1994), Schott, Fischer e Stramma (1998), and in agreement with the observations presented in the previous chapter, the NBUC core depth is around 200m depth, therefore the velocity here analyzed at 222m can be considered the NBUC core signature. At 34.6°W, the core total velocity varies between 1.02 m s^{-1} in April, and 1.09 m s^{-1} in October. Notice that, since the climatologic velocity variation is very small, the seasonal differences in the overall transport are due to the differences in the zonal NBUC extension. Although the used scale in Figure 18a interferes with the visualization of other circulation components, east of the NBUC appears a southeastward flow followed by a northward flow further east. This alternating pattern is stronger and better defined from February to May, reaching velocity intensities up to 0.14 m s^{-1}. Such a circulation pattern just east of the NBUC could be related to the North Brazil Undercurrent counterflow (NBUCc), or even to the meandering pattern at the southern portion of the SEUC west of 30°W.

In Figure 19, the westernmost section (blue) is located meridionally along the longitude of 38.5°W and reveals a strong northwestward flow representative of the NBC following the Brazilian continental margin at 1-3.2°S. It also shows a weaker and more fluctuating eastward flow, indicative of the EUC between the equator and 1°S. The NBC presents maximum velocity at 2.3°S, varying from 0.6 m s^{-1} in May-June to 0.7 m s^{-1} in December-January. It is important to notice that, unlike de NBUC which flows in subsurface levels, the NBC also has a strong subsurface signature as well as an important surface core as a result of the eSEC and cSEC contributions (not shown here). The northwestward current was delimited from 1°S to 3.2°S (A-B slice in Figure 19), the latter being the landward bathymetric limit. The velocity direction shifts from northwestward to eastward at 1°S, separating the NBC from the EUC at 222 m depth. From 1°S to the equator, the EUC is formed with climatologic variability of a stronger flow from August to February with a weaker intensity from March to July. The velocity maxima occur at the equator ranging from 0.08 m s^{-1} in June to 0.26 m s^{-1} in September. The current also peaks in December and January.

At the northernmost section (green, Figure 20), the EUC appears inflowing to the

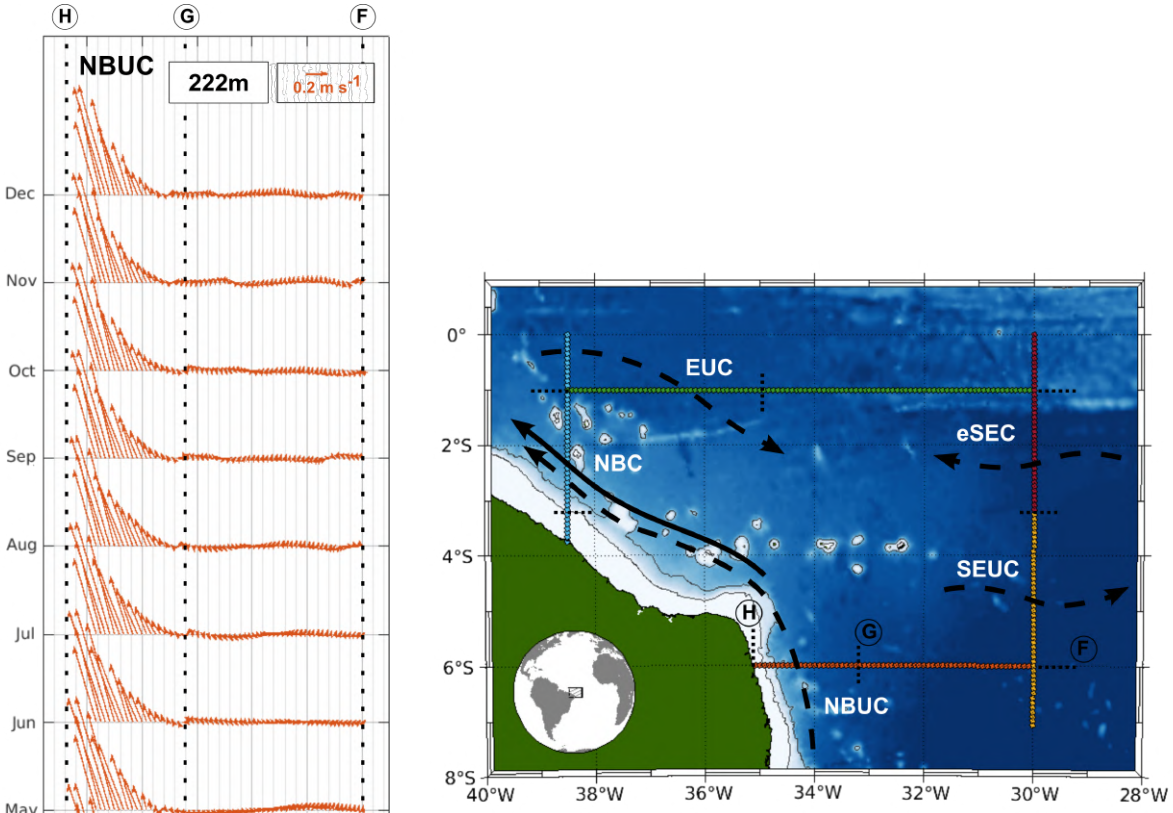

Figure 18 – Climatological seasonal hovmöller diagram of current velocity vectors at 222m depth for the southernmost section in orange. The map indicates a schematic circulation and the delimitations for the NBUC (G-H slice in the right panel) as also shown in dashed black lines in the left-side hovmöller plot.

rectangular area. The current has a predominantly southeastward direction, shifting southward in June and even southwestward in May. At 37°W, the velocity maxima are 0.19 m s^{-1} in September and 0.05 m s^{-1} in May, similar to the EUC extremes verified at 38.5ºW. However, the December and January peaks observed at the westernmost section are proportionally smaller at 37°W. The current is stronger and better defined between September and December, and demonstrates a more spatially oscillating behavior during months. Indeed, Johns et al. (1998) and Brandt et al. (2014) pointed out that the extension of the EUC depth varies to approximately 100-300 m depth, with seasonal fluctuations in its intensity and depth range: deeper in September and shallower in March. Therefore, it is possible here to capture the seasonality for the deeper period, but the seasonal signature is not very remarkable during the "shallower period". In Figure 20, the EUC was spatially defined as the flow between 35-38.5°W (B-C slice). East of 35°W, the velocities oscillate along the section and do not exhibit a net

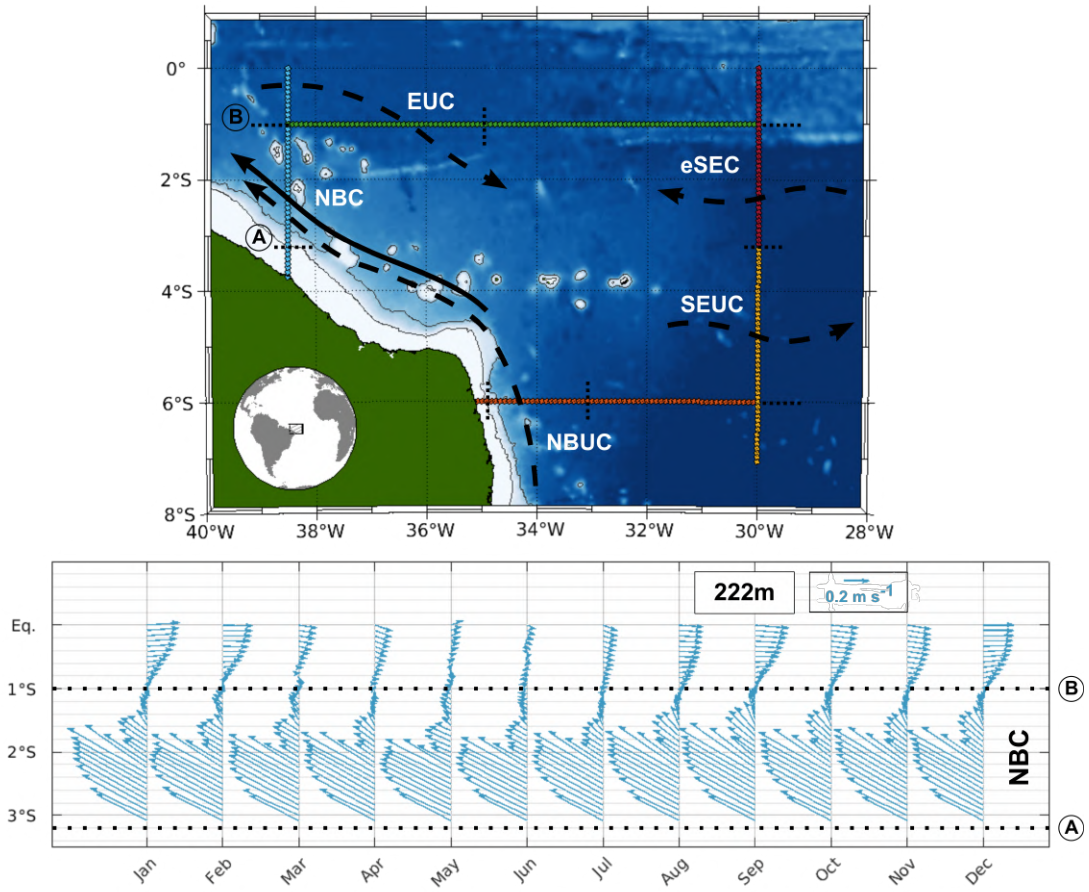

Figure 19 – Climatological seasonal hovmöller diagram of current velocity vectors at 222m depth for the westernmost section in blue. The map indicates a schematic circulation and the delimitations for the NBC (A-B slice in the upper panel) as also shown in dashed black lines in the hovmöller plot.

climatologic pattern, showing small magnitudes up to 0.06 m s^{-1}.

Some authors suggest that the SEUC is fed by recirculations entrained in the westward eSEC deeper portion and returning into the eastward current (MOLINARI, 1982; FISCHER et al., 2008). Therefore, in order to capture the eSEC apart from the SEUC, the easternmost section located at 30°W was divided in two different segments: a north portion encompassing the eSEC between the equator and 3.2°S (purple, Figure 21), and a southern portion covering the SEUC latitudinal extension at 3.2-7°S (yellow, Figure 21). The north portion reveals an eastward flow at 0°-1°S representing the EUC with similar seasonality described at the westernmost section, stronger and better defined from August to January, reaching a maximum velocity of 0.08 m s^{-1} in December near the equator. In general, the EUC velocities at 30°W are weaker than those found in 38.5°W and in 37°W, and in particular the September peak is proportionally less intense. Results show that the eSEC was delimited between 1-3.2°S (D-E slice, Figure 21), presented as a westward flow with a maximum velocity position oscillating in latitude. The meandering varies from its northernmost position in October, November and December at 2.1°S, to its southernmost position in January, February and March around 2.6°S.

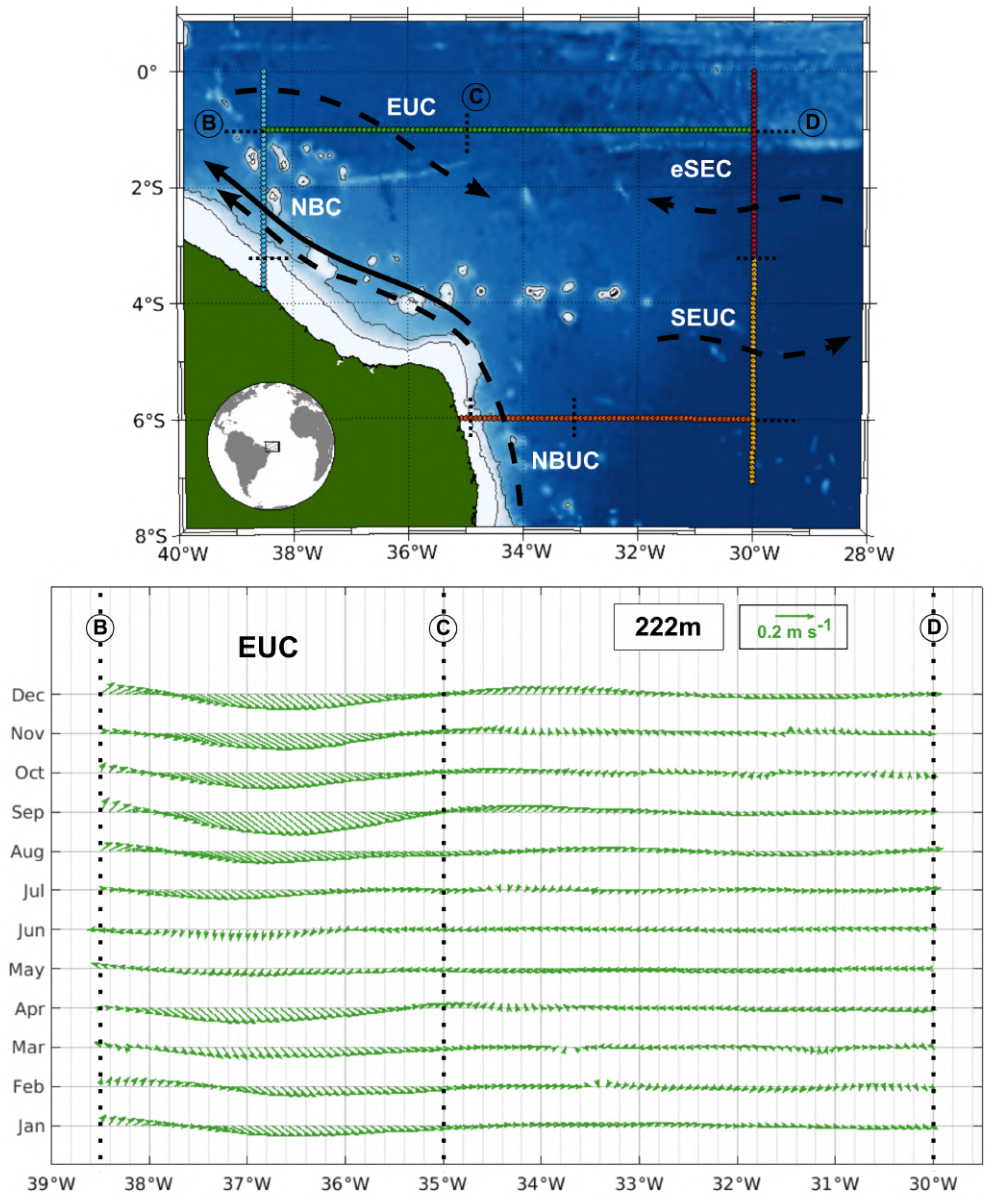

Figure 20 – Climatological seasonal hovmöller diagram of current velocity vectors at 222m depth for the northernmost section in green. The map indicates a schematic circulation and the delimitations for the EUC (B-C slice in the upper panel) as also shown in dashed black lines in the hovmöller plot.

In terms of current intensity, the velocities are higher during January-March, with a maximum of 0.14 m s^{-1}, and lower during July-September, with values around 0.05 m s^{-1}.

The SEUC is represented as the eastward flow crossing the easternmost yellow E-F slice in Figure 21, between 3.2°S and 6°S. As already evidenced from previous observational characterization, the SEUC core is located around 220 m depth. Thus, the climatological hovmöller analysis of the current at 222 m depth may be considered the SEUC core evaluation in time and space. At 30°W, the eastward current seems to meander with its northernmost velocity maximum position at 4.2°S in July-August, and its southernmost velocity maximum

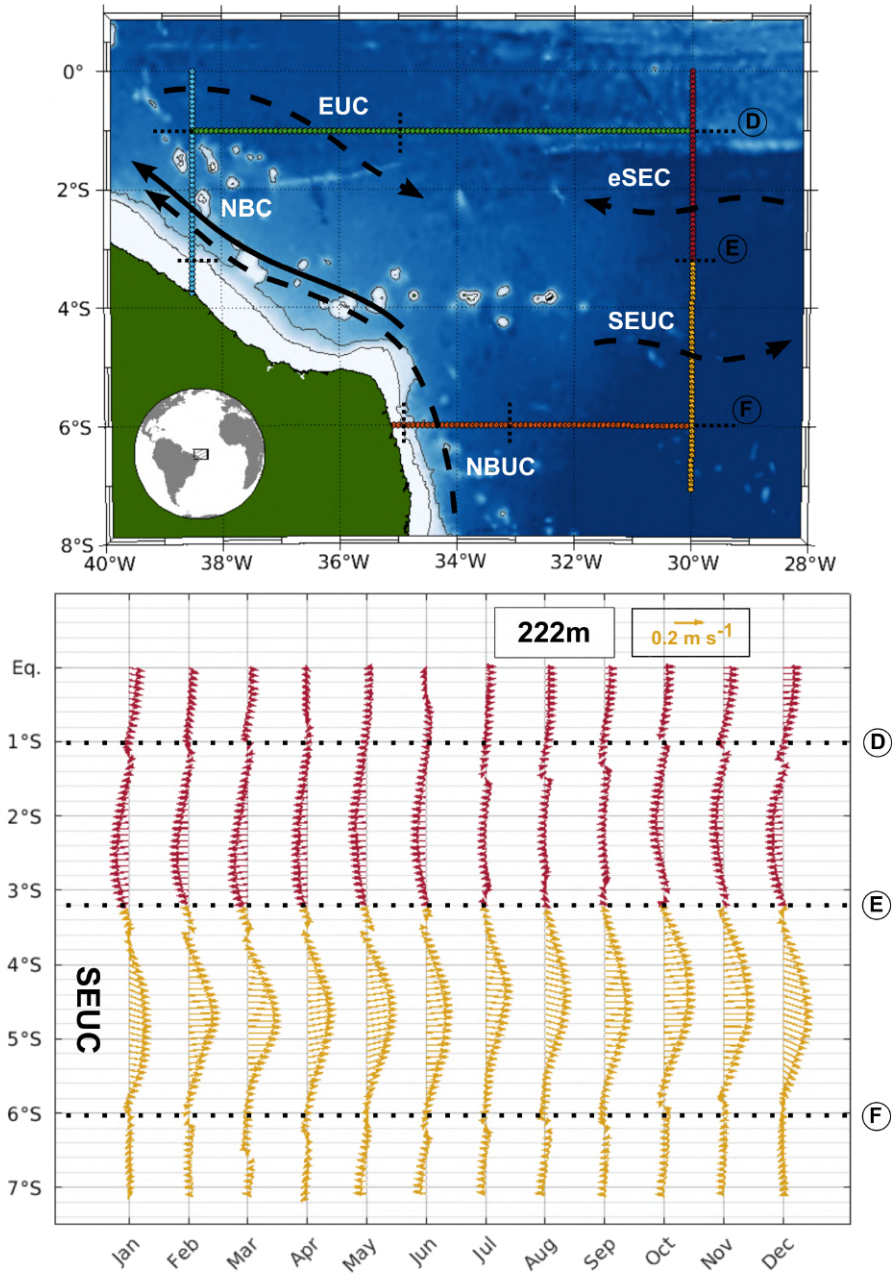

Figure 21 – Climatological seasonal hovmöller diagram of current velocity vectors at 222 m depth for the easternmost section in purple and yellow. The map indicates a schematic circulation and the delimitations for the eSEC (D-E slice in the upper figure) and for the SEUC (E-F slice in the upper panel) as also shown in dashed black lines in the hovmöller plot.

position at 4.7°S in January-May. Considering the current as whole in latitudinal extension, the SEUC is shifted north from July to December, being wider from September to December. In contrast, results indicate that the SEUC is shifted south from January to June, presenting a narrower meridional band during February-March. The maximum velocity varies from 0.23 m s^{-1} in March, to 0.15 m s^{-1} in January. South of 6°S, velocities reach up to 0.09 m s^{-1} in May-July, flowing westward, which might be associated with deeper portions of the cSEC.

4.2.2 Mean volume transport balance

The analysis of the volume transport balance can be thought a way to evaluate current contributions to the SEUC origin region, providing insights for the existing circulation paths that could be associated with the feeding of the SEUC. In this context, the mean water volume transport crossing the area of the SEUC origin were calculated, considering the same above considered horizontal boundaries used in the climatologic hovmöllers. The vertical boundaries were established as the vertical limits of the SEUC previously evidenced from observational characterization, as being the SEUC density range of $\gamma_n = 24.5$ to $\gamma_n = 27.2$. To evaluate seasonal and intraseasonal variations and eliminate unnecessary fluctuations for the present work, the transport time series were filtered using a lowpass Butterworth filter of cut-off period of 400 days.

Figure 22 shows the calculated mean volume transport into and out of the SEUC origin area. Positive and negative transports were referenced to the flux contribution for the SEUC origin region: positive values mean mass inflow into the rectangle and negative values mean mass outflow out of the rectangle. The SEUC origin region presents positive transports, i.e., receives water inflows from the southernmost section and the NBUC, from the northernmost section and the EUC, and from the eSEC. The negative transports, i.e., water outflows are accounted for in the westernmost section and in the NBC, and in the SEUC. Notice that the westernmost section and the NBC are equivalent, since the landward NBC limit is the bathymetric limitation at 222 m depth. Therefore, for practical reasons the westernmost section will be referred as the NBC transport hereafter. From the overall balance, represented by the sum of the sections' contributions, only $+0.86$ Sv remains without net identification. This difference is related to uncertainties, as the standard error calculated for the total transport is 0.51 Sv, and one may speculate that it might be due to diapycnal transports at the western tropical Atlantic boundary.

At the southernmost section, the NBUC accounts for 23.77 Sv of the 24.68 Sv mass transport, and another 0.91 Sv reaches the region from the east portion of the section. This residual can be related to contributions from the cSEC or even from meanderings of the SEUC. Considering the climatological hovmöller for this section previously analyzed, the velocity field indicates inflows of northeastward direction, which lead us to affirm that the 0.91 Sv contribution might be mainly transported to the SEUC. The northernmost section encompasses the EUC inflow, which partially leaves the region through the east portion of the same section, and the other fraction might recirculate to the NBC and/or it might join the SEUC. Some authors affirmed that the eSEC impinges at the Brazilian continental margin from the east, and feeds the NBC northwestward (SCHOTT; FISCHER; STRAMMA, 1998; STRAMMA; ENGLAND, 1999). Other authors also stated that the SEUC is fed by equatorial recirculations entrained in the eSEC and reentered to the SEUC (FISCHER et al., 2008). Therefore, the eSEC

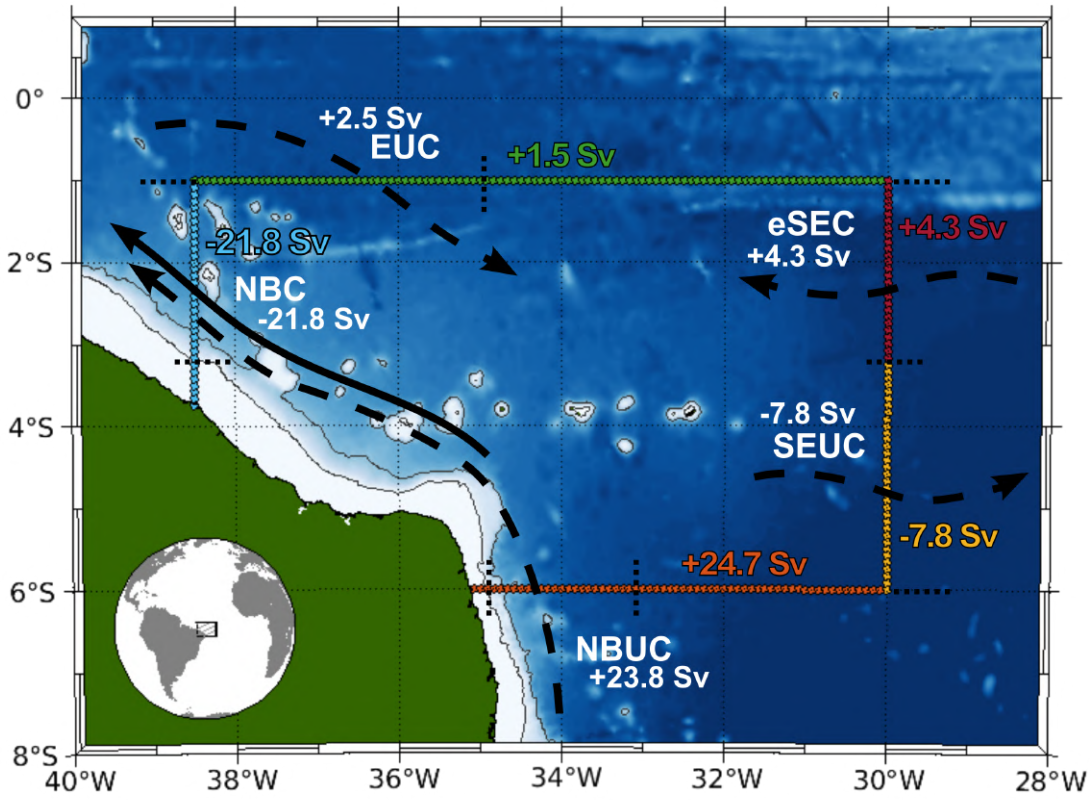

Figure 22 – Mean water mass transport at the region of the SEUC origin in the western tropical Atlantic boundary, considering circulation components arising from the NBUC, NBC, EUC, eSEC, and SEUC.

might partly feed the NBC and might also contribute to the SEUC mass transport. Assuming the northernmost net inflow from the EUC does not recirculate to the NBC and admitting no contribution from the eSEC to the NBC, the SEUC mass flux remains unbalanced. Taking into account the 0.91 Sv contribution as part of the southernmost section, the northernmost section inflow of 1.51 Sv, and the eSEC transport of 4.29 Sv, the sum represents 6.71 Sv inflow and the SEUC outflow is 7.83 Sv. Consequently, the NBUC is indeed connected to the SEUC and contributes to the mass transport balance of that current.

Still looking for more indications about the currents' connection, in particular NBUC, SEUC and eSEC, some basic statistics were extracted and calculated from the filtered transport time series of each section (Table 6). The NBC is presented as the circulation component with the lowest peak-to-peak transport range of 33.57 Sv, standard deviation of $\pm$ 4.58 Sv, similar mean and median, and a very symmetric distribution. The EUC also exhibits a symmetric distribution with a moderate peak-to-peak range and standard deviation compared to the other currents.

On the other hand, the NBUC, SEUC and eSEC show more asymmetrical distributions (Figure 23). The NBUC distribution is slightly positively skewed, with a small right tail indicating fewer but important outliers. The current transport has low peak-to-peak range and

Section	**Minimum**	**Maximum**	**Median**	**Mean**	**S. Deviation**	**S. Error**
Southermost	2.42	41.64	24.86	24.68	± 4.87	± 0.05
NBUC	4.88	41.37	23.67	23.77	± 4.83	± 0.05
Westernmost	-39.28	-5.71	-21.78	-21.79	± 4.58	± 0.05
NBC	-39.28	-5.71	-21.78	-21.79	± 4.58	± 0.05
Northernmost	-20.38	23.67	1.57	1.51	± 6.40	± 0.07
EUC	-19.52	28.11	2.56	2.52	± 5.94	± 0.06
Easternmost	-26.67	29.56	-3.56	-3.54	± 6.77	± 0.07
eSEC	-14.81	24.37	4.62	4.29	± 5.45	± 0.06
SEUC	-29.12	27.66	-8.29	-7.83	± 6.67	± 0.07

Table 6 – Basic statistics of the filtered volume transport time series from the different sections bordering SEUC origin region. All statistical variables here presented are in Sverdrup (Sv) units.

standard deviation values. The eSEC curve is negatively skewed and the left tail of negative transports reveals some negative outliers, i.e., outflow peaks. The SEUC shows the highest peak-to-peak range of 56.78 Sv and standard deviation of 6.67 Sv. The SEUC transport

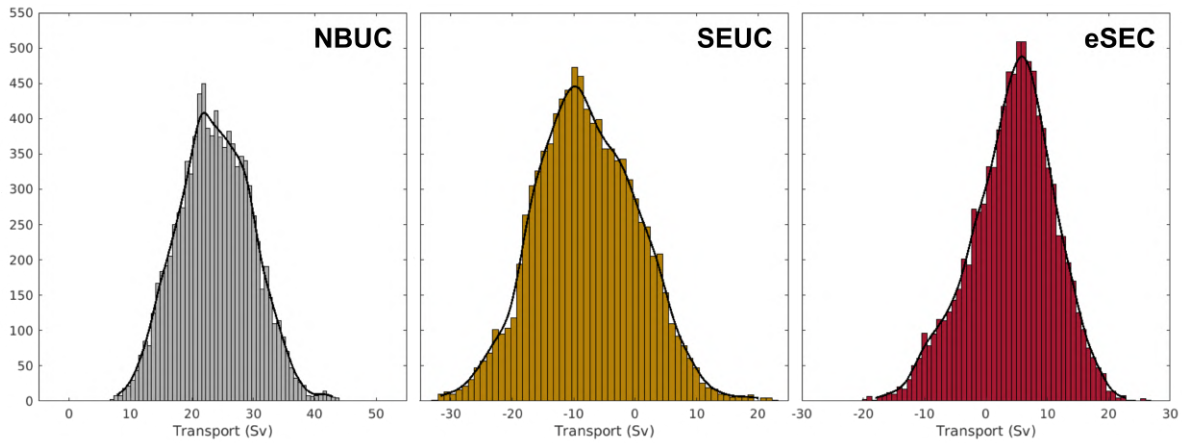

Figure 23 – Probability distributions for the eSEC (purple), NBUC (gray) and SEUC (yellow).

distribution has positive skewness, exhibiting peaks of inflows and the greatest median-mean difference among the all analyzed currents, with a median 0.46 Sv lower than the calculated mean value. The SEUC median, a more representative central tendency for skewed distributions, is equivalent to an outflow of 8.29 Sv from the region. The inflow and outflow peaks could be related to high mesoscale activity associated to meandering and eddies. Note the high standard deviations for the northernmost and easternmost sections. As previously suggested in this work, and also observed by Fischer et al. (2008), the SEUC shows important meanders at the western boundary of the tropical Atlantic region.

4.2.3 The SEUC vs. AMOC transport long-term variability

A question that long-time series poses to us is how interannual variabilities and tendencies are related to climate changes in the ocean. According to McCreary, Lu e Yu (2002), the SEUC correspondent in the Pacific ocean, i.e. the Southern Subsurfaces Countercurrent (SSCCs), is remotely forced by the Indonesian throughflow. They suggest that the SEUC, as its counterpart in the Atlantic, could be driven by the Atlantic Meridional Overturning Circulation (AMOC). Through a decade of *in situ* measurements at 26°N, Srokosz e Bryden (2017) observed a decrease of the AMOC. After a 180-day filter for the period of 2004 to 2014, this decline was calculated as 0.5 Sv per year.

We decide to investigate how the SEUC transport can be responsible for the AMOC transport northward. In otder to do so, we filter the GLORYS12V1 outpus with the same 180-day-filter, and consider the same time period analized by Srokosz e Bryden (2017): 2004-2014 period (Figure 24). For the SEUC transport at 30°W, we observe an increase of 0.47 Sv per year. The similar decrease/increase of the AMOC/SEUC suggests a relation between them, as a possible leakage of the thermohaline circulation to the zonal equatorial current. This is just a first hint in this topic, since there are other eastward-flowing equatorial jets (i.e., South Equatorial Countercurrent, North Equatorial Undercurrent and North Equatorial Countercurrent) that can account such leakage as well as SEUC. Nevertheless, the simple and preliminary calculation presented here is encouraging to be pursued and deserves a note.

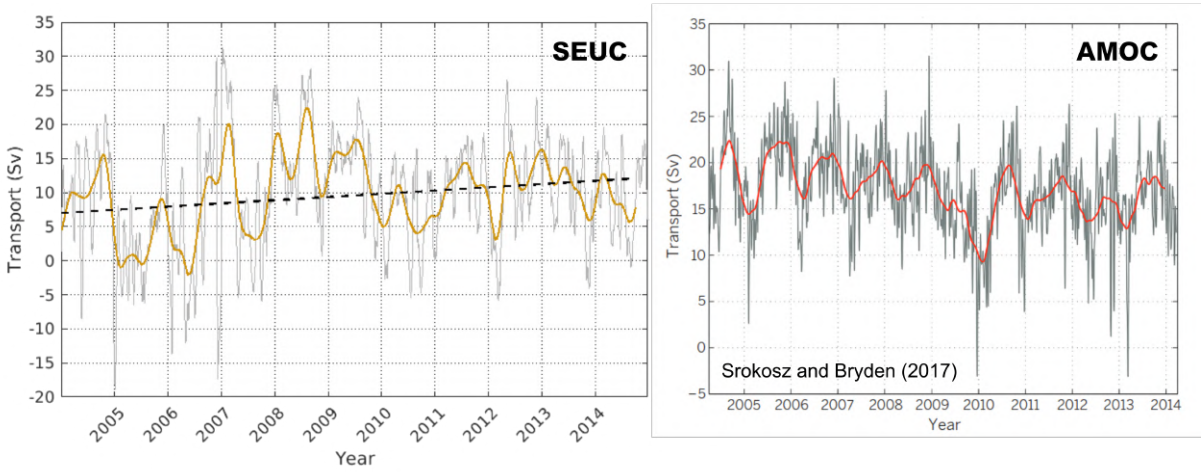

Figure 24 – The 10-year time serie of the SEUC transport at 30°W (left pannel) and of the AMOC at 26.5°N (right pannel). The gray lines indicate indicate the 10-day-filtered time series in both pannels, the yellow solid line in the left pannel represents the 180-day-filtered SEUC transport, the dashed black line in the left pannel illustrates the SEUC trend for 2004-2014 and the red line in the right panel correspond to the 180-day-filtered AMOC transport. The right pannel is the Figure 2 from Srokosz e Bryden (2017).

4.2.4 Seasonal to intraseasonal variability

Finally, in order to evaluate more precisely how the energy in the volume transport series is distributed in different time scales of seasonal to intraseasonal variations, a spectral analysis was carried out for each analyzed currents with the focus on the SEUC connections. The frequency distributions of the transport time series, i.e. the power spectral density (PSD), were computed usig the Welch's periodogram method with a 2048-day-wide Kaiser-Bessel window and 50% (1024 days) of overlap (WELCH, 1967; EMERY; THOMSON, 2014). Among the analyzed PSDs, the eSEC and NBUC frequency distributions were very similar to the SEUC distribution. In Figure 25, the percentages indicate the relative amount of variance for three different period ranges: 14-35 days, 35-100 days and 100-400 days. The currents show approximately the same variance proportions, with a larger portion of the variance for lower (higher) frequencies (periods), an intermediary and still large portion for the 35-100 days band, and a smaller portion for higher (lower) frequencies (periods). The eSEC shared variance peaks with the SEUC around 75 days and 180 days, with smaller peaks close to 60 days and 120 days. Moreover, the NBUC transport also shared some variance peaks with the SEUC at 60 days, 75 days and 120 days, presenting a smaller peak at 180 days.

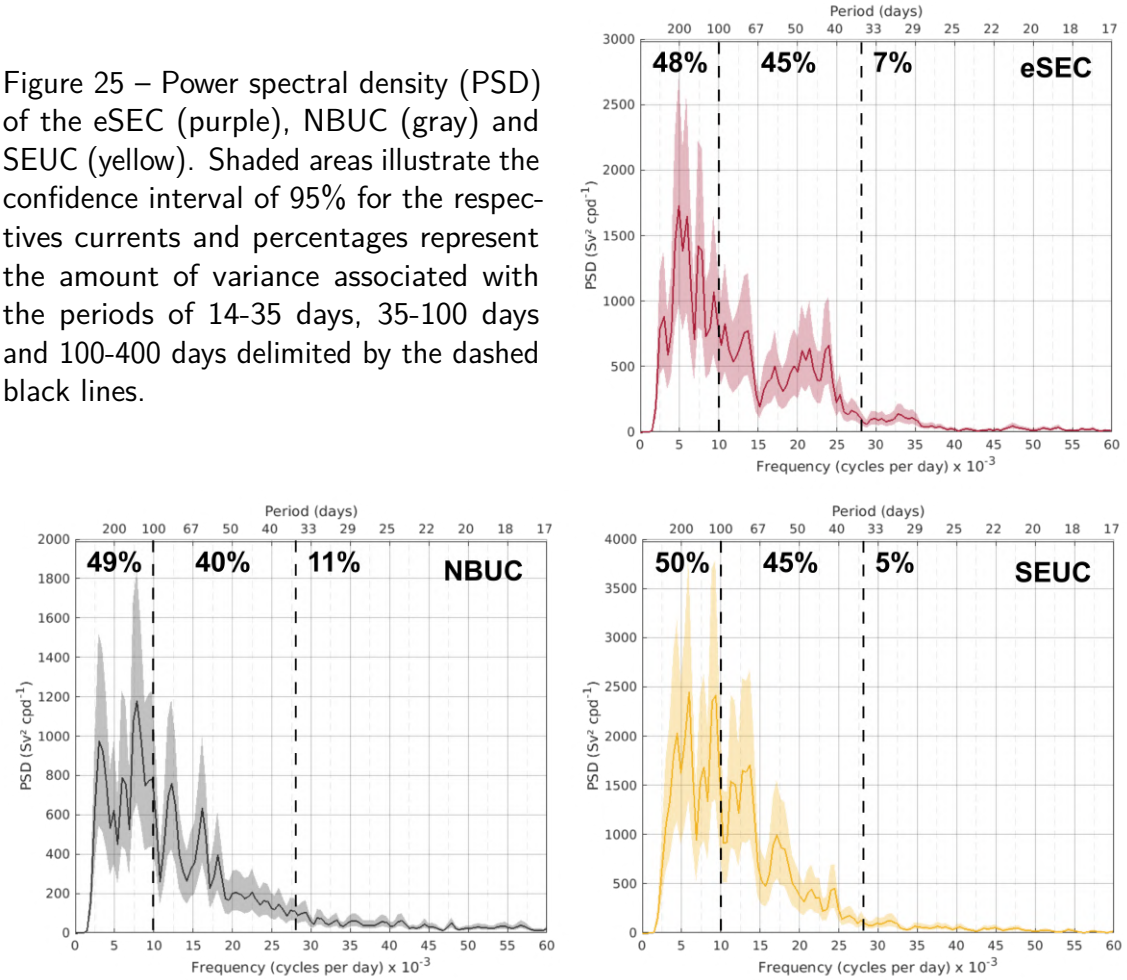

Figure 25 – Power spectral density (PSD) of the eSEC (purple), NBUC (gray) and SEUC (yellow). Shaded areas illustrate the confidence interval of 95% for the respectives currents and percentages represent the amount of variance associated with the periods of 14-35 days, 35-100 days and 100-400 days delimited by the dashed black lines.

The similarities between the eSEC and the SEUC variability in time scale is expected since the scientific community agrees that the SEUC is fed by the deeper portion of the eSEC from the north. However, the NBUC-SEUC resemblances of variance proportions and common peaks reinforce the connection between the currents. From the power spectral density analysis in Figure 25, it is clear the relevance of the intraseasonal variability, with the 35-100-days variations representing 45% of the SEUC variance at the western tropical Atlantic boundary. The mesoscale variability must play an important role for the SEUC origin dynamics, as we will discuss in the next Section.

4.3 Mesoscale Activity

The western tropical Atlantic boundary is a region strongly affected by dynamical processes of mesoscale variability. The tropical instability waves (TIW) depart eastward between 5°S and 5°N, with energy propagation down to 600m depth (DUEING et al., 1975; DECCO et al., 2018). Schuckmann, Brandt e Eden (2008), highlighted the 4-5°S band as an important energy source for the TIW. Between 0° and 4°S, Specht, Jungclaus e Bader (2021) observed subsurface TIW detached from the TIW at the surface. Coastal trapped waves (CTW) were also observed along the northeast Brazilian margin (VELEDA et al., 2012). Moreover, Fischer et al. (2008) noted a meandering pattern at the westernmost portion of the SEUC, which was confirmed by the observational characterization previously presented in this work. Furthermore, our previous power spectral density analysis evidence the relevant intraseasonal variability linked to the mesoscale activity at the SEUC origin region.

4.3.1 Eddy spatial distribution and percentual ocurrence frequency

To better understand the SEUC dynamics related to the intraseasonal variations associated with the supracited motions and phenomena, an hybrid eddy detection tracking method was used at the study region. The Angular Momentum Eddy Detection and tracking Algorithm (AMEDA) was applied on GLORYS12V1 outputs at the 222 m depth, as the SEUC core depth. The Figure 26 shows the eddies' trajectories in the Tropical Atlantic western boundary from 1993 to 2018. Note that the trajectories illustrated represent the barycenter positions of the eddy's characteristic contour. In the upper and right outer panels, the figure also illustrates the eddy counts for their formation positions in longitudes and latitudes, respectively. The anticyclonic eddies are represented in red, and the cyclonic eddies are indicated in blue, as they will be represented hereafter. A total of 1336 eddies were detected at the region, 625 (47%) being anticylonic eddies and 711 (53%) being cyclonic. Most of the eddies show the formation position at the easternmost longitudinal position, around 27°W. These formation points indicate the eddies were not necessarily formed at this position, but it was where they

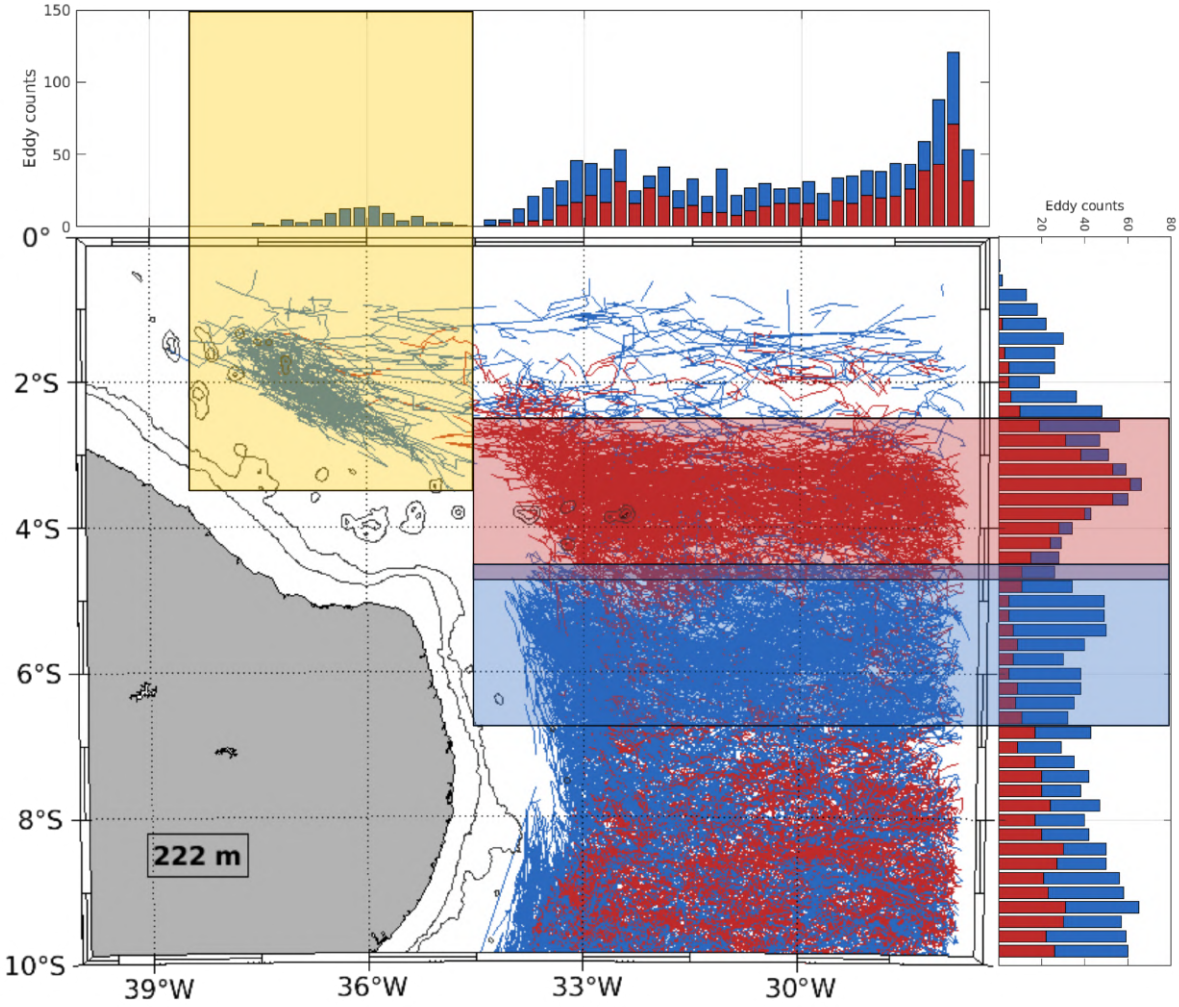

Figure 26 – Eddy trajectories on the western tropical Atlantic boundary and eddy counts for longitudes and latitudes of eddy formation. Anticyclonic eddies are marked in red and cyclonic eddies are represented in blue. The boxes indicate the bands of relevant eddy occupation, as the cyclonic band (blue), anticyclonic band (red) and the NBC band (yellow).

were firstly detected at the region. These eddies, found at 27.2°-28.6°W, were probably formed eastward of 27°W, accounting for 27% (364) of the total eddies distributed between 27.2°W and 37.6°W. The proportions between anticyclonic and cyclonic eddies are approximately the same east of 33°W. West of 33°W, cyclonic eddies predominate, as we can see the dominance of cyclones trajectories along the whole Brazilian coast. These cyclonic eddies in the landward region might be associated with the presence of the strong western boundary currents, the NBUC-NBC system. West of 35°W, no anticyclonic eddies were detected. In latitude, the eddy formation positions are more equally distributed, when compared to the longitudinal distribution. The longitudinal peak reaches 121 counts, while the latitudinal peak is of 55 counts. The anticyclones-cyclones proportions maintain approximately the same south of 6.8°S. North of approximately 3.4°S, cyclones predominate over anticyclones, mainly because no anticyclones are present west of 34.5°W as already mentioned. West of 34.5°W, cyclones propagate northwestward along the NBC limits, following the Brazilian coast. Between 6.8°S

and 2.5°W and east of 35°W, two distint bands contrast at the region: at 4.6°-6.8°S, dominated by cyclonic eddies; and at 2.5°-4.8°S, predominantly occupied by anticyclonic eddies. These bands' interface limit coincide with the SEUC position, and the eddies trajectories propagate westward along the northern and southern limits of the SEUC, following the meandering pattern of the current.

Considering the eddies' trajectories and formation positions, three areas appear important in Figure 26: (i) the cyclonic band (4.6-6.8°S, 27.5°-34.5°W), with 308 detected eddies and 79% of cyclones; (ii) the anticyclonic band (2.5°-4.8°S, 27.5°-34.5°W), with 304 detected eddies and 87% of anticyclones; and (iii) the NBC band (0°-3.4°S, 34.5°-38.5°W), with 87 detected eddies and no anticyclones formed at the area. In order to visually identify the areas on the map where the eddies are confined more often from 1993 to 2018, the eddy frequency was calculated as the percentage of time when at least one eddy was passing the location (Figure 27). The frequency of the total amount of eddies is higher around 3.5°S and 32.5°W, reaching frequencies of 34%. Note the meandering pattern of low eddy frequencies along the latitude of approximately 4.5°S, corresponding to the SEUC position. The cyclonic eddies reach eddy frequencies of 24% around 5.8°S and 33.3°W, with another less intense patch of high frequencies ($\approx$ 22%) close to 5.7°S and 30.7°W. West of 34.5°W, an isolated patch exhibit eddy frequencies of 11%. The anticyclones are more frequent around the 3.5°S-32.5°W location, with values up to 33%. Once again, the cyclonic, the anticyclonic and the NBC bands are evidenced as pathways of subsurface eddies at the western tropical Atlantic boundary.

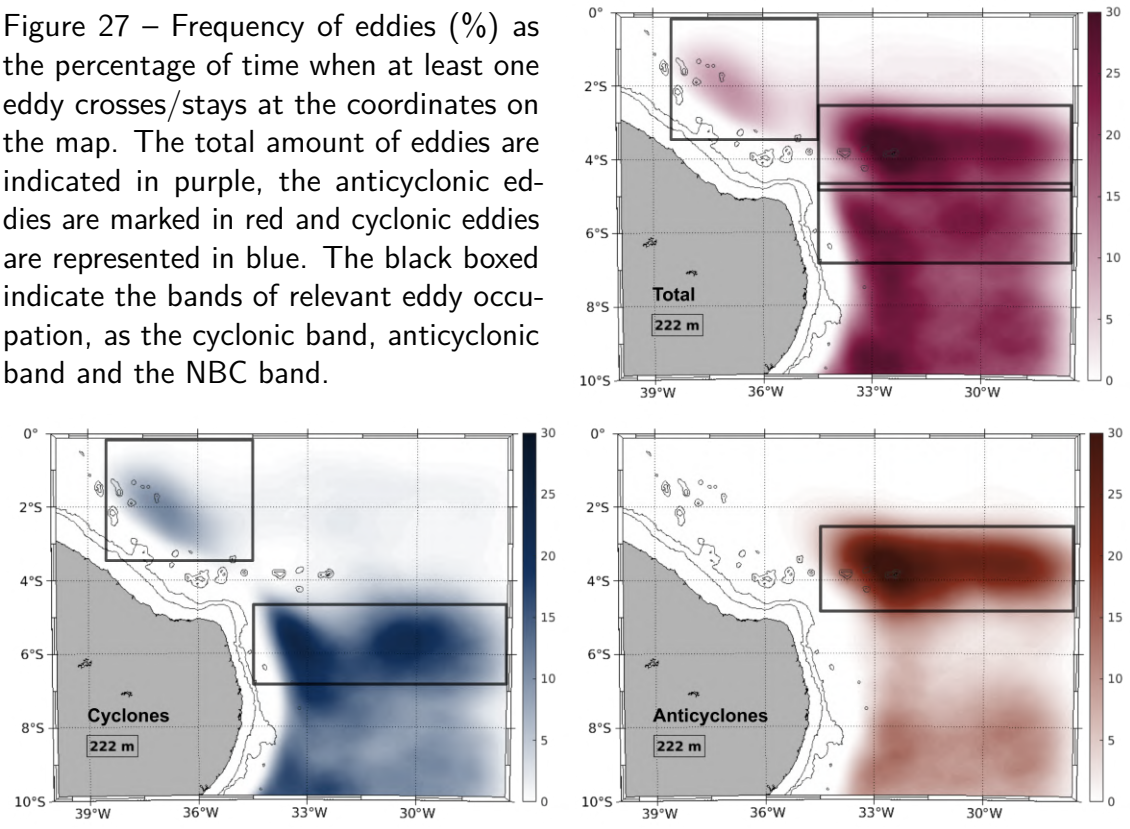

Figure 27 – Frequency of eddies (%) as the percentage of time when at least one eddy crosses/stays at the coordinates on the map. The total amount of eddies are indicated in purple, the anticyclonic eddies are marked in red and cyclonic eddies are represented in blue. The black boxed indicate the bands of relevant eddy occupation, as the cyclonic band, anticyclonic band and the NBC band.

To better understand and visualize the large and associated mesoscale circulation at the western tropical Atlantic boundary, the snapshot map of the velocity and vorticity fields in 08-August-1999 is shown at 222 m depth (Figure 28). The eddies detected by the AMEDA are highlighted in contours, with cyclonic circulations in blue and anticyclonic circulations in red. South of 6°S and close to 33°W, an anticyclonic eddy is present off the continental margin. Along the Brazilian coast, the NBUC flows northward following the topography, turning northwestward after the Cape Calcanhar to become the NBC. It is possible to observe the anticyclonic Potiguar Eddy (PE) at 4.5°S and 36°W. Around 4.5°S, the SEUC flows eastward limited by cyclones and anticyclones flowing westward at its southward and northward portions, respectively. Associated with the mesoscale circulation, the SEUC meandering pattern appears extremelly evident at this region, ranging more than 3 degrees of latitude.

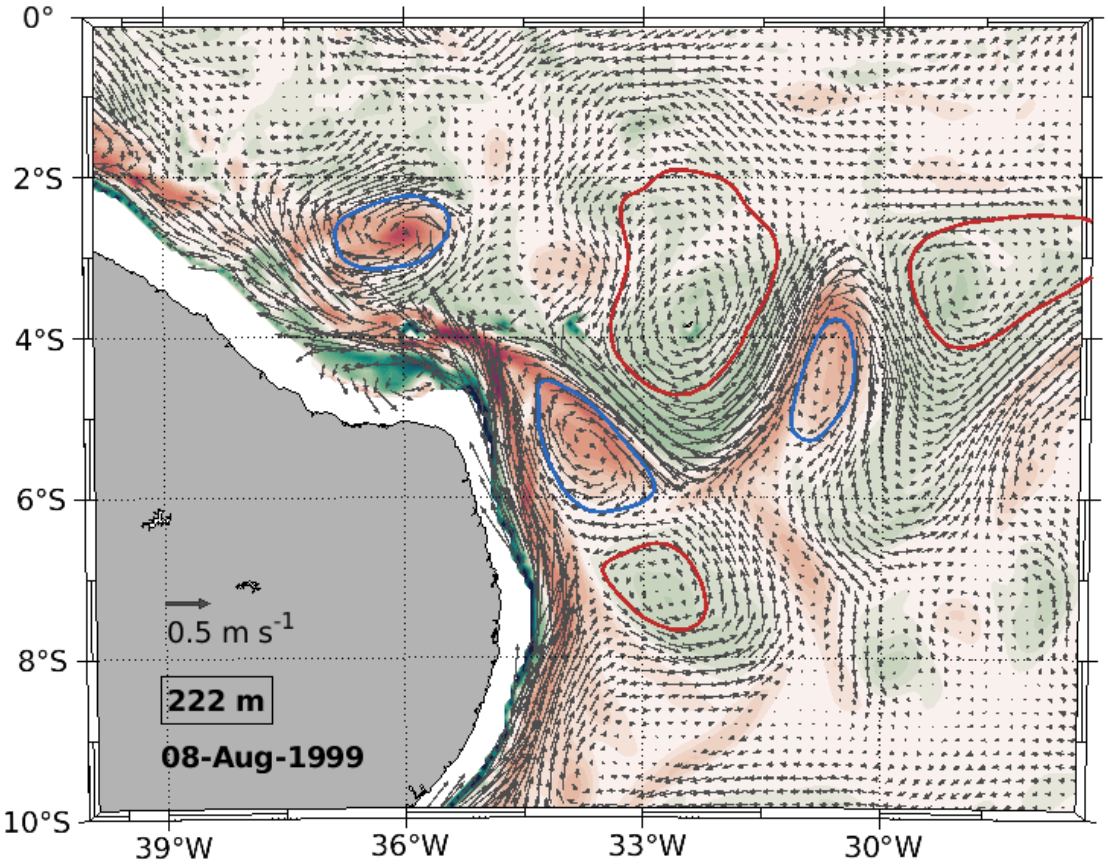

Figure 28 – Distribution of relative vorticity (colors) and velocity fields (arrows), and detected anticyclonic (red contours) and cyclonic eddies (blue contours) on 08 August 1999.

At approximately 3.5°S and 33.5°W, the SEUC is fed by the deeper portion of the eSEC flowing westward around 2°S, north of the former current. This supply from the eSEC to the SEUC seems to be enhanced by the anticyclone around 4°S and 32.5°W. More specifically at 5.5°S and 33.5°W, we observe a cyclonic eddy at the eastern NBUC limit and at the southern SEUC limit. The NBUC-SEUC connection is, once again, evident and it is associated and reinforced by the cyclonic circulation at this location. Around 3°S and 36°W, a

cyclone is observed dettaching from the location of the NBUC-SEUC connection to propagate northwestward.

Accordingly, the SEUC is a meandering current located around 4.5°S, limited by cyclonic and anticyclonic circulations propagating westward at, respectively, its southward and northward limits: the SEUC eddies. Along the Brazilian continental margin, the NBUC flows northward, retroflects around 4.5°S and 34.5°W to feed the SEUC, shedding eddies northwestward in connection with and along the NBC: the NBUC eddies. The SEUC and NBUC eddies are, to our knowledge, so far unknown. The mesoscale activity at the SEUC origin region might be the responsible for the presence of oxygen-rich South Atlantic waters found in the SEUC and also the presence of oxygen-poor Eastern Atlantic waters found in the NBUC-NBC system.

4.3.2 Eddy characterization

After previously investigating and defining the three eddy-rich bands associated with the SEUC dynamics, we analyzed the eddies characteristics of each band. Before proceding with the analysis, we must recollect the definition of characteristic contours as the closed streamline contour of maximum azimuthal velocity. The characterization involved the density distribution of seven different variables: (i) area delimited by the characteristic contour; (ii) equivalent radius of a circle with the same area of the characteristic contour; (iii) lifetime of the eddy; (iv) mean azimuthal velocity averaged along the characteristic contour; (v) sum of the kinetic energy inside the characteristic contour; (vi) mean vorticity inside the characteristic contour; and (vii) Rossby number calculated.

In Figure 29, the density distributions of the area, the radius and the lifetime are illustrated for the cyclonic, the anticyclonic and the NBC bands. Table 7 summarizes the basics statistics for the variables at each of the analyzed bands. The eddies in the cyclonic band present aparent smaller areas than the anyicyclones in the north. Within the anticyclonic band, the areas are greater and the distribution is more spread, expressed by the higher standard deviation. Eddies in the NBC band have intermediate area sizes and show lesser variations, with the lowest standard deviation. As expected, the radii follow the same tendency observed with their area. The total eddy radii ranged from 44.3 km at the cyclonic band to 156.3 km at the anticyclonic band. The minimum eddy lifetime was 5 days for all of the bands, since a time filter was used to eliminate eddies of too short life spans. The cyclonic band showed longer eddies on average, with the highest standard deviation of 32 days. On the other hand, the eddies at the NBC band presented the shortest lifetimes, with maximum values of 45 days. Since the region of eddy detection used for the AMEDA method was limited northward by the equator, it must be noted that the eddies at the NBC band might have travelled shorter distances when compared to the other bands. The eddies in the anticyclonic band revealed similar with the life spans observed at the cyclonic band.

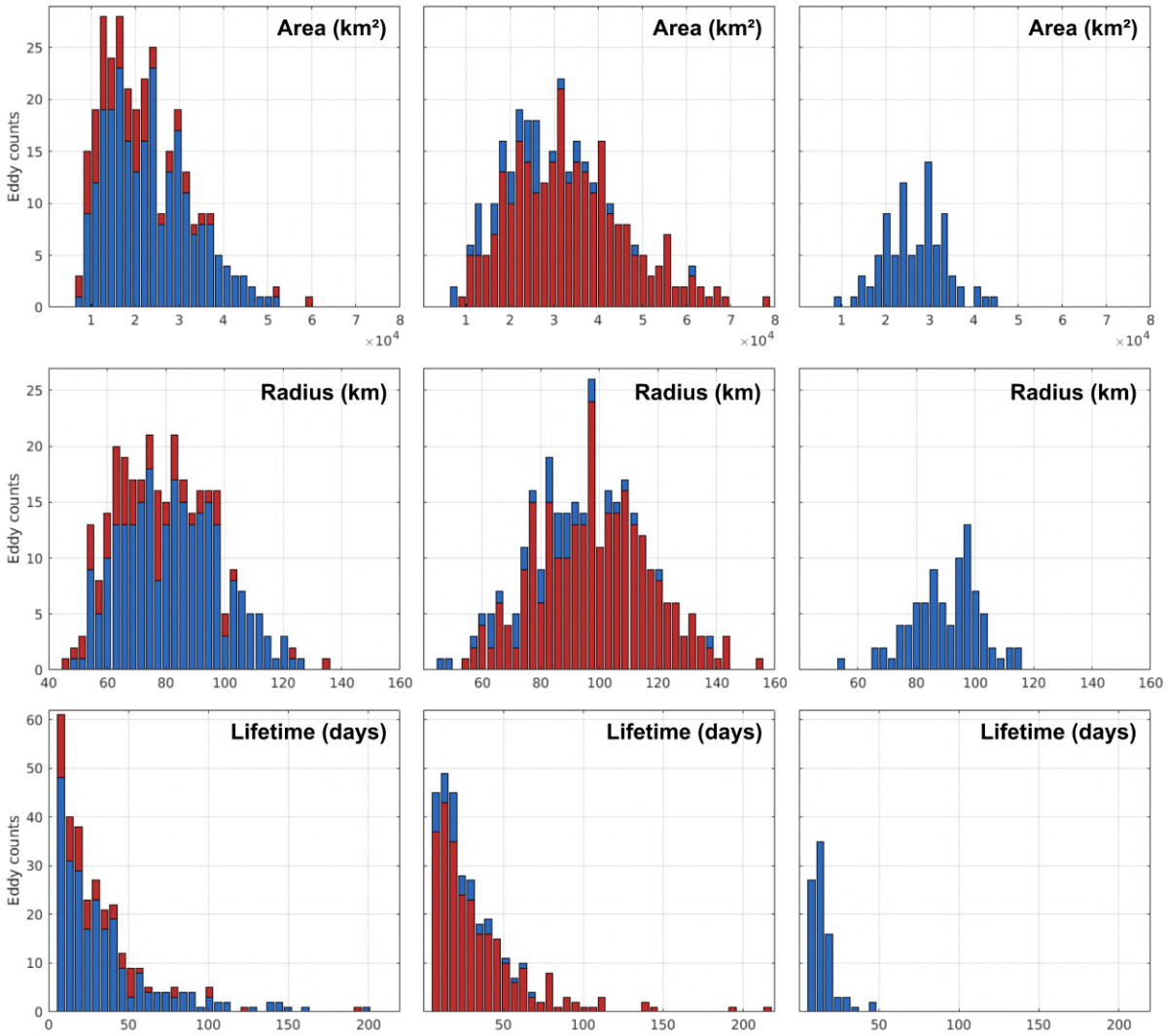

Figure 29 – Density distribution of eddies characteristics - area, radius and lifetime - for the cyclonic band (left panels), the anticyclonic band (middle pannels) and the NBC band (right panels). Anticyclonic eddies are marked in red and cyclonic eddies are represented in blue.

The density distributions for the swirl velocity, the kinetic energy, the vorticity and the Rossby number were also analyzed at the cyclonic, the anticyclonic and the NBC bands (Figure 30). Again, the following Table 8 summarizes the basic statistics of these variables at each band. The swirl velocity, i.e. the mean azimuthal velocity, show no significant difference between the cyclonic and anticyclonic bands, with median velocities of 0.18 m s^{-1}. The eddies within the NBC band, however, are significantly faster compared to the other bands, with velocities up to 0.58 m s^{-1} and median equivalent to 0.35 m s^{-1}. This difference between the SEUC eddies and the NBUC eddies might be related to the association of the latter with the strong western boundary current, i.e. the NBUC-NBC system flowing northwestward. For kinetic energy, the distributions change significantly between the analyzed bands. The cyclonic band shows eddies with lower kinetic energy, the anticyclonic band presents intermediate values, and the NBC band reveal significantly higher kinetic energy, with median of 11.48 m^2 s^{-2}. Note that the eddies at the NBC band show a wider variations of kinetic energy values, with a range

Bands	Minimum	Maximum	Median	Mean	S. Deviation	S. Error
Area ($\times$ 10^4 km^2)						
Cyclonic	0.6	5.8	2.1	2.2	$\pm$ 1.0	$\pm$ 0.06
Anticyclonic	0.7	7.8	3.1	3.2	$\pm$ 1.3	$\pm$ 0.07
NBC	0.9	4.4	2.7	2.7	$\pm$ 0.7	$\pm$ 0.07
Radius (km)						
Cyclonic	44.3	133.7	79.2	80.5	$\pm$ 17.1	$\pm$ 0.97
Anticyclonic	46.9	156.3	96.7	96.8	$\pm$ 19.8	$\pm$ 1.14
NBC	54.7	115.6	92.2	90.3	$\pm$ 11.8	$\pm$ 1.26
Lifetime (days)						
Cyclonic	5	200	25	35	$\pm$ 32	$\pm$ 1.8
Anticyclonic	5	218	23	33	$\pm$ 29	$\pm$ 1.7
NBC	5	45	13	14	$\pm$ 7	$\pm$ 0.7

Table 7 – Basic statistics of the area, radius and lifetime for the eddies at the cyclonic, the anticyclonic and NBC bands.

of 32.91 m^2 s^{-2} and standard deviation of 7.26 m^2 s^{-2}. Due to the higher standard deviation and smaller sample size for this band, the standard error is also higher when compared to the other bands. Despite of that, the higher median kinetic energy for the NBC band is related to the greater velocities of these eddies. The difference between the kinetic energy distributions of the cyclonic and anticyclonic bands might be related to the greater surface area of the eddies at the latter band, since the variable was calculated as the sum of kinetic energy inside the eddy. Note that the vorticity in Table 8 for the cyclonic (anticyclonic) band considered only the cyclonic (anticyclonic) eddies. Moreover, to simplify and enable a comparison between the bands, the minimum and maximum values for the anticyclonic eddies were listed and analyzed in respect to their absolute values. No significant difference is observed between the cyclonic and the anticyclonic bands, with median vorticity of 0.50 $\times$ 10^{-5} s^{-1} and -0.39 $\times$ 10^{-5} s^{-1}, respectively. Again, higher vorticity values are found for the eddies at the NBC band, with a median of 0.86 $\times$ 10^{-5} s^{-1}. The Rossby number, calculated from the ratio between the swirl velocity and the product of the radius and the Coriolis parameter, is used to compare the importance of the relative vorticity to the planetary vorticity. The main reason for the differences found between the analyzed bands are the Coriolis parameters for each of these areas. The proximity with the equator influences the calculated Rossby numbers, with the eddies at the NBC band presenting the significantly higher values of median equivalent to 0.76. Of course, the greater swirl velocities of the eddies at this band also impact on the higher Rossby numbers.

The Okubo-Weiss (OW) parameter enables the detection of eddies through the quanti-

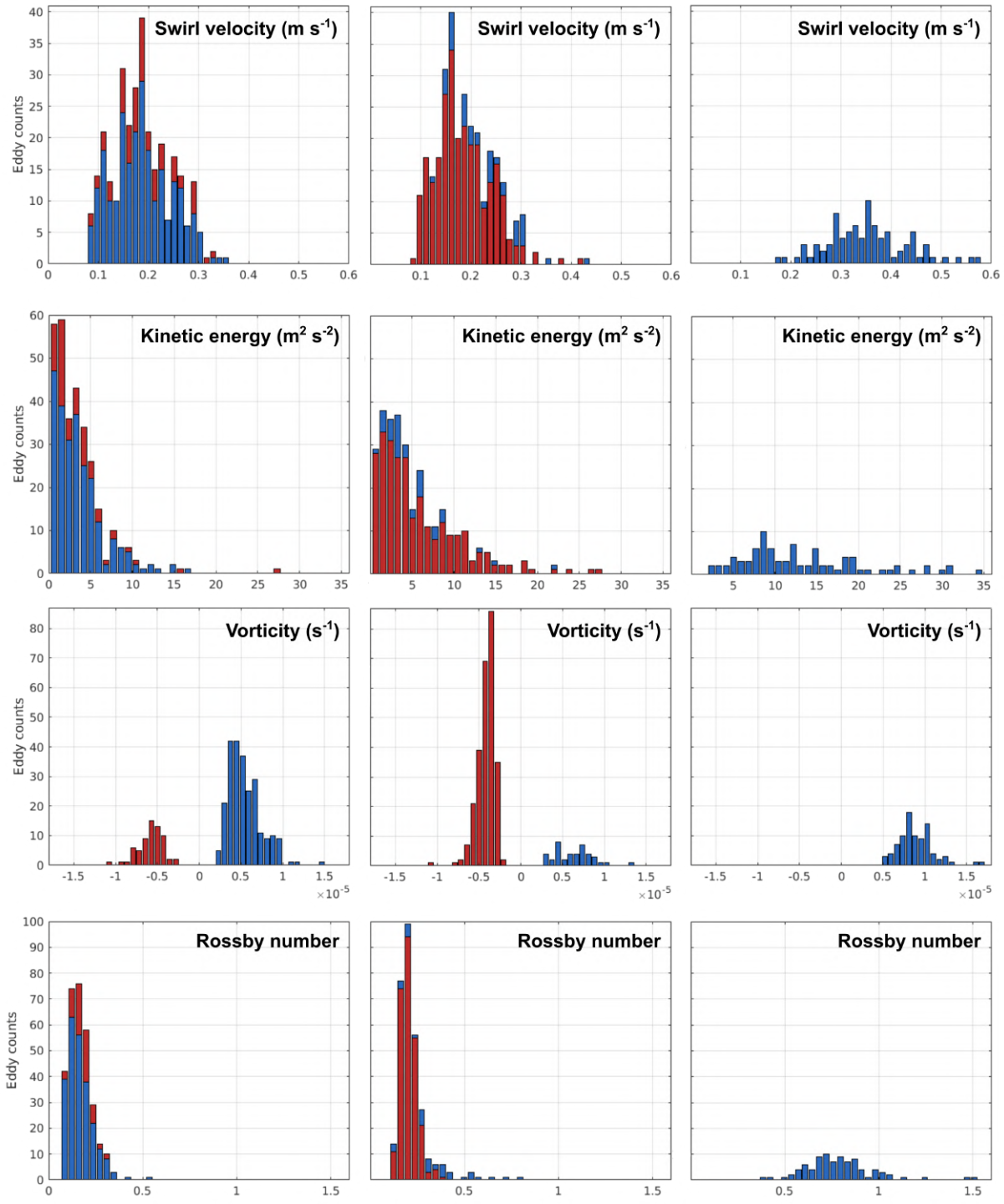

Figure 30 – Density distribution of eddies characteristics - velocity, kinetic energy, vorticity and Rossby number - for the cyclonic band (left panels), the anticyclonic band (middle pannels) and the NBC band (right panels). Anticyclonic eddies are marked in red and cyclonic eddies are represented in blue.

fication of the relative importance of vorticity in respect to shearing and straining deformations. Negative OW values are present inside the vortex. To characterize the vertical structure of the SEUC and the NBUC eddies, the OW parameter was calculated for the sections at 30°W and 37°W (Figures 31 and 32, respectively).

Bands	Minimum	Maximum	Median	Mean	S. Deviation	S. Error
Swirl velocity (m s^{-1})						
Cyclonic	0.08	0.35	0.18	0.19	± 0.06	± 0.003
Anticyclonic	0.08	0.43	0.18	0.19	± 0.06	± 0.003
NBC	0.18	0.58	0.35	0.35	± 0.08	± 0.009
Kinetic energy (m^2 s^{-2})						
Cyclonic	0.18	27.24	2.87	3.55	± 3.19	± 0.182
Anticyclonic	0.50	27.36	4.12	5.59	± 4.75	± 0.272
NBC	1.98	34.89	11.48	13.13	± 7.26	± 0.778
Vorticity ($\times$ 10^{-5} s^{-1})[a]						
Cyclonic	0.22	1.46	0.50	0.54	± 0.19	± 0.011
Anticyclonic[b]	-0.21	-1.12	-0.39	-0.41	± 0.11	± 0.006
NBC	0.53	1.72	0.86	0.89	± 0.21	± 0.022
Rossby number						
Cyclonic	0.07	0.54	0.16	0.17	± 0.06	± 0.003
Anticyclonic	0.11	0.81	0.20	0.22	± 0.09	± 0.005
NBC	0.40	1.52	0.76	0.79	± 0.19	± 0.020

[a] The vorticity of the cyclonic (anticyclonic) band take into account only the cyclonic (anticyclonic) eddies.

[b] For the anticyclonic eddies, the vorticities were considered and listed here as their absolute values to enable and simplify the comparison between the bands.

Table 8 – Basic statistics of the swirl velocity, kinetic energy, vorticity and Rossby number for the eddies at the cyclonic, the anticyclonic and NBC bands.

In Figure 31, snapshots of a cyclone and a anticyclone were selected to exemplify each type of mesoscale circulation, and it was also calculated an average of the vertical OW distribution of the section for the period of 1993-2018. On 05-January-1996, we can observed a cyclonic eddy around 5°S. The negative values of OW parameter indicate the vertical extension of the eddy, with stronger negative values between the isopycnals of $\gamma_n = 24.5$ and $\gamma_n = 27.2$, and reaching depths of 900m. On 30-January-1997, the anticyclonic eddy shows weaker negative OW values concentrated between the $\gamma_n = 24.5$ and $\gamma_n = 27.2$ isopycnals, with no vertical extension beyond approximately 500m depth. The averaged vertical distribution of the OW parameter show strong negative values at 4.5°-6°S ($\approx$ cyclonic band), mainly constrained between the $\gamma_n = 24.5$ and $\gamma_n = 27.2$ isopycnals, but also extending vertically over 900m depth. Between 4°S and 2.2°S ($\approx$ anticyclonic band), the negative patch is observed weaker and mostly comprised between the $\gamma_n = 24.5$ and $\gamma_n = 27.1$ isopycnals. This difference between

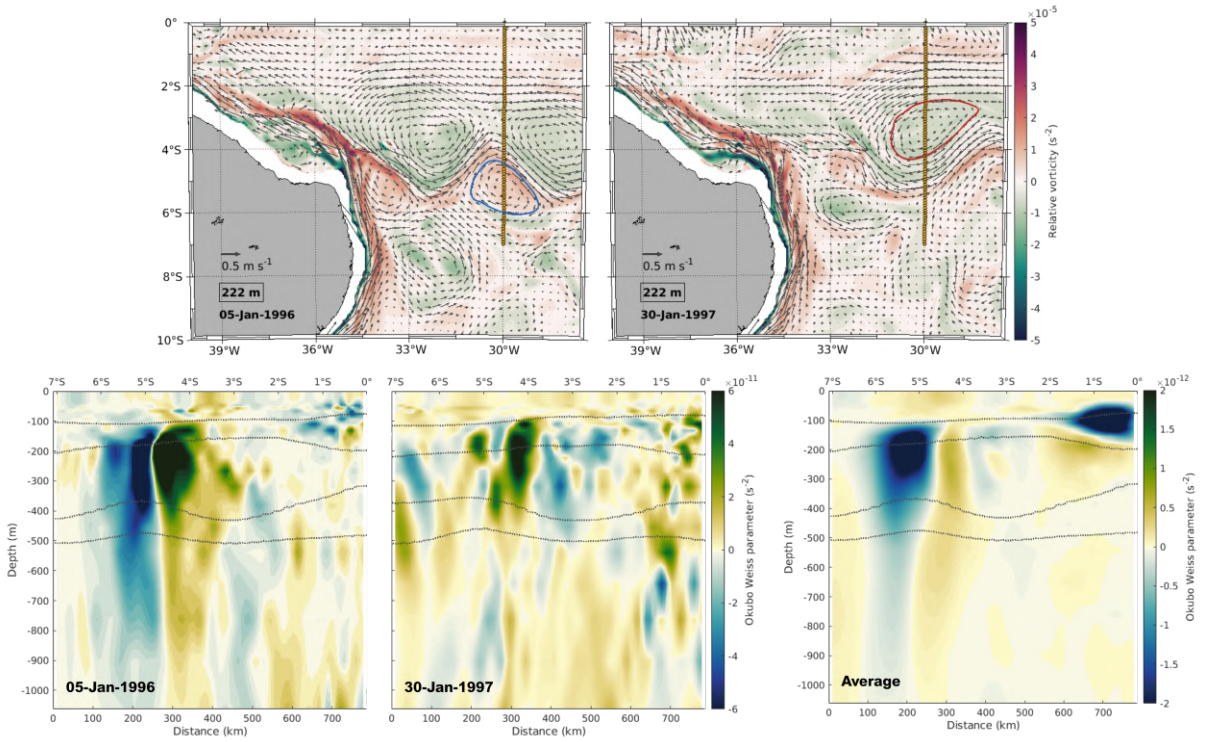

Figure 31 – Horizontal distribution of vorticity and velocity, with highlighted eddies passing through the section at 30°W on 05-Jan-1996 (upper-left pannel) and on 30-Jan-1997 (upper-right pannel). Cyclonic eddies are represented in blue and anticyclonic eddies are indicated in red. Vertical distribution of Okubo-Weiss parameter at the section on 05-Jan-1996 (lower-left pannel), on 30-Jan 1997 (lower-middle pannel) and the average distribution for the period of 1993-2018 (lower-right pannel). The ispycnals of are illustrated in gray dotted lines.

the vertical extension of cyclones and anticyclones is expected, consequence of the divergence and convergence property of these eddies, respectively. The positive patch at 4°-4.5°S is associated with the SEUC more typical position at 30°W. Note the negative OW values close to the equator, over the $\gamma_n = 26.7$ isopycnal and at the EUC location, which might be related to TIW propagating westward.

In Figure 32, a snapshot of a cyclonic circulation at 37°W was selected on 05-Jul-2001 to exemplify and characterize the eddies at the NBC band. The shedded NBUC eddy is mostly confined between the $\gamma_n = 24.5$ and $\gamma_n = 27.2$ isopycnals and approximately centered and the isopyncal of $\gamma_n = 26.7$, which correspond to the SEUC core level. The averaged vertical distribution at the 37°W section shows negative OW values enteending from bellow the $\gamma_n = 24.5$ isopycnal to over 900m depth. Stronger values are found at the surrounding of the $\gamma_n = 26.7$ isopycnal, above 400m depth and at 2.3°-3.4°S. The negative patch between 2.5°S and the equator is restricted to upper layers over the isopycnal of $\gamma_n = 26.7$. This negative OW values might be related in part to eddies extending northward, as observed in the NBUC eddy on 05-Jul-2001. However, it is also related to the negative patch equatorward also observed at 30°W, which is probably associated with TIW propagating westward as already mentioned.

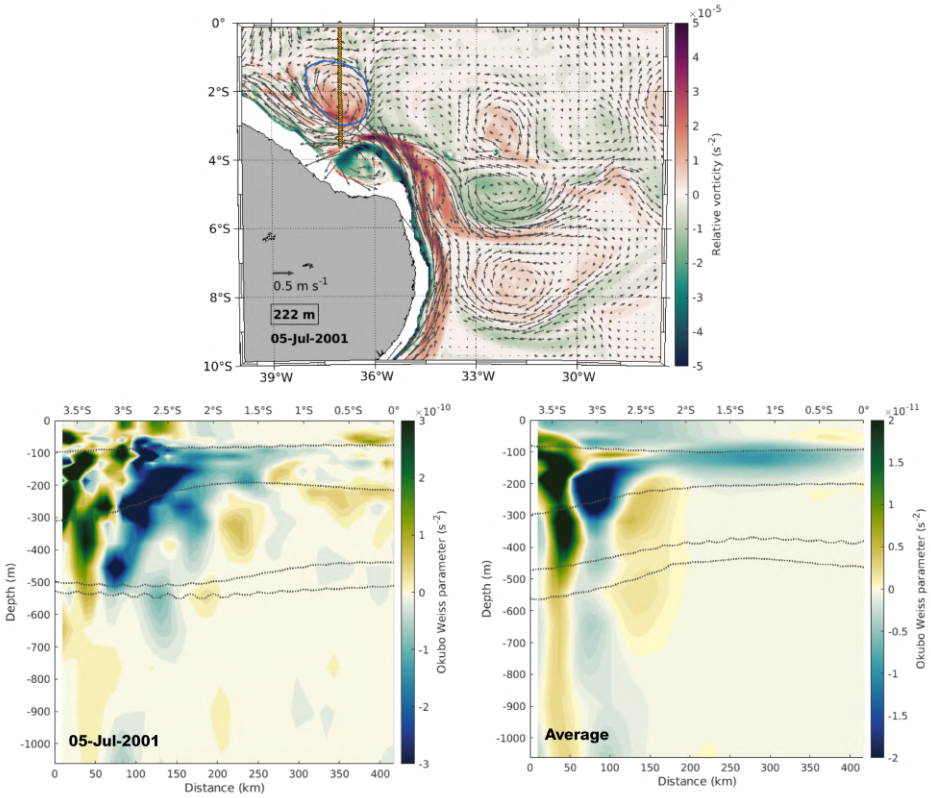

Figure 32 – Horizontal distribution of vorticity and velocity, with highlighted cyclonic eddy (blue circle) passing through the section at 37°W on 05-Jul-2001 (upper pannel). Vertical distribution of Okubo-Weiss parameter at the section on 05-Jul-2001 (lower-left pannel) and the average distribution for the period of 1993-2018 (lower-right pannel). The isopycnals of are illustrated as gray dotted lines.

4.3.3 Eddy formation rates

After characterizing the mesoscale features associated with the SEUC dynamics, we calculated the number of eddies formed per year and the probability of formation for each analyzed band. The probability of formation is the ratio between the number of eddies formed at a specific month and the total amount of eddies formed at the analyzed band.

The probability of formation allow us to identify the climatological variability for the formation of the mesoscale circulations at the bands of interest, calculated for the period of 1993-2018 (Figure 33). The cyclones at the cyclonic band show peaks of 8.1% at March, July and October, and minima of 4.5% in November and of 4.8% in February. At the anticyclonic band, the months of significant peaks for anticyclonic event are March and August of 8.6% and 8.0%, respectively. The lowest points are in October and November, with values of 5.8% in both months. The anticyclones formed at the cyclonic band seemed to reveal a seasonal variation, with higher probabilities between November and April and lower probabilities from May to October. No seasonal variability is observed for the cyclones at the anticyclonic band, with a single siginificant peak in August. For both cyclonic/anticyclonic bands, no clear

seasonal cycle is shown for the cyclones and anticyclones formed, recpetively. The SEUC eddies are, therefore, continuos throughout the year along the current southern and northern limits at its origin region. As already discussed in Chapter 3, the NBUC-SEUC connection was observed in spring and fall seasons (Figure 7). Moreover, it was also previously mentioned that the presence of a cyclonic circulation at the NBUC-SEUC limits around 5.5°S and 33.5°W might reinforce the connection between the currents. The formation of cyclonic structures propagating westward throughout the year at the cyclonic band corroborate to the inference of an year-round connection between the NBUC and the SEUC.

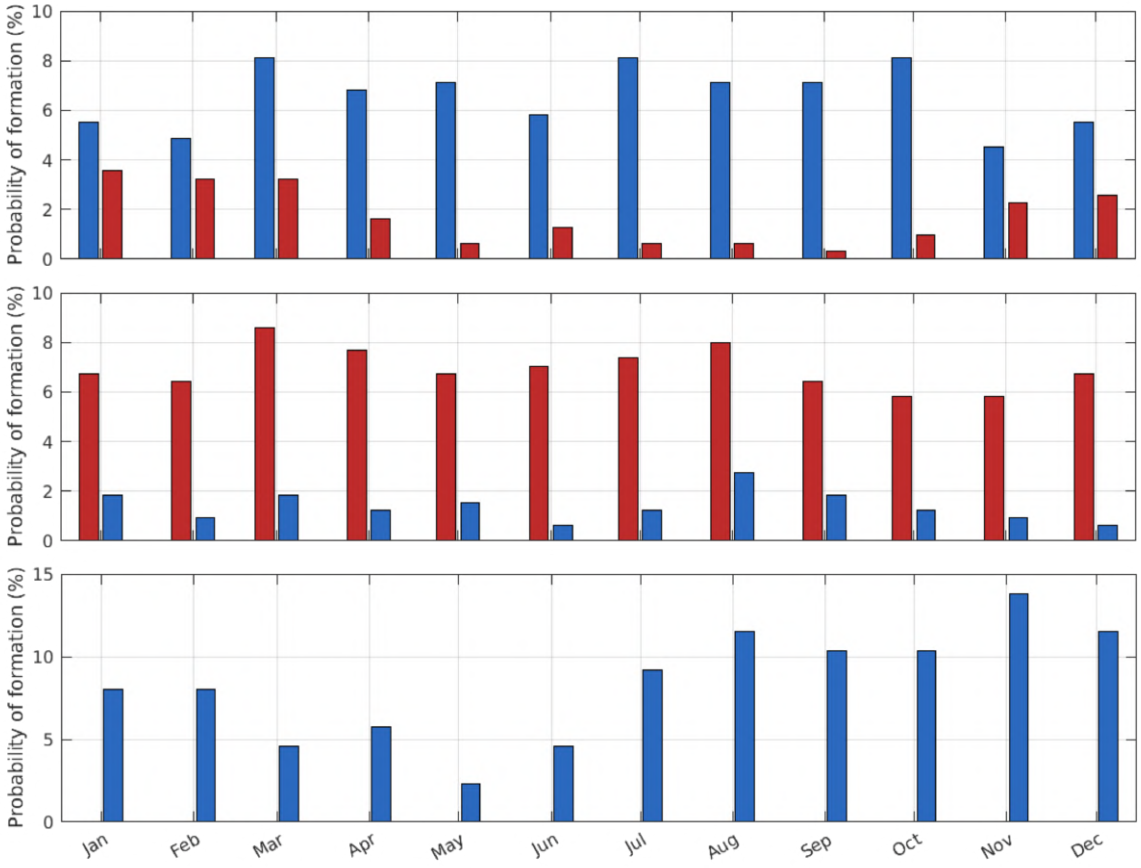

Figure 33 – Probability of formation in each month for the cyclonic band (upper panel), the anticyclonic band (middle panel) and the NBC band (lower panel). Anticyclonic eddies are indicated in red and cyclonic eddies are represented in blue.

The NBUC eddies reveal a seasonal cycle of higher probabilities of formation from June to December, and lower probabilities at the period between January and June. In May, the cyclonic events are the least likely to occur with value of 2.3%, and a small relative peak is observed in April. The seasonallity of the NBUC-eddies formation shows similarities with the climatological variability found in the EUC at 1°S (Figure 20). In fact, the current demonstrates higher velocities from August to December, minimum velocity in May and a small peak in April. The climatological SEUC at 30°W, presented in Figure 21, share a resembling seasonallity with the cycle found in the formation of the NBUC eddies. The current is shifted north from June

to December, it is wider between September and December, and it shifts south from January to June. This EUC-NBUC eddies-SEUC seasonal dynamic could be associated with changes on the location of the NBUC retroflection to feed the SEUC, also evidenced on the observational maps (Figure 7). These findings give insights about the dynamics behind the NBUC shedding of eddies northwestward through the NBC, along the Brazilian coast, involving the presence of the EUC and the SEUC meridional positioning.

Figure 34 shows the interannual variation of the number of eddies formed at the cyclonic, the anticyclonic and the NBC bands for the period of 1993 to 2018. An average of 12 eddies per year form at the cyclonic band and, considering only the cyclonic eddies, an average of 9 cyclone were formed. The years of 2003 and 2010 showed total minima of 6 (5 cyclonic) eddies and 4 (2 cyclonic) eddies, respectively. No anticyclones were formed in 1999. At the anticyclonic band, the total average was equivalent to 13 eddies per year and, accounting only the anticyclonic events, the average was of 10 eddies per year. In 2001, a peak of eddy events occured for the total amount, and also for the anticyclones and cyclones at this band, with a total maximum of 22 (15 anticyclonic) eddies. When comparing the cyclonic and anticyclonic bands, they revealed similar average number of eddy formed per year, with no significant difference. After the analysis of long snapshot series (not shown), we observed that the number of detected events for the NBC band was underestimated. Two main reasons seemed to interfere at the algorithm detection: some of the eddies were smaller and presented high deformation and ellipticity and others were embedded in the strong NBC, very close to the topographic limit along the Brazilian coast. Therefore, the algorithm possibly was not able to identify closed streamline contours for those eddies. Nevertheless, the NBC band presented an average of 3 eddies per year and, as already noted, no anticyclones were detected. Some years, such as 1996, 1997 and 1998, showed no eddy detection. Disconsidering the years of no eddy detection, the NBUC shedded an average of 4 eddies per year. In 2001 and 2002, 7 cyclones per year were observed at the NBC band.

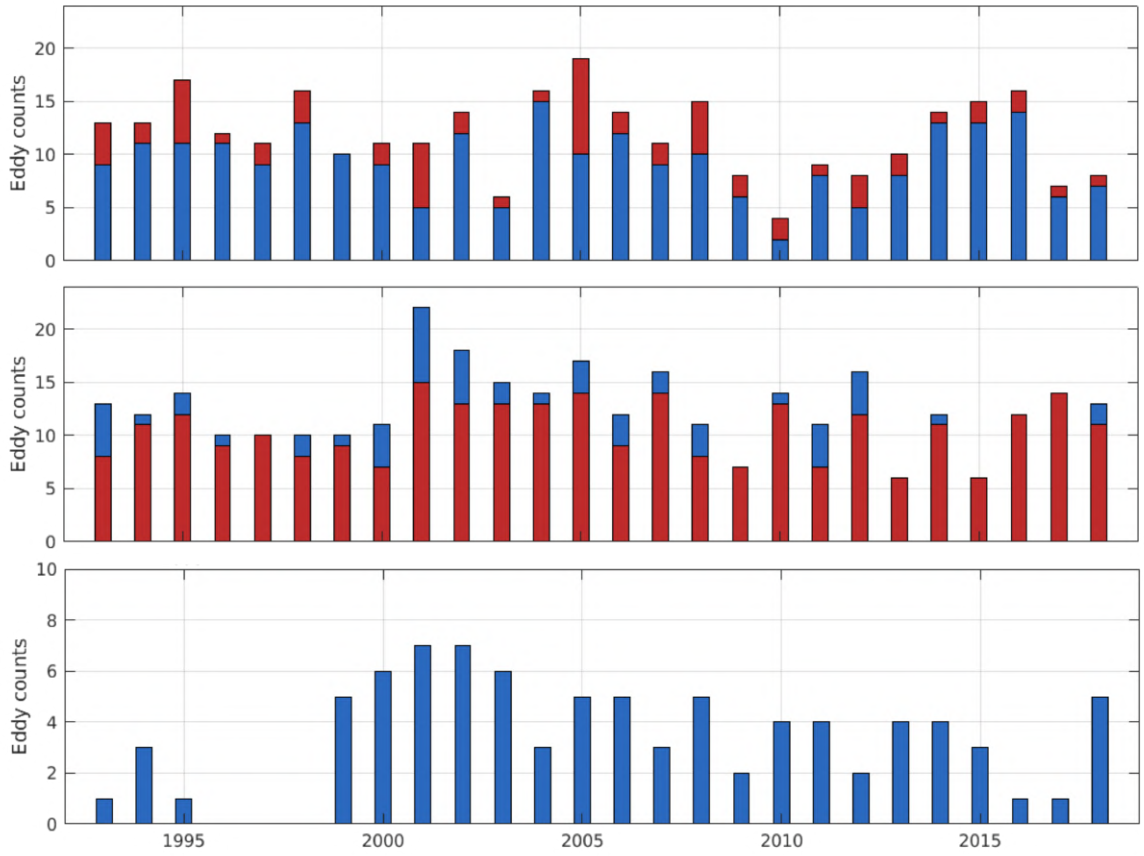

Figure 34 – Number of eddies per year (1993-2018) considering its formation time for the cyclonic band (upper panel), the anticyclonic band (middle panel), and the NBC band (lower panel). Anticyclonic eddies are indicated in red and cyclonic eddies are represented in blue.

5

SUMMARY AND CONCLUSIONS

The SEUC, the northermost equatorial countercurrent of the South Atlantic Ocean, is found flowing eastward in the latitude range between 3.5°-5,5°. The original studies to first described the jet pointed out it presents a velocity core at about 200 m depth. As the SEUC's velocity core depth is situated below the tropical pycnocline, it causes sometimes the SEUC to be referred in the literature as a subpycnoclinc current. The formation of the SEUC has been disputed among the scientific community. Some authors credit the SEUC genesis due to the feeding mainly by the western boudary current system, i.e., the NBUC. Others consider the SEUC to be formed by ocean interior contributers, such as a cyclonic turn of the equatorial SEC branch, as it impinges on the Brazilian continental shelf. Other works comprimise the two ideas aforementioned, stating both water volume sources are part of the SEUC formation, and that the relative contribution of either varies seasonally. However, some of these studies employed data of either a single or a pair of synopitic hydrographic surveys. Others employed a limited float data set at a restricted depth range only. Some older studies tried even to build a climatology based on geostrophic computation to obtain a picture of this near-equatorial scenario. The present work aims to proof (or disproof once for all) that there is a connection between the NBUC-NBC system and the SEUC formation nearby the South Atlantic western boundary.

In order to pursue the main objective of this thesis, we gathered 25 oceanographic campaigns from both national and international efforts to obtain various maps of the SEC origin site, as well the currents' vertical sections. This would allow us to the examine the morphometry and ispyocnal ranges related to the jets in the region. From those 25 surveys, after pre-processing and examining each one of them in terms of hydrography and vessel-mounted ADCP data, we selected 13 that were effectively employed in our analysis, calculations, and objective mapping.

Given that the 13 selected surveys spanned the area in all four seasons of the year, we identified the NBUC-SEUC connection from the horizontal velocity and streamfunction fields. The NBUC indeed retroflects and feeds the SEUC. The (cyclonic) retroflection lobes were captured being extended to different latitudes: 5.5°S, 4.5°S and 3.5°S. This connection

was also observed in fall and spring seasons, discarting a seasonal NBUC-SEUC connection, and reinforced the hypothesis of a year-round retroflection.

The ADCP-derived vertical sections enabled the identification of the vertical structure of the currents at the western Atlantic boundary. The NBUC flows northward along the Brazilian coast down to 800m depth, with core located around 200 m depth, reaching velocities over 1.0 m s^{-1}. East of the NBUC, the NBUCc southward flow was present, with a core around 300m depth. After the abrupt change in the coast direction, the NBC flows northwestward down to approximately 450 m depth, with double core at the surface and at subsurface around 170 m depth. North of 2°S and west of 36°W, the EUC flows eastward centered around $\gamma_n =$ 24.5 and reaching depths of 240m. The SEUC was observed as an eastward meandering flow, between $\gamma_n = 24.5$ and $\gamma_n = 27.2$ isopycnals, with core at $\gamma_n = 26.7$ around 220 m depth. Off the Brazilian coast, west of 34°W, the current reaches velocities of 0.6 m s^{-1} between 4°S and 5°S. Closer to the continetal margin, the SEUC was observed north of 5°S with maximum velocities of 0.4 m s^{-1}. The flow was present further north between 2.5°S and 4.2°S at 35°W, and west of 35°W it is not possible to clearly distinguish between the SEUC and the EUC. The calculated SEUC transports varied from 3.8 Sv to 11.7 Sv, with mean of 8.1 Sv and standard deviation of 2.0 Sv. No clear seasonal cycle was evident from observations, neither for the SEUC transport nor for the NBUC-NBC system. However, regarding the last affirmation, the reader should consider that the cruises were either unevenly distributed temporally and/or the possible mesoscale variability may overcome the seasonal signal on the cruises' quasi-synoptic snapshots.

Moreover, we opted to further address the NBUC-NBC connection to the SEUC by examining and exploring water mass tracers, specially regarding the dissolved oxygen and salinity contents. Most works in the region classify locally the SACW as coming from three different sources: the low saline and high O_2 SAW, the low saline and low O_2 EAW, and high saline and low O_2 NAW. The presence of high oxygen concentrations in the SEUC compared to the low concentrations in the eSEC is a strong indicative of a connection between the NBUC and the SEUC. These oxygen-enriched waters are present at pycnoclinic levels and they are still more evident at subpycnoclinic levels. Another source for these oxygen-enriched waters could be the deeper portions of the EUC. Moreover, the occurrence of low dissolved oxygen characteristics in the NBUC-NBC system suggests recirculations from the SEUC to the system.

Unfortunately, despite the vast amount of hidrographic-survey data gathered for this work, it was clear to us that the spatial and time resolutions of the available *in situ* measurements were not enough to analyze in detail the variability of the NBUC-SEUC connection, neither to examine the mesosacale activity along the SEUC flow. In that context, as we opted to analyse validaded numerical modeling outputs appear as a useful tool to proceed with our investigation: the GLORYS12V1 reanalysis. We then were able to examine a three-dimensional time series of the portion of the Tropical Atlantic western boundary comprising the SEC formation site.

As there were no validation of the GLORYS12V1 reanalysis available for the study area, we carried out a as careful as possible validation by means of radar (or spiderweb) charts and Taylor diagrams. These statistical tools were built confronting the quasi-synoptic vertical sections and horizontal maps from the cruises and the model output in the same time range. Since the GLORYS12V1 is data-assimilative, the output can be directly compared. In the case of radar charts, we used the velocity components, the velocity magnitude, the latitude, longitude, depth and neutral isopycnal surface of the current core position as qualifiers (or contributors). The overall correlation coefficient exceeded 0.75 for most qualifiers in the comparisons between model and vertical sections. The Taylor diagram presented general correlation coefficient varying from 0.4 to 0.9, all statistically significant at the 95% confidence level. This effective numerical model output validation allowed us the development of a more confident and robust analysis.

We first built a mean climatological scenario for the 1993-2018 time series, as well as climatological seasonaly-varying hovmöller diagrams enabled the analysis of the seasonal current for the four boundaries closing the study area between 0°-6°S in latitude and 38.5°W-30°W in longitude. The volume tranport imbalance of 0.86 Sv in the rectangular region limited vertical by the 24.5-27.2 neutral isopycnals (100-500 m depth on average) was considereed small, since represented only about 3% of the NBUC transport and about 10% of the SEUC transport. The calculation revealed unequivocally the feeding of the SEUC by the NBUC. It is not discarded the eventual contributions of the EUC amd eSEC flows to the SEUC. However, between 1-2 Sv must retroflect from the NBUC to feed the SEUC.

The seasonaly-varying homöller diagrams also indicate a spatially-damped oscillatory pattern to the SEUC in southern border of the rectangular area. Since we averaged over 25 years of numerical simulation, we conclude that there is a mean retroflection pattern reminiscent from a vigorous separation of the pycnoclinc-subpycnoclinc NBUC to form the SEUC.

A complete picture of the GLORYS12V1 emerges when we present below in Figure 35 the 1993-2018 mean volume transport stream function, where the retroflection pattern is evident. The retroflection lobe is cyclonic while the primary crest is anticyclonic.

We also built a SEUC transport time series which interestingly indicates an increase of about .5 Sv/year in our a series, a value which virtually matches the supposed weakening of the AMOC in the northern hemisphere. Of course, we would be tempted to affirm that the AMOC weakens due to detours of pycnoclinic branches due to equatorial circulation. Of course, more extensive studies involving the other Atlantic countercurrents in both northern and southern halves of the equatorial gyre should be conduct to confirm this so far only subtle evidence.

We continued our SEUC investigation using the GLORY12V1 outputs addressing the mesoscale variability. We employed the AMEDA eddy detecting algorithm and evaluated the study area as very rich eddy region but marked bands, which are dominanted by diferent polarities. For instance, three bands were clearly identified. The northeast anticyclonic band

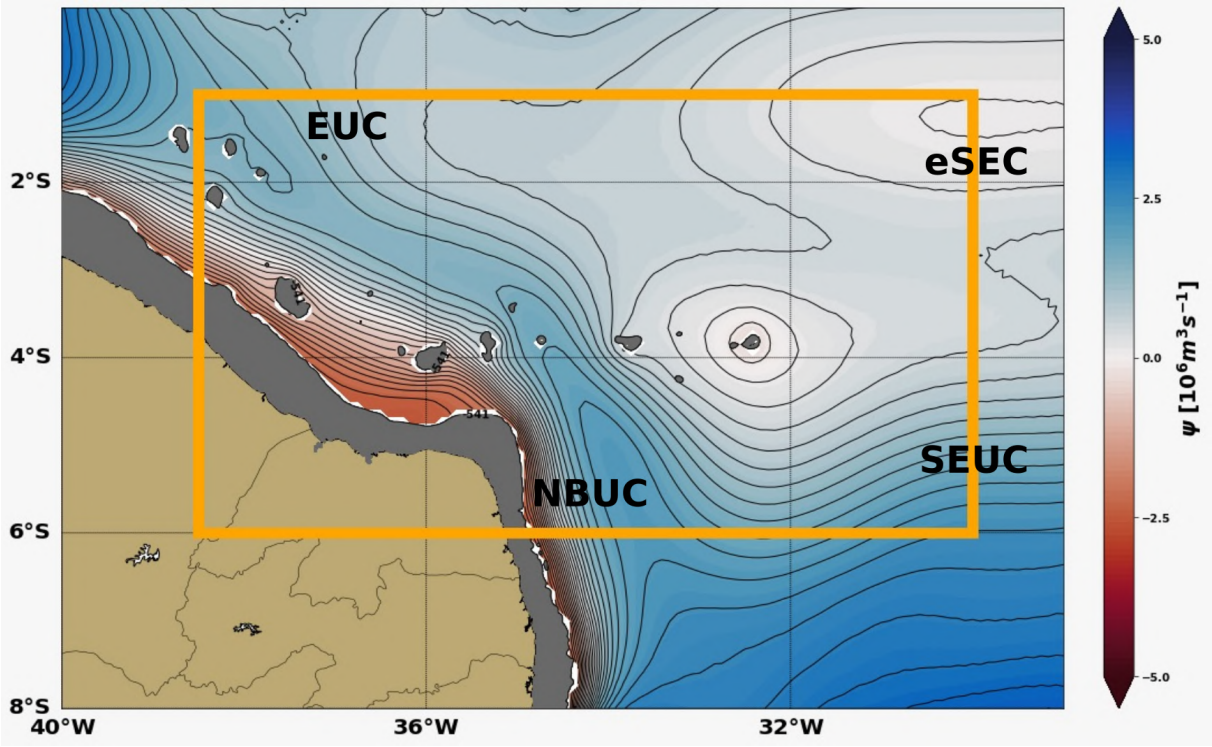

Figure 35 – The 1993-2018, $\gamma_n = 24.7 - 27.2$ mean transport stream function for the GLORYS12V1 simulation. Each streamline represents 1 Sv. The orange box delimits the borders of the rectangle used to compute the volume transport balance.

centered in 3.5°S, and extending from 34°W-28°; the southeast cyclonic band centered at 5.5°S and also extending from 34°W-28°; and the western boundary (or the NBC) cyclonic band centered at 2.5°S, and spanning from 38.5°W-34.4°. We conclude that the NE anticyclonic and SE cyclonic bands are associated with finite amplitude meanders associated with the very likely unstable SEUC meanders adjacent to the NBUC retroflection. As a matter of fact, it has been reported in the literature that TIWs are formed nearby the western boundary and propagate group eastward, as most of the Yanai-like waves do. This certainly corroborates our findings, where our results suggests waves of about 360-400 km emanting from the NBUC retroflection. These waves can be either short baroclinic Rossby waves or short Yanai waves.

However, perhaps the most unexpected result we obtained when analyzing the outputs of the GLORYS12V1 reanalysis was to verify that the NBUC retroflection to form the SEUC is a very dynamic region, from where vortical rings are shed, very much as its counterparts on the northern hemisphere at 4°N and 7°N. We again present a synthesis figure exemplfying the retroflection lobe instabilization, elongation, and its necking-off forming a intrapycnoclinic cyclone (Figure 36). According to the AMEDA analysis result, the expressive average amount of 7 rings per year are generated from the NBUC retroflection upon using the $approx$ 25 years of simulation. The strong eddy signal depicted in the northwest corner of the mean transport stream function map suggests that these rings propagate and tend to converge in the region where the upper pycnocline waters of the NBC retroflect that the equator to feed the EUC.

This is however beyond the scope of this work, and we leave it as a suggestion of future studies in the region.

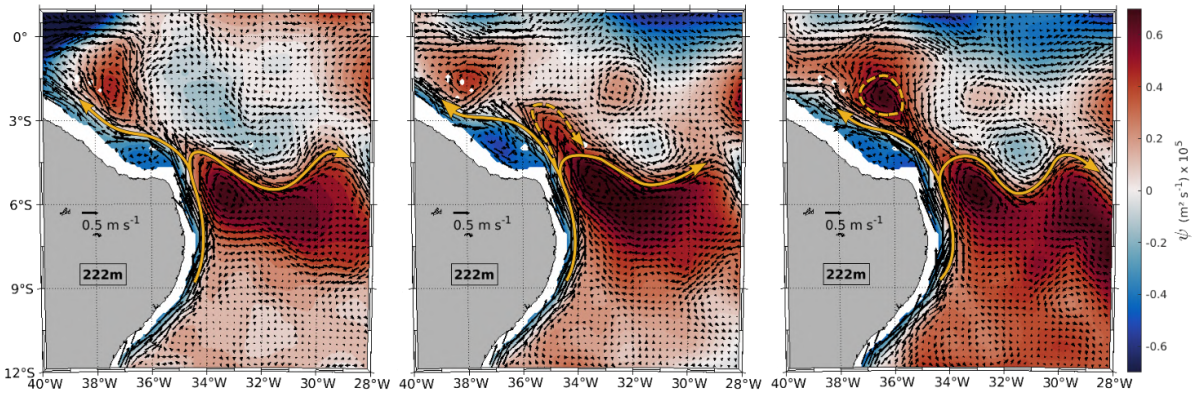

Figure 36 – The cyclone shedding by the NBUC retroflection off Cape Calcanhar. The ring separates and flows northward along the western boundary bordering the NBC. Snapshots selected from the simulation year of 2003.

To end this thesis, it deserves emphasis to state that the three hypotheses listed in Section 1 upon the formulation of the current research were fully addressed and tested. They were all confirmed with the results summarized and reviewed in this last chapter.

REFERENCES

ALLEN, J. R. Models of wind-driven currents on the continental shelf. *Annual Review of Fluid Mechanics*, v. 12, n. 1, p. 389–433, 1980.

ARAUJO, M. et al. Brazilian pirata cruises: S-adcp data. *SEANOE*, 2021.

ARAUJO, M. E.; RAMALHO, C. W. N.; MELO, P. W. Artisanal fishers, consumers and the environment: immediate consequences of the oil spill in pernambuco, northeast brazil. *Cadernos de Saúde Pública*, v. 36, n. 1, 2020.

ARHAN, M. et al. Hydrographic sections across the atlantic at 7°30n and 4°30s. *Deep Sea Research Part I*, v. 45, p. 829—872, 1998.

BERTRAND, A. et al. Abracos 2 cruise - physical datasets. *SEANOE*, 2017.

BERTRAND, A. et al. Abracos cruise - physical datasets. *SEANOE*, 2015.

BOEBEL, O. et al. The intermediate depth circulation of the western south atlantic. *Geophysical Research Letters*, v. 26, n. 21, p. 3329–3332, 1999.

BOURLES, B. et al. Pirata: A sustained observing system for tropical atlantic climate research and forecasting. *Earth and Space Science*, 2019.

BOURLES, B. et al. On the evolution of the thermocline and subthermocline eastward currents in the equatorial atlantic. *Geophysical Research Letters*, v. 29, n. 16, 2002.

BOURLES, B.; GOURIOU, Y.; CHUCHLA, R. On the circulation in the upper layer of the western equatorial atlantic. *Journal of Geophysical Research*, v. 104, n. C9, p. 151—170, 1999.

BOURLES, B. et al. Upper layer currents in the western tropical north atlantic (1989-1991). *Journal of Geophysical Research*, v. 104, n. C1, p. 1361—1375, 1999.

BOYER, T. P. et al. World ocean database 2018. 2018. NOAA Atlas NESDIS 87. Disponível em: <https://www.ncei.noaa.gov/sites/default/files/2020-04/wod_intro_0.pdf>.

BRANDT, P. et al. On the role of circulation and mixing in the ventilation of oxygenminimum zones with a focus on the eastern tropical north atlantic. *Biogeosciences*, v. 12, p. 489—-512, 2015.

BRANDT, P. et al. The equatorial undercurrent in the central atlantic and its relation to tropical atlantic variability. *Climate Dynamics*, v. 43, n. 11, 2014.

BRANDT, P. et al. Atlantic equatorial undercurrent intensification counteracts warming-induced deoxygenation. *Nature Geoscience*, v. 14, n. 5, p. 278–282, 2017.

BRANDT, P. et al. Changes in the ventilation of the oxygen minimum zone of the tropical north atlantic. *Journal of Physical Oceanography*, v. 40, p. 1784—-1801, 2010.

BRANDT, P. et al. Circulation in the central equatorial atlantic: Mean and intraseasonal to seasonal variability. *Geophysical Research Letters*, v. 33, n. L07609, 2006.

BUNGE, L.; PROVOST, C.; KARTAVTSEFF, A. Variability in horizontal current velocities in the central and eastern equatorial atlantic in 2002. *Journal of Geophysical Research: Atmospheres*, v. 112, n. C2, 2007.

CABANES, C. et al. The cora dataset: Validation and diagnostics of in-situ ocean temperature and salinity measurements. *Drakkar Group Experiment report*, 2013.

CARTER, E. F.; ROBINSON, A. R. Analysis models for the estimation of oceanic fields. *Journal of Atmospheric and Oceanic Technology*, v. 4, n. 1, p. 49–74, 1987.

CHAIGNEAU, A.; GIZOLME, A.; GRADOS, C. Mesoscale eddies off peru in altimeter records: Identification algorithms and eddy spatio-temporal patterns. *Progress in Oceanography*, v. 79, p. 106–119, 2008.

CHELTON, D. B. et al. Geographical variability of the first baroclinic rossby radius of deformation. *Journal of Physical Oceanography*, v. 28, n. 3, p. 433–460, 2006.

COCHRANE, J. D.; KELLY, F. J.; OLLING, C. R. Subthermocline countercurrents in the western equatorial atlantic ocean. *Journal of Physical Oceanography*, v. 9, p. 724–738, 1979.

COP11, UN. Decisions. In: UNITED NATIONS. *Fourteenth meeting of the Conference of the Parties to the Convention on Biological Diversity*. [S.l.], 2012. (Conference of the Parties).

DECCO, H. T. et al. Revisiting tropical instability wave variability in the atlantic ocean using soda reanalysis. *Ocean Dynamics*, v. 68, n. 15, 2018.

DENGLER, M. et al. Break-up of the atlantic deep western boundary current into eddies at 8° s. *Nature*, v. 432, p. 1018–1020, 2004.

DOGLIOLI, A. M. et al. Tracking coherent structures in a regional ocean model with wavelet analysis: Application to cape basin eddies. *Journal of Geophysical Research*, v. 112, n. C05043, 2007.

DOSSA, A. *Near-surface ocean dynamic off Northeast Brazil and coastal sea surface salinity gradients in the world ocean*. Tese (Doutorado) — Federal University of Pernambuco, Recife, Brazil, May 2021. PhD thesis.

DREVILLON, M. et al. CMEMS-MOB-QUID-015-012, E.U. Copernicus Marine Service Information. 2021. Accessed: June 2021. Disponível em: <https://catalogue.marine.copernicus.eu/documents/QUID/CMEMS-GLO-QUID-001-030.pdf>.

DUCHEZ, A. et al. Drivers of exceptionally cold north atlantic ocean temperatures and their link to the 2015 european heat wave. *Environmental Research Letters*, v. 11, n. 7, 2016.

DUEING, W. et al. Meanders and long waves in the equatorial atlantic. *Nature*, v. 257, p. 280—284, 1975.

DURACK, P.; WIJFFELS, S. Fifty-year trends in global ocean salinities and their relationship to broadscale warming. *Journal of Climate*, v. 23, n. 16, p. 4342–4362, 2010.

DUTEIL, O. et al. Major role of the equatorial current system in setting oxygen levels in the eastern tropical atlantic ocean: A high-resolution model study. *Geophysical Research Letters*, v. 41, p. 2033—2040, 2014.

EMERY, W. J.; THOMSON, R. E. *Data analysis methods in physical oceanography*. 3. ed. [S.l.]: Elsevier Science, 2014.

FAKOWSKI, P. G. et al. Role of eddy pumping in enhancing primary production in the ocean. *Nature*, v. 352, n. 6330, p. 55–58, 1991.

FERRARI, R.; FERREIRA, D. What processes drive the ocean heat transport? *Ocean Modelling*, v. 38, p. 171–186, 2011.

FISCHER, J. et al. South equatorial undercurrent in the western to central tropical atlantic. *Geophysical Research Letters*, v. 35, n. L21601, 2008.

FLIERL, G. R. Particle motions in large-amplitude wave fields. *Geophysical Astrophysical Fluid Dynamics*, v. 18, n. 1–2, p. 39–74, 1981.

FOLTZ, G. R.; MCPHADEN, M. J. The 30–70 day oscillations in the tropical atlantic. *Geophysical Research Letters*, v. 31, n. 15, 2004.

FRATANTONI, D. M.; RICHARDSON, P. The evolution and demise of north brazil current rings. *Journal of Physical Oceanography*, v. 36, n. 7, 2006.

GARCIA, H. E. et al. World ocean database 2018: User manual. 2018. NOAA Atlas NESDIS 87. Disponível em: <https://www.ncei.noaa.gov/sites/default/files/2020-04/wodreadme_0.pdf>.

GODO, O. R. et al. Mesoscale eddies are oases for higher trophic marine life. *PLoS ONE*, v. 7, n. 1, 2012.

GOES, M. et al. Variability of the atlantic off-equatorial eastward currents during 1993—2010 using a synthetic method. *Journal of Geophysical Research*, v. 118, p. 3026—3045, 2013.

GOES, M.; SILVEIRA, I. C. A.; WAINER, I. Retroflections of the north brazil current during february 2002. *Deep-Sea Research Part I: Oceanographic Research Papers*, v. 52, n. 4, p. 647–667, 2005.

GONCALVES, L. L. et al. The brazilian blue amazon under threat: Why has the oil spill continued for so long? *Ambiente Sociedade*, v. 23, n. 1, 2020.

GOOD, S.; MARTIN, M.; RAYNER, N. En4: Quality controlled ocean temperature and salinity profiles and monthly objective analyses with uncertainty estimates. *Journal of Geophysical Research: Oceans*, v. 118, n. 12, 2013.

GREINER, E. et al. CMEMS-MOB-QUID-015-012, E.U. Copernicus Marine Service Information. 2020. Accessed: May 2021. Disponível em: <https://catalogue.marine.copernicus.eu/documents/QUID/CMEMS-MOB-QUID-015-012.pdf>.

HAN, W. et al. Dynamics of intraseasonal sea level and thermocline variability in the equatorial atlantic during 2002–03. *Journal of Physical Oceanography*, v. 38, n. 5, p. 945—967, 2008.

HUA, B. L.; MARIN, F.; SCHOPP, R. Three-dimensional dynamics of the subsurface countercurrents and equatorial thermostad. part i: Formulation of the problem and generic properties. *Journal of Physical Oceanography*, v. 33, n. 12, p. 2588–2609, 2003.

HUMMELS, R. et al. Interannual to decadal changes in the western boundary circulation in the atlantic at 11°s. *Geophysical Research Letters*, v. 42, p. 7615—-7622, 2015.

HUTTL-KABUS, S.; BONING, C. W. Pathways and variability of the off-equatorial undercurrents in the atlantic ocean. *Journal of Geophysical Research*, v. 113, n. C10018, 2008.

IPCC. Climate change 2021: The physical science basis. contribution of working group i to the sixth assessment report of the intergovernmental panel on climate change. *Cambridge University Press.*, 2021.

JOCHUM, M.; MALANOTTE-RIZZOLI, P. A new theory for the generation of the equatorial subsurface countercurrents. *Journal of Physical Oceanography*, v. 34, p. 755–771, 2004.

JOCHUM, M.; MALANOTTE-RIZZOLI, P.; BUSALACCHI, A. Tropical instability waves in the atlantic ocean. *Ocean Modelling*, v. 7, p. 145–163, 2004.

JOHNS, W. E. et al. Annual cycle and variability of the north brazil current. *Journal of Physical Oceanography*, v. 28, n. 1, p. 103—128, 1998.

JOHNSON, G. C.; MOORE, D. W. The pacific subsurface countercurrents and an inertial model. *Journal of Physical Oceanography*, v. 27, n. 11, p. 2448–2459, 1997.

KATZ, E. J. Equatorial kelvin waves in the atlantic. *Journal of Geophysical Research: Atmospheres*, v. 92, n. C2, p. 1894–1898, 1987.

KEELING, R. E.; ARNE, K.; GRUBER, N. Ocean deoxygenation in a warming world. *Annual Review of Marine Science*, v. 2, n. 1, p. 199—-229, 2010.

KERMABON, C. et al. Chaine automatisée de suivi des courantomètres acoustiques doppler embarqués. cascade v7.2: Logiciel de validation et de visualisation des mesures adcp de coque. documentation utilisateur et maintenance. *Ifremer, Brest, France*, n. 115 pp., 2018. Disponível em: <ftp://ftp.ifremer.fr/ifremer/lpo_permanents/cascade/CASCADE_V72_V2.pdf>.

KRELLING, A. P. M. et al. A newly observed quasi-stationary subsurface anticyclone of the north brazil undercurrent at 4°s: the potiguar eddy. *Journal of Geophysical Research: Oceans*, v. 125, n. e2020JC016268, 2020.

LADLE, R. J. et al. Brazil's mystery oil spill: an ongoing social disaster. *Nature*, v. 578, n. 7793, p. 37–37, 2020.

Le Vu, B.; STEGNER, A.; ARSOUZE, T. Angular momentum eddy detection and tracking algorithm (ameda) and its application to coastal eddy formation. *Journal of Atmospheric and Oceanic Technology*, v. 35, n. 4, p. 739–762, 2018.

LI, Z.; CHAO, Y.; MCWILLIAMS, J. C. Computation of the streamfunction and velocity potential for limited and irregular domains. *Monthly weather review*, v. 134, n. 11, p. 3384–3394, 2006.

LIU, W. et al. Overlooked possibility of a collapsed atlantic meridional overturning circulation in warming climate. *Science Advances*, v. 3, n. 1, 2017.

LORBACHER, K. et al. Regional patterns of sea level change related to interannual variability and multidecadal trends in the atlantic meridional overturning circulation. *Journal of Climate*, v. 23, n. 15, p. 4243–4254, 2010.

LUKO, C. D. et al. Revisiting the atlantic south equatorial current. *Journal of Geophysical Research: Oceans*, 2021.

LUMPKIN, R.; GARZOLI, S. Interannual to decadal variability in the southwestern atlantic's surface circulation. *Journal of Geophysical Research Atmospheres*, v. 116, n. C1, 2011.

LUMPKIN, R.; GARZOLI, S. L. Near-surface circulation in the tropical atlantic ocean. *Deep-Sea Research Part I*, v. 52, p. 495—-518, 2005.

LUMPKIN, R.; SPEER, K. Global ocean meridional overturning. *Journal of Physical Oceanography*, v. 37, n. 10, 2007.

LUO, J. et al. Ocean heat content reveals secrets of fish migrations. *PLoS ONE*, v. 10, n. 10, 2015.

MADEC, G.; TEAM, N. S. *NEMO ocean engine*. [S.l.], 2008. (Scientific Notes of Climate Modelling Center, 27).

MAIDA, M. et al. Ensaio sobre a caracterização ecossistêmica, circulação das correntes e a exploração de petróleo nos montes submarinos da cadeia de fernando de noronha. *Relatório de Análise de Impacto Ambiental*, 2021.

MARIN, F.; HUA, B. L.; WACONGNE, S. The equatorial thermostad and subsurface countercurrents in the light of the dynamics of atmospheric hadley cells. *Journal of Marine Research*, v. 58, n. 3, p. 405–437, 2000.

MAYER, D. A.; WEISBERG, R. A description of coads surface meteorological fields and the implied sverdrup transports for the atlantic ocean from 30°s to 60°n. *Journal of Physical Oceanography*, v. 23, n. 10, 1993.

MCCREARY, J. P.; LU, P.; YU, Z. Dynamics of the pacific subsurface countercurrents. *Journal of Physical Oceanography*, v. 32, n. 8, p. 2379–2404, 2002.

MCGILLICUDDY, D. J. Mechanisms of physical-biological-biogeochemical interaction at the oceanic mesoscale. *Annual Review of Marine Science*, v. 8, n. 1, 2015.

MCPHADEN, M. On the dynamics of equatorial subsurface countercurrents. *Journal of Physical Oceanography*, v. 14, n. 7, p. 1216–1225, 1984.

MCWILLIAMS, J. C. The vortices of two-dimensional turbulence. *Journal of Fluid Mechanics*, v. 219, p. 361–385, 1990.

MENESGUEN, C. et al. Observations and mechanisms for the formation of deep equatorial and tropical circulation. *Earth and Space Science*, v. 6, p. 370–386, 2019.

Mercator Ocean. Global Ocean Physics Reanalysis, E.U. Copernicus Marine Service Information. 2020. Accessed: October 2020. Disponível em: <https://resources.marine.copernicus.eu/?option=com_csw&view=details&product_id=GLOBAL_REANALYSIS_PHY_001_030>.

MKHININI, N. et al. Long-lived mesoscale eddies in the eastern mediterranean sea: Analysis of 20 years of aviso geostrophic velocities. *Journal of Geophysical Research Oceans*, v. 119, p. 8603–8626, 2014.

MOLINARI, R. L. Observations of eastward currents in the tropical south atlantic ocean: 1978–1980. *Journal of Geophysical Research: Atmospheres*, v. 87, n. C12, p. 9707–9714, 1982.

MOLINES, J. M. et al. Orca12.l46 climatological and interannual simulations forced with dfs4.4: Gjm02 and mjm88. *Drakkar Group Experiment report*, 2014.

Multi Observations Thematic Assembly Center. Multi Observation Global Ocean 3D Temperature Salinity Heights Geostrophic Currents and MLD Product, E.U. Copernicus Marine Service Information. 2020. Accessed: May 2021. Disponível em: <https://resources.marine.copernicus.eu/?option=com_csw&view=details&product_id=MULTIOBS_GLO_PHY_TSUV_3D_MYNRT_015_012>.

NENCIOLI, F. et al. A vector geometry–based eddy detection algorithm and its application to a high-resolution numerical model product and high-frequency radar surface velocities in the southern california bight. *Journal of Atmospheric and Oceanic Technology*, v. 27, n. 3, p. 564–579, 2010.

OKUBO, A. Horizontal dispersion of floatable particles in the vicinity of velocity singularities such as convergences. *Deep Sea Research and Oceanographic*, v. 17, n. 3, p. 445–454, 1970.

PEREZ, F. F. et al. Atlantic ocean co2 uptake reduced by weakening of the meridional overturning circulation. *Nature Geoscience*, v. 6, n. 2, p. 146–152, 2013.

PETERSON, R. G.; STRAMMA, L. Upper-level circulation in the south atlantic ocean. *Progress in Oceanography*, v. 26, n. 1, p. 1–73, 1991.

PHILANDER, S. G. Instabilities of zonal equatorial currents. *Journal of Geophysical Research: Atmospheres*, v. 81, n. C7, p. 3725–3735, 1976.

RAHMSTORF, S. et al. Exceptional twentieth-century slowdown in atlantic ocean overturning circulation. *Nature Climate Change*, v. 5, n. 5, 2015.

REID, J. L. On the total geostrophic circulation of the south atlantic ocean: Flow patterns, tracers, and transports. *Progress in Oceanography*, v. 23, n. 3, p. 149–244, 1989.

RICHARDSON, P. L. et al. Norht brazil current retroflection eddies. *Journal of Geophysical Research*, v. 99, n. C3, p. 5081—5093, 1994.

RODRIGUES, R. R.; ROTHSTEIN, L. M.; WIMBUSH, M. Seasonal variability of the south equatorial current bifurcation in the atlantic ocean: a numerical study. *Journal of Physical Oceanography*, v. 37, n. 1, p. 16–30, 2007.

RUHS, S. et al. On the suitability of north brazil current transport estimates for monitoring basin-scale amoc changes. *Geophysical Research Letters*, v. 42, n. 19, p. 8072–8080, 2015.

SADARJOEN, I. A.; POST, F. H. Detection, quantification, and tracking of vortices using streamline geometry. *Computer Graphics*, v. 24, n. 3, p. 333–341, 2000.

SAMADI, S. et al. Seamount endemism questioned by the geographic distribution and population genetic structure of marine invertebrates. *Marine Biology*, v. 149, n. 6, p. 1463–1475, 2006.

SANCHEZ-VELASCO, L. et al. Three-dimensional distribution of fish larvae in a cyclonic eddy in the gulf of california during the summer. *Deep Sea Research Part I: Oceanographic Research Papers*, v. 75, p. 39–51, 2013.

SCBD. *Ecologically or Biologically Significant Marine Areas (EBSAs): Special places in the world's oceans*. 2014. 86 p.

SCHMIDT, R.; SCHMINCKE, H. U. Encyclopedia of volcanoes. In: _____. [S.l.]: ed. Academic Press, 2000. cap. Seamounts and island building, p. 383–402.

SCHOTT, F. et al. The zonal currents and transports at 35°w in the tropical atlantic. *Geophysical Research Letters*, v. 30, n. 7, 2003.

SCHOTT, F. et al. The shallow and deep western boundary circulation of the south atlantic at 5°–11°s. *Journal of Physical Oceanography*, v. 35, n. 11, p. 2031—2053, 2005.

SCHOTT, F.; FISCHER, J.; STRAMMA, L. Transports and pathways of the upper-layer circulation in the western tropical atlantic. *Journal of Physical Oceanography*, v. 28, p. 1904—-1927, 1998.

SCHOTT, F. A. et al. On the boundary flow off brazil at 5–10°s and its connection to the interior tropical atlantic. *Geophysical Research Letters*, v. 29, n. 17, p. 1–4, 2002.

SCHUCKMANN, K. von. *Intraseasonal variability in the southwestern and central tropical Atlantic Ocean*. Tese (Doutorado) — University of Kiel, Kiel, Germany, Sep 2006. PhD thesis.

SCHUCKMANN, K. von; BRANDT, P.; EDEN, C. Generation of tropical instability waves in the atlantic ocean. *Journal of Geophysical Research*, v. 113, n. C08034, 2008.

SERVAIN, J. et al. A pilot research moored array in the tropical atlantic (pirata). *Bulletin of the American Meteorological Society*, v. 79, p. 2019–2031, 1998.

SHMITZ, W. J.; MCCARTNEY, M. On the north atlantic circulation. *Reviews of Geophysics*, v. 31, n. 1, p. 29–49, 1993.

SHULZITSKI, K. et al. Encounter with mesoscale eddies enhances survival to settlement in larval coral reef fishes. *Proceedings of the National Academy of Sciences*, v. 113, n. 25, 2016.

SILVA, A. et al. Surface circulation and vertical structure of upper ocean variability around fernando de noronha archipelago and rocas atoll during spring 2015 and fall 2017. *Frontiers in Marine Science*, v. 8, n. 598101, 2021.

SILVA, M. A. et al. High-resolution regional ocean dynamics simulation in the southwestern tropical atlantic. *Ocean Modelling*, v. 30, n. 4, p. 76–116, 2009.

SILVEIRA, I. C. A.; BROWN, W. S.; FLIERL, G. R. Dynamics of the north brazil current retroflection region from the western tropical atlantic experiment observations. *Journal of Geophysical Research*, v. 105, n. C12, p. 559—583, 2000.

SILVEIRA, I. C. A.; MIRANDA, L. B.; BROWN, W. S. On the origins of the north brazil current. *Journal of Geophysical Research*, v. 99, n. C11, p. 501–512, 1994.

SILVEIRA, I. C. A.; NAPOLITANO, D. C.; FARIAS, I. U. Water masses and oceanic circulation of the brazilian continental margin and adjacent abyssal plain. In: _____. [S.l.]: Springer Nature Switzerland AG, 2020. cap. 2.

SILVEIRA, I. D. et al. On the baroclinic structure of the brazil current–intermediate western boundary current system at 22–23 s. *Geophysical research letters*, Wiley Online Library, v. 31, n. 14, 2004.

SIMOES-SOUZA, I. et al. The barreirinhas eddies: stable energetic anticyclones in the near-equatorial south atlantic. *Frontiers in Marine Science*, v. 8, n. 617011, 2021.

SNOWDEN, D. P.; MOLINARI, R. L. Subtropical cells in the atlantic ocean: An observational summary. *Elsevier Oceanography Series*, v. 68, p. 287–312, 2003.

SPECHT, M. S.; JUNGCLAUS, J.; BADER, J. Subsurface tropical instability waves in the atlantic ocean in model and observations. In: *EGU General Assembly 2021*. online: [s.n.], 2021. (EGU21-53).

SROKOSZ, M. A.; BRYDEN, H. L. Observing the atlantic meridional overturning circulation yields a decade of inevitable surprises. *Science*, v. 348, n. 6241, 2017.

STRAMMA, L. Geostrophic transport of the south equatorial current in the atlantic. *Journal of Marine Research*, v. 49, n. 2, p. 281–294, 1991.

STRAMMA, L.; ENGLAND, M. H. On the water masses and mean circulation of the south atlantic ocean. *Journal of Geophysical Research*, v. 104, n. C9, p. 20863–20883, 1999.

STRAMMA, L.; FISCHER, J.; REPPIN, J. The north brazil undercurrent. *Deep-Sea Research Part I*, v. 42, n. 5, p. 773—-795, 1995.

STRAMMA, L.; SCHOTT, F. The mean flow field of the tropical atlantic ocean. *Deep Sea Research Part II*, v. 46, p. 279–303, 1999.

TAYLOR, K. E. Summarizing multiple aspects of model performance in a single diagram. *Journal of Geophysical Research*, v. 106, n. D7, p. 7183–7192, 2001.

TRAVASSOS, P. et al. Thermohaline structure around seamounts and islands off north-eastern brazil. *Archive of Fishery and Marine Research*, v. 47, n. 2, p. 211–222, 1999.

TSUCHYIA, M. Subsurface countercurrents in the eastern equatorial pacific ocean. *Journal of Marine Research*, v. 33, p. 145–175, 1975.

UNESCO. *Brazilian Atlantic Islands: Fernando de Noronha and Atol das Rocas Reserves*. 2018. Accessed: April 2021. Disponível em: <http://whc.unesco.org/en/list/1000>.

VELEDA, D. et al. Seasonal and interannual variability of the southern south equatorial current bifurcation and meridional transport along the eastern brazilian edge. *Tropical Oceanography*, v. 39, n. 1, p. 27–59, 2011.

VELEDA, D. et al. Intraseasonal variability of the north brazil undercurrentforced by remote winds. *Journal of Geophysical Research*, v. 117, n. C11024, 2012.

VIIKMAE, B.; TORSVIK, T. Quantification and characterization of mesoscale eddies with different automatic identification algorithms. *Journal of Coastal Research*, v. 65, p. 2077–2082, 2013.

WEISBERG, R. H.; WEINGARTNER, T. J. Instability waves in the equatorial atlantic ocean. *Journal of Physical Oceanography*, v. 18, n. 11, p. 1641—1657, 1988.

WEISS, J. The dynamics of enstrophy transfer in two- dimensional hydrodynamics. *Physica D*, v. 48, n. 2-3, p. 273–294, 1991.

WELCH, P. The use of fast fourier transform for the estimation of power spectra: A method based on time averaging over short, modified periodograms. *IEEE Transactions on Audio and Electroacoustics*, v. 15, n. 2, p. 70–73, 1967.

WILSON, D. W.; JOHNS, E.; MOLINARI, L. Upper layer circulation in the western tropical north atlantic ocean during august 1989. *Journal of Geophysical Research*, v. 99, n. C11, p. 513—523, 1994.

WILSON, W. D.; JOHNS, W. E.; GARZOLI, S. L. Velocity structure of north brazil current rings. *Geophysical Research Letters*, Wiley Online Library, v. 29, n. 8, p. 114–1, 2002.

YI, J. et al. Enhancing the accuracy of automatic eddy detection and the capability of recognizing the multi-core structures from maps of sea level anomaly. *Ocean Science*, v. 10, p. 39–48, 2014.

ZHANG, Z.; WANG, Y.; QIU, B. Oceanic mass transport by mesoscale eddies. *Science*, v. 345, n. 6194, p. 322–324, 2014.